

CHARACTERIZATION OF MICROSTRUCTURE AND
MECHANICAL BEHAVIOUR OF HEAT AFFECTED
ZONES IN ROBOTIC ARC WELDING OF AA6061-T6

by

Zeli ARHUMAH

THESIS PRESENTED TO ÉCOLE DE TECHNOLOGIE SUPÉRIEURE
IN PARTIAL FULFILLMENT FOR A MASTER'S DEGREE
WITH THESIS IN MECHANICAL ENGINEERING
M.A.Sc.

MONTREAL, APRIL 24, 2019

ÉCOLE DE TECHNOLOGIE SUPÉRIEURE
UNIVERSITÉ DU QUÉBEC



Zeli ARHUMAH, All rights reserved



This Creative Commons licence allows readers to download this work and share it with others as long as the author is credited. The content of this work cannot be modified in any way or used commercially.

BOARD OF EXAMINERS

THIS THESIS HAS BEEN EVALUATED
BY THE FOLLOWING BOARD OF EXAMINERS

Prof. Tan Pham, Thesis Supervisor
Département de génie mécanique, École de technologie supérieure

Prof. Van-Ngan Le, President of the Board of Examiners
Département de génie mécanique, École de technologie supérieure

Dr. Fatemeh Mirakhorli, Member of the jury
National research council of Canada, Saguenay, QC, Canada

THIS THESIS WAS DEFENDED
IN THE PRESENCE OF A BOARD OF EXAMINERS AND THE PUBLIC
MARCH 29, 2019
AT ÉCOLE DE TECHNOLOGIE SUPÉRIEURE

ACKNOWLEDGMENT

I would like to express my sincere appreciation to my supervisor Prof. Tan Pham for his patience, motivation, and extensive knowledge.

I would also like to acknowledge the Libyan Ministry of Education for providing me the opportunity to pursue my master's studies and for recommending me for the scholarship offered.

I would like to thank Professor Van-Ngan Le and Dr. Fatemeh Mirakhorli for spending time and valuable comments as jury members.

Finally, I would like to thank my family and my friends for supporting me spiritually throughout my studies.

Caractérisation de la microstructure et propriétés mécaniques de la zone affectée thermiquement dans le soudage robotisé à l'arc de AA6061-T6

Zeli ARHUMAH

RÉSUMÉ

Le soudage GMAW de l'aluminium AA6061-T6 introduit un changement dans les propriétés mécaniques de la zone affectée thermiquement (ZAT) en modifiant la microstructure obtenue par vieillissement. La variation du cycle thermique de soudage à travers la ZAT produit différentes propriétés mécaniques des sous-zones dans la ZAT. L'objectif de cette étude est de caractériser la variation des propriétés mécaniques dans les sous-zones de la ZAT et de les corrélérer avec les cycles thermiques de soudage. Dans cette étude, les cycles thermiques de soudage, les propriétés microstructurales et mécaniques des plaques d'aluminium soudées AA6061-T6 ont été étudiées dans deux différentes configurations. Le robot Yaskawa intégrée avec l'équipement de soudage à l'arc Fronius Trans Plus Synergic 4000 et le métal d'apport A4043 ont été utilisés pour le soudage GMAW. Les cycles thermiques de soudage ont été obtenus expérimentalement à partir de différents emplacements de plaques soudées. À l'aide du logiciel SYSWELD, la source de chaleur est ajustée à partir des températures mesurées et de la taille de la zone fondue. Les simulations numériques ont été réalisées pour évaluer la répartition de la chaleur dans les plaques soudées. Le modèle numérique fournit une approximation acceptable comparée avec les températures mesurées. La caractérisation des propriétés mécaniques a été obtenue en utilisant un essai de microdureté sur la coupe transversale de la plaque soudée. La carte 2D est utilisée pour illustrer la microdureté. De plus, le comportement mécanique et la déformation locale dans les sous-zones de la ZAT ont été étudiés à l'aide d'un essai de traction micro-plat avec corrélation d'images numériques (DIC). Les propriétés mécaniques des sous-zones de la ZAT étaient corrélées au cycle thermique de soudage ainsi qu'à la microstructure de la ZAT étudiée expérimentalement. Il a été observé que le cycle thermique de soudage fait une variation importante de la microstructure à travers de la ZAT, qui influence à son tour de manière significative sur les propriétés de la ZAT. La transformation des précipités β'' vers β' et β est la cause de ces changements.

Mots-clés: Zone affectée thermiquement (ZAT), Cycle thermique, Microdureté, Microtension, Corrélation d'images numériques (DIC), SYSWELD, Propriétés mécaniques

Characterization of microstructure and mechanical behaviour of heat affected zone in robotic arc welding of AA6061-T6

Zeli ARHUMAH

ABSTRACT

GMAW welding of aluminum AA6061-T6 introduce changes in the mechanical properties of the heat affected zone (HAZ) by changing the microstructure obtained from heat treatment. The variation of the welding thermal cycle across the HAZ produces different mechanical properties in subzones of the HAZ. The purpose of this investigation is to investigate the variation of the microstructure and mechanical behaviour in the HAZ subzones and correlate these subzones with the welding thermal cycle. In this study, the welding thermal cycle, and the microstructural and mechanical properties of welded aluminum AA6061-T6 plates were studied. The plates were prepared and welded in two different configurations using a Yaskawa robot integrated with Fronius Trans Plus Synergic 4000 arc welding equipment and metal filler AA4043. The welding thermal cycle was obtained experimentally from different locations on the welded plates. Using SYSWELD software the heat source was adjusted using the thermal cycle obtained from the experimental work and the size of the welding pool to reproduce the welding thermal cycle. Simulation was performed to observe the heat distribution in two configurations of the welded plate. The numerical model offers an adequate approximation to the welding thermal profile measured during the welding process. The characterization of mechanical properties was obtained using a microhardness test on welding cross section and a 2D map used to illustrate the microhardness at the welding cross section. Moreover, mechanical behavior and local deformation in subzones of the heat affected zone were investigated using digital image correlation (DIC) with a micro-flat tensile test. The mechanical properties of subzones of the HAZ were correlated with the welding thermal cycle as well as with the microstructure of the HAZ that was investigated experimentally. It was observed that the welding thermal cycle controls the variation of the microstructure across the HAZ, which significantly effects the mechanical behaviour of the HAZ. The change of precipitates sequence from β'' to β' and β explains these changes.

Keywords: Heat affected zone (HAZ), Thermal cycle, Microhardness, Micro-tensile, Digital image correlation (DIC), SYSWELD, Mechanical properties.

TABLE OF CONTENTS

	Page
INTRODUCTION	1
CHAPTER 1 LITERATURE REVIEW	3
1.1 Aluminum alloys.....	3
1.2 Properties of aluminum.....	4
1.3 Aluminium magnesium silicon alloys (6XXX series).....	4
1.4 Strength in 6XXX	5
1.4.1 Alloying elements in 6XXX	5
1.4.2 Precipitation sequence in 6xxx	6
1.4.3 Hardening Mechanisms in Heat-Treatable Alloys.....	9
1.4.4 Precipitation Hardening (Heat Treatment) of Aluminum Alloy 6061-T6.....	10
1.4.4.1 Solution Heat Treatment	11
1.4.4.2 Precipitation Heat Treatment	12
1.5 Gas Metal Arc Welding (GMAW)	13
1.5.1 Welding Thermal Cycle.....	15
1.5.1.1 Thermal Cycle Measurement.....	16
1.6 Heat Affected Zone.....	17
1.6.1 Microstructure of the heat affected zone	19
1.6.1 Mechanical Properties of HAZ	22
1.6.1.1 Correlation between welding thermal history and hardness across HAZ	23
1.6.1.2 Mechanical properties characterization of HAZ.....	24
1.7 Summary.....	27
CHAPTER 2 EXPERIMENTAL PROCEDURE	29
2.1 Welding Equipment and Material Used.....	31
2.2 Sample preparation before welding	33
2.3 Welding parameters and configuration.....	33
2.4 Welding thermal cycle measurement.....	35
2.5 Procedures for characterisation of HAZ	36
2.5.1 Microstructure characterisation	36
2.5.2 Mechanical Characterisation.....	37
2.5.2.1 Microhardness Tests	37
2.5.2.2 Micro flat tensile test with DIC transverse to welding direction	38
2.5.2.3 Micro flat tensile test for samples extracted parallel to welding direction	41
CHAPTER 3 THERMAL ANALYSIS OF TWO GMAW CONFIGURATIONS	43
3.1 Welding thermal profile.....	43
3.1.1 Vertical configuration thermal profile	44

3.2	Sysweld models	46
3.2.1	Heat source used in SYSWELD	47
3.2.2	Mesh and boundary condition.....	49
3.2.3	Calibrating the heat source of the vertical plate.....	50
3.2.3.1	Thermal profile	51
3.2.3.2	Comparison between experimental and FE thermal profile	53
3.2.4	Adjusting heat source of the horizontal plate	54
3.2.4.1	Thermal profile	54
3.2.4.2	Comparison between experimental and FE thermal profile	57
CHAPTER 4 CHARACTERIZATION OF MICROSTRUCTURE AND MECHANICAL PROPERTIES		59
4.1	Heat affected zone width	59
4.2	Microstructure characterization of HAZ.....	62
4.2.1	Grain growth in HAZ.....	64
4.3	Mechanical characterization of HAZ in vertically welded plate	66
4.3.1	Microhardness behaviour across the HAZ.....	67
4.3.2	MFT parallel to the welding line	69
4.3.3	Micro-flat tensile test (DIC).....	74
4.3.3.1	Local behaviour of welded specimen from MFT test with DIC	75
4.3.3.2	Local behaviour of HAZ.....	78
4.3.4	Local behaviour of HAZ subzones in welded plate obtained by DIC	80
4.3.5	Local Stress–Strain properties obtained using DIC test in welded sample.....	81
CONCLUSION		89
RECOMMENDATIONS		91
APPENDIX I WELDED SAMPLES EXPERIMENTAL THERMAL PROFILE CAPTURE WITH THERMOCOUPLES		93
APPENDIX II THERMAL DISTRIBUTION CALCULATED BY SYSWELD		97
APPENDIX III MICROHARDNESS PROFILE IN TWO CONFIGURATIONS.....		99
APPENDIX IV MICROFLAT TENSILE TEST (DIC).....		103
LIST OF REFERENCES		107

LIST OF TABLES

		Page
Table 1.1	Phase transformation during aging of Al-Si-Mg alloys.....	7
Table 2.1	Chemical composition of the base metals.....	32
Table 2.2	Mechanical properties of base metal 6061-T6 and filler wire	32
Table 2.3	Chemical composition of filler wire	33
Table 2.4	Welding parameters for two plate configurations.....	33
Table 2.5	Location of thermocouples for temperature measurement.	34
Table 3.1	Standard deviation of peak temperature in horizontally welded plate	43
Table 3.2	Standard deviation of peak temperature in vertical welded plate	45
Table 3.3	Gaussian 3D conical heat source parameters for vertical plate	50
Table 3.4	Heating and cooling rate of Exp and FE vertically welded plate	52
Table 3.5	Difference in% of peak temperatures in vertically welded plate	54
Table 3.6	Gaussian 3D conical heat source parameters for horizontal plate	55
Table 3.7	Heating and cooling rate of Exp and FE horizontal plate.....	56
Table 3.8	Difference in % of peak temperatures in horizontally welded configuration	58
Table 4.1	Shows microhardness and peak temperature with the MFT result for each specimen parallel to weld.....	70
Table 4.2	Shows microhardness and peak temperature with the MFT result of each specimen parallel to weld.....	71
Table 4.3	Properties of base metal and welded specimens	74

LIST OF FIGURES

		Page
Figure 1.1	GP Zone Al-Mg-Si (6xxx) [13]	7
Figure 1.2	Transmission electron micrograph showing a, c) β'' (needle-shaped) , and b, d) β' (rod-shaped) precipitates [17].	8
Figure 1.3	The interaction between the particle and dislocation (a) Orowan looping, (b) particle cutting [18].	9
Figure 1.4	Main role of the age hardening mechanism [19]	10
Figure 1.5	Two stages of precipitation hardening in (T6) heat treatment	11
Figure 1.6	Phase diagram for precipitation-hardenable Mg_2Si aluminum	12
Figure 1.7	Strength vs aging time	13
Figure 1.8	Schematic of gas metal arc welding process, a) process overall, b) fusion area [23].	14
Figure 1.9	a) Welded plate, b) different temperature at different points.	15
Figure 1.10	Precipitation transformation through multistage thermal processing of (Al-Mg-Si) alloy during welding and PWHT [17].	17
Figure 1.11	Cross-section of (a) direct electric arc welding; (b) indirect electric arc welding	18
Figure 1.12	Grain size Mechanical properties relation of A356 alloy [33]	20
Figure 1.13	Microstructure changes through a fusion joining method. a) cooling slope of welding thermal. b) different microstructures in different HAZ subzones [26].	21
Figure 1.14	Heat effected zone of 6082-T6 aluminium; a) hardness profile; b) precipitate β' during cooling; c) hardness profile after aging [37].	24
Figure 1.15	The illustration of the test setup of DIC to characterise the local material properties [38].	25
Figure 1.16	Global strain of the specimens estimated with extensometer, local deformation fields characterised using DIC [43]	26

Figure 2.1	Schematic representation of experimental procedure	30
Figure 2.2	(a) Welding robot, b) Fronius Trans Plus Synergic power supply	31
Figure 2.3	(a) Horizontal welding configuration; b) Vertical welding configuration	34
Figure 2.4	Location of installed thermocouples	35
Figure 2.5	Extracted specimen from the a) horizontal welded plate, b) vertical welded plate	36
Figure 2.6	Polished and etched sample for microstructure characterisation extracted from horizontally welded plate	37
Figure 2.7	Distribution of microhardness indentation	38
Figure 2.8	DIC of machined samples transverse to the weld direction, a) and b) machined specimen, c) and d) the extracted samples.	39
Figure 2.9	Speckle patterns for DIC	40
Figure 2.10	Set up of micro tensile test with DIC	41
Figure 2.11	HAZ extracted micro-tensile specimens parallel to welding line, dimensions in mm, a) and b) machined specimen, c) and d) the extracted DIC samples.	42
Figure 3.1	Experimental thermal profile recorded by four TCs on each side of welding line in horizontally welded plate	44
Figure 3.2	Experimental thermal profile of vertical plate	45
Figure 3.3	YSWELD simulation process	47
Figure 3.4	Conical Gaussian volumetric heat source model	48
Figure 3.5	Mesh for simulation (with 1mm size in the HAZ, and 3mm outside the HAZ)	49
Figure 3.6	Thermal distribution at the moment when the heat source was in the center of the part.	50
Figure 3.7	Simulated thermal profiles at the same locations as the 4 thermocouples	51
Figure 3.8	Fusion zone of vertical welded plate	52

Figure 3.9	Thermal profile of vertical plate, a) thermal profile comparison between experimental results and finite element simulation of points at different distances from the welding center line, b) peak temperature comparison.....	53
Figure 3.10	Thermal profile of 4 nodes in the horizontally welded configuration corresponded to the location of TCs.....	55
Figure 3.11	Thermal distribution in horizontal welded plate.....	56
Figure 3.12	Melting zone	57
Figure 3.13	Thermal profile of horizontal plate, a) thermal profile comparison between experimental and finite element simulation from points at different distances from the welding center line, b) peak temperature comparison.....	58
Figure 4.1	Comparison between HAZ of optical image (discolouration) of welding cross section and FE result.	60
Figure 4.2	HAZ width characterised by microhardness profile on sample cross section in horizontal plate.....	60
Figure 4.3	Size of HAZ in vertical welded sample	61
Figure 4.4	Base metal of 6061-T6, a) coarse second phase particles distributed randomly, b) grain size of base metal.	62
Figure 4.5	Light optical micrographs of microstructure of FZ and PMZ; a) grains in FZ, b) low melting phases segregated on the grain boundary, c) The interface between the HAZ and fusion zone showing fine microscopic hot cracks, d) high magnification of figure (c).....	63
Figure 4.6	The relationship between average of grain growth and peak temperature across the HAZ	65
Figure 4.7	Light optical micrographs of recrystallization and grain growth; a) zone adjacent to FZ, b) gradual change of grain size	66
Figure 4.8	Correlation between thermal cycle and microhardness values in HAZ.....	67
Figure 4.9	Correlation between grain size, microhardness, and peak temperature across the HAZ.....	68
Figure 4.10	Cutting arrangement for the machined sample	69

XVIII

Figure 4.11	Microhardness measurement locations in the MFT samples.....	70
Figure 4.12	Stress- strain for different specimen extracted from different HAZ, a) Test 1, b) Test 2	72
Figure 4.13	Tensile properties in different zones, a) Test 1, b) Test 2.....	73
Figure 4.14	Global response (stress-strain) curves for welded sample and parent metal.....	74
Figure 4.15	Illustration of distribution of local in-plane strain acquired using DIC equivalent to different strains (corresponding to 24.mm specimen gauge length) for two specimens	75
Figure 4.16	Average value of ϵ_{xx} and ϵ_{yy} in transverse weld direction for three stages of stress/strain condition. a) 126 MPa_0.5%, b) 202 MPa_2.4% and, c) 225 MPa_5.1% illustrating local in plane strain localisation zones.....	77
Figure 4.17	Illustration of distribution of local in-plane strain acquired using DIC equivalent to different strains (corresponding to 24.mm specimen gauge length) in the HAZ	78
Figure 4.18	Average value of ϵ_{xx} and ϵ_{yy} in transverse weld direction for three stages of stress/strain condition. a) 160MPa-0.9%, b) 210 MPa-4.1% and c) 225 MPa-5.1% showing local in plane strain concentration zones	79
Figure 4.19	(a) Local strain-time for different locations on the welded sample, b) shows the location of local strain investigated (BM & HAZ & FZ)	81
Figure 4.20	(a) Stress-local strain in different locations obtained by DIC for welded sample, (b) close-up of figure (a).	82
Figure 4.21	Average stress-strain behaviour (DIC measurements) for welded joint, fracture planes in HAZ (Z1 and Z2) compared with base metal thermal cycle distribution across gauge length of DIC test specimen.....	83
Figure 4.22	Thermal history of extracted samples for DIC test, a) fusion zone, b) HAZ.	84
Figure 4.23	Correlations between mechanical properties and peak temperature profile along FZ and HAZ	85
Figure 4.24	Correlations between mechanical properties and peak temperature profile along HAZ.....	86

LIST OF ABBREVIATIONS

BM	Base metal
BOP	Bead on plate
DIC	Digital image correlation
Exp	Experimental
FEM	Finite element method
FZ	Fusion zone
GMAW	Gas metal arc welding
HAZ	Heat affected zone
MFT	Micro flat tensile test
MAG	Metal inert gas
OM	Optical microscopy
PMZ	Partially melted zone
TS	Travel speed of welding torch
TEM	Transmission electron microscopy
WD	Welded direction
WFS	Wire feeding speed
WCL	Welding center line
Z	Zone

LIST OF SYMBOLS

G	Temperature gradient
HV	Vickers hardness
I	Arc amperage
k_0	Bessel function
k	Thermal conductivity
MPa	Mega Pascal
nm	Nanometer
Q	Heat input
R	Distance from heat source
T	Temperature
TC	Thermocouple
T_0	Initial temperature
T6	Heat treatment
t	Time
UTS	Ultimate tensile strength
V	Arc voltage
v	Velocity of heat source
W	Width of subzone
Wt %	Weight percentage
YS	Yield strength
α	Thermal diffusivity
β	Mg ₂ Si precipitate
ϵ_{xx}	Strain in X direction
ϵ_{yy}	Strain in Y direction
ΔH	Change in hardness
η	Efficiency

INTRODUCTION

Aluminum and aluminum alloys have been broadly used in many different applications such as the aviation and automotive industries, as well as used as an alternative to steel because of their mechanical properties, low-weight and good corrosion resistance properties [1]. These properties have encouraged the spread of aluminum alloys which has made it the second most used metal in manufacturing after steel. Alloying elements and heat treatment affect the strength and process-ability of aluminum alloys, these alloys such as 6xxx & 7xxx have had their strength enhanced by precipitation-hardening and this increases the scientific and manufacturing interest especially in the aluminum alloy 6xxx series due to its extrudability and mechanical properties.

The 6xxx series aluminum alloys which contain mainly (Al-Si-Mg-Cu) have many advantages: for instance, good strength to weight ratio, extrudability, weldability, and good corrosion properties. It obtains its strength from a precipitate of Magnesium silicide (Mg_2Si) phase during heat treatment. Since the heat plays the main role in producing the alloy's properties, welding heat input causes major changes in the metallurgy of the heat affected zone [2]. Observations on the microstructure and mechanical behaviour of the welded specimen showed that to obtain optimum mechanical properties it is crucial to obtain homogeneously distribution of Mg_2Si precipitates and to control their size. Heating and cooling rate are the main variables to be controlled; for maintaining the fine grain structure and homogeneous distribution of Mg_2Si precipitates, hence the welding as joining process of aluminum alloys gains great importance.

Welding is a conventional manufacturing method for aluminum that has been widely used for many different applications. Gas metal arc welding (GMAW) is a joining technique utilised to manufacture aluminum parts and is a complicated method that involves different phenomena such as thermal, mechanical and metallurgical-chemical changes. A comparison between welding methods shows that; GMAW has several benefits such as producing high quality welds, flexibility, low cost, and the potential for full automation that results in high manufacturing efficiency.

Developments in welding processes have made aluminum alloys a target candidate for welding in manufacturing. Advanced automatic welding robots have minimised the heat input, and the thermal history variation along the welding line as a consequence of instability of welding speed.

Heat treatable aluminum alloys suffer significant loss of their mechanical strength caused by the welding thermal cycle. It introduces changes in the microstructure that lead to changes in the final mechanical properties of the area that is adjacent to the welding line (HAZ). These changes significantly depend on the thermal cycle and the base material properties. The variation of the welding thermal cycle introduces a different extent of metallurgical changes that lead to variations in the mechanical properties across the HAZ; these changes may be characterised in subzones based on the temperature attained in each zone.

An investigation is desirable to study the mechanical behaviour and microstructure of the HAZ and correlate it with the variation of the welding thermal profile. This study focuses on characterising the mechanical properties of welded aluminum alloy AA6061-T6 by robotic GMAW welding. The present investigation includes five chapters. The first chapter presents the theory and the literature review about the properties of aluminum alloy 6XXX series, GMAW robotic welding process, welding thermal cycle, and heat affected zone as a key point about the subject. The second chapter is reserved for the experimental procedure used in this study and its outcomes. The third chapter presents the numerical simulation of heat distribution and calculation of material properties for two welding configurations using Sysweld software. The fourth and fifth chapters contain the results and discussion in which welding thermal profiles obtained from two different configurations are presented visually by graphs and compared with the simulation result obtained from the Sysweld software. Moreover, the influence of welding thermal history on microstructure and mechanical behaviour was examined using microhardness and micro-tensile test with DIC to observe the local mechanical response in different zones within the HAZ. Finally, a correlation between welding thermal history, microstructure and mechanical properties in the HAZ was established. All the results observed were deliberated using the physical metallurgy in terms of the characterisation the mechanical properties of the HAZ.

CHAPTER 1

LITERATURE REVIEW

Investigation of the welding thermal cycle and characterization of the mechanical properties and microstructure for welded aluminum are an important consideration. Much research has been established to characterise the mechanical behaviour of the HAZ. Different methods have been used to correlate between the welding thermal cycle, microstructure and mechanical properties. This chapter will examine a range of aluminum alloys and the properties of these alloys in summary. This will be followed by the strengthening in heat treatable aluminum alloys. Also, the GMAW process will be described as well as the problems associated with aluminum welding, with a particular focus on 6xxx series aluminum alloys. A summary of previous studies about the influence of thermal history on microstructure and mechanical behaviour of welded aluminum will be provided to explain the phenomena that underlie the microscopic transformation of aluminum alloy during the fusion welding process.

1.1 Aluminum alloys

Aluminum alloys can be divided to non heat-treatable alloys such as the 1xxx, 3xxx, 5xxx series and heat-treatable alloys such as the 2xxx, 6xxx, 7xxx series. The mechanical properties of heat-treatable alloys such as the 6xxx series (Al-Mg-Si) alloys can be improved by heat-treatment, while non-heat-treatable alloys can be work hardened to improve their strength [3, 4].

Cold working can be used to improve the properties of non heat treatable alloys. These alloys are 1xxx series which are pure aluminum, 3xxx series which are known for their high formability, 4xxx series which have good fluidity, and 5xxx series which have good corrosion resistance and moderate strength. In heat-treatable alloys, the structure of the alloy is stabilised by heat treatment and consequently its strength is increased. 2xxx alloys are used

in the aviation industry and for high temperature applications. Due to high strength of 6xxx series alloys are appropriate for extrusion with moderate properties, non-corrodibility and high weldability. 7xxx series alloys have high strength but their strength drops to unacceptable levels after fusion welding and they are susceptible to hot crack. Due to their strength, heat-treatable alloys are commonly used in many different applications [1]. The main interest of this study is the heat-treatable AA6061-T6 alloy, which gains its mechanical properties from a heat treatment that precipitates fine particles of Mg_2Si [5, 6].

1.2 Properties of aluminum

There are many properties that attract researchers to focus on aluminum alloys. These properties can be summarised as follows [7]:

- Low density compared to steel; aluminum has only one third the density of steel,
- High resistance to a wide range of liquids, atmospheric gases and weather,
- Used as decorative material owing to high reflectivity,
- Its strength can be equal to that of normal construction steel,
- The high elasticity of aluminum can be an advantage under shock loads,
- Under low temperatures aluminum alloys preserve their toughness,
- Aluminum has good malleability and can be rolled to very thin foils,
- High conductivity to heat and electricity; approximately 50 % to 60 %, and 63% respectively of copper [8].

1.3 Aluminium magnesium silicon alloys (6XXX series)

The high strength aluminum alloys are used in many different applications. 2xxx and 7xxx aluminum alloys are used widely in the aviation industry and the automotive industry. 6xxx series aluminum alloys are of particular interest to the aviation industry (such as fuselage casings) and automobile manufacturing (for frames, bumpers and panels) because of its desirable combination of properties. There are many advantages of 6xxx aluminum alloys

including medium to high strength, extrudability, and good weldability. The weather resistance of 6xxx alloys is higher than 7xxx alloys, which are traditionally used in the aviation industry. 7xxx and 2xxx alloys are susceptible to intergranular attack. Moreover, 6xxx alloys are inexpensive and are particularly important to the aviation industry which relies on 2xxx and 7xxx alloys [9].

The component responsible for the high strength of 6xxx alloys is magnesium silicide Mg_2Si . Depending on the alloy designation, it may contain a small amount of manganese, zinc, copper and chromium. 6xxx series alloys are used widely in the welding fabrication industry, they are used mainly in extrusion, and are merged with various structural components [10]. 6xxx alloys are susceptible to weld cracking, therefore, it is recommended to weld them using filler material with arc welding. Hot cracking can be avoided using filler metals that contain high proportions of silicon such as AA4043 filler. In 6xxx heat-treatable alloys, the changes in microstructure and mechanical properties are complex and mainly depend on the welding conditions applied [3, 7].

1.4 Strength in 6XXX

Aluminum-silicon-magnesium alloy is one of the heat treatable alloys. Its strength after heat treatment can be increased threefold compared to its properties prior to heat treatment. There are two main factors that influence the strength in aluminum 6xxx: the alloying elements and the heat treatment stages or age hardening of the alloy.

1.4.1 Alloying elements in 6XXX

The principal elements responsible for strengthening the 6xxx series alloys are magnesium and silicon. 6xxx alloys acquire their strength during heat treatment, mainly from the precipitation hardening phase, Mg_2Si . The 6061-T6 alloy also includes traces of some other

elements such as manganese, chromium, copper and iron, which provide many favourable properties to the alloy.

The material properties depend upon the formation of metastable, completely coherent and stable semi-coherent and incoherent precipitates during aging as shown in Table 1.1. The table illustrates three important transformations that affect the strengthening of the alloy [10]. There are several previous studies that link the reliance of engineering strength on microstructure, specifically the characteristics, dimensions and forms of precipitates.

1.4.2 Precipitation sequence in 6xxx

Precipitation hardening is the arrangement of tremendously small dispersed particles of a second phase in the main phase matrix, which is achieved by heat treatment. The chemical composition of Al6061-T6 shows that the alloy is formed with a definite Mg:Si ratio (1.73:1) to form the quasi-binary Al-Mg₂Si system, and it increases its strength by precipitation of metastable β'' before the equilibrium β Mg₂Si phase. Therefore, understanding the phase transformation sequence during artificial aging is critical for a comprehensive understanding and to estimate the effect of the welding thermal history on the mechanical behavior of the alloy [11].

In general, the precipitation sequence of alloys containing Al-Mg-Si can be separated into the following phases: α (SSS) \rightarrow GP zones \rightarrow β'' \rightarrow β' \rightarrow β .

Table 1.1 Phase transformation during aging of Al-Si-Mg alloys

Phase	Coherency	Remarks
GP zone	Coherent	Spherical
β''	Coherent	Needle shape with round cross-section and completely coherent in aluminum matrix
β'	Semi-coherent	Rods with ellipsoidal cross-section and generally coherent but end of rods is incoherent to the matrix
β	Incoherent	Plates; totally incoherent to aluminum matrix

The overall precipitation sequence was summarised by Miao [12] with the crystal structures, morphology and metastable phases as shown in Table 1.1. During heat treatment, it first forms α (SSS), the super saturated solid solution which forms after quenching. The atoms then form Guinier-Preston (GP) zones (also called clusters) as presented in Figure 1.1.

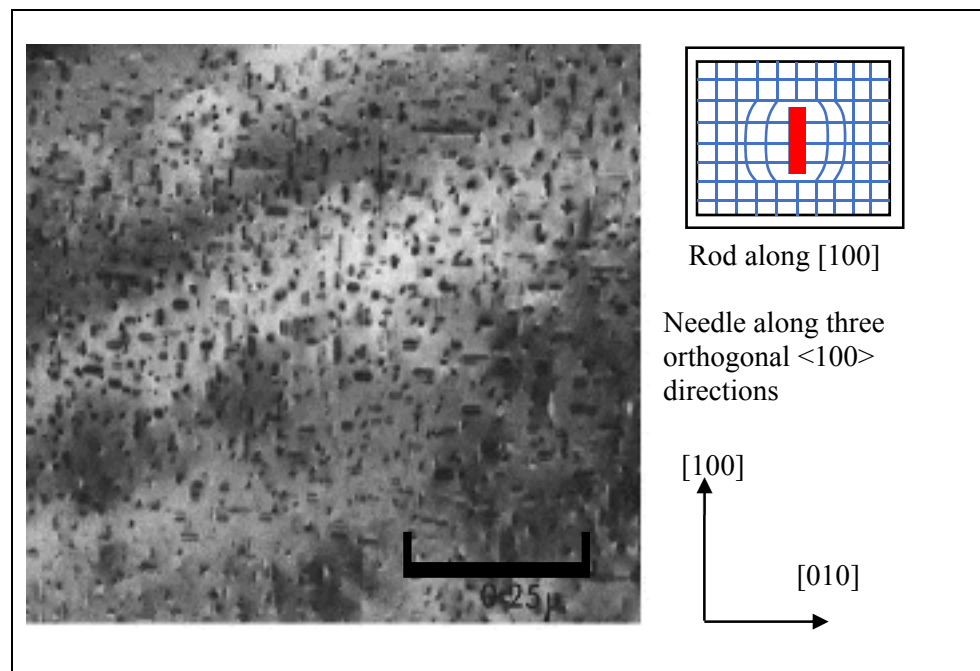


Figure 1.1 GP Zone Al-Mg-Si (6xxx) [13]

During artificial aging, the β'' phase starts to form as fine needle shaped precipitates which contribute to the peak strength of the alloy. Continuing the artificial aging results in a growing β'' and form β' phase which represents rod-like precipitates (circular cross section). The crystal structure in this phase is more defined and less cohesive with the matrix of the solvent. The growing of β' results in an equilibrium β phase (Mg_2Si) which is typically formed as plate [14] as shown in Figure 1.2.

There is a fine line that separates the three phase transformations and a short timespan between the precipitation hardening and the over-aging of the material. Exposing the material to a temperature for longer than required during artificial aging can result in the precipitates growing too large, dispersed, and becoming totally incoherent to the material matrix [15, 16]. This transformation causes the material to lose strength and become softer.

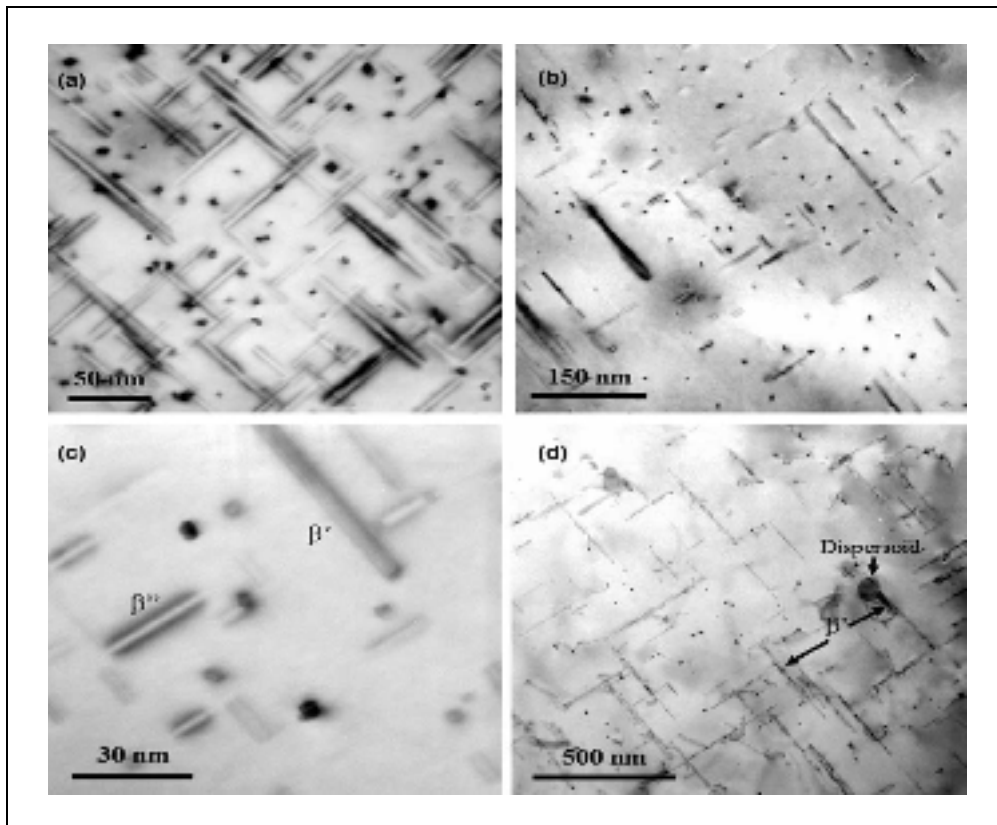


Figure 1.2 Transmission electron micrograph showing a, c) β'' (needle-shaped), and b, d) β' (rod-shaped) precipitates [17]

1.4.3 Hardening Mechanisms in Heat-Treatable Alloys

The properties of an age heat-treatable alloy are determined by the interplay of the distributed precipitate phase with dislocation. The interaction between the dislocations and the distributed particles will raise the critical resolved shear stress (RSS). Depending on how the dislocation penetrates the precipitated particles, two groups can be formed: Dislocation can loop around the particle or cut the precipitates [18].

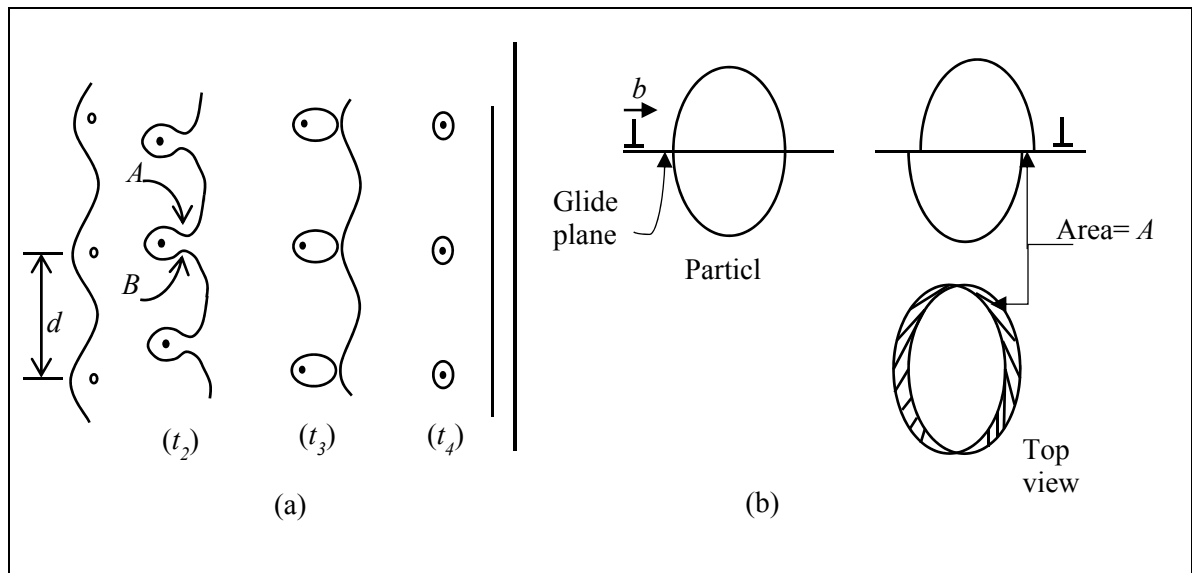


Figure 1.3 The interaction between the particle and dislocation (a) Orowan looping, (b) particle cutting [18]

In case of particle looping (known as Orowan looping), the dislocation loops out, and then divides from the looped area leaving one loop around the precipitate as shown in Figure 1.3.a. The loop is shaped around each particle when the dislocation passes the particle. This type of mechanism becomes beneficial when the particles have small diameters and the space between them is small. In contrast, particle cutting occurs if particles are small and coherent, when the dislocations glide right through the particle and are not stopped at the particle-dislocation contact as shown in Figure 1.3 b.

During the artificial aging procedure, the particle cutting mechanism works owing to small particles that precipitate first. As heat treatment continues, the precipitate size grows and looping around the particles becomes easier [19]. The role of hardening during the different stages of age hardening is shown in Figure 1.4.

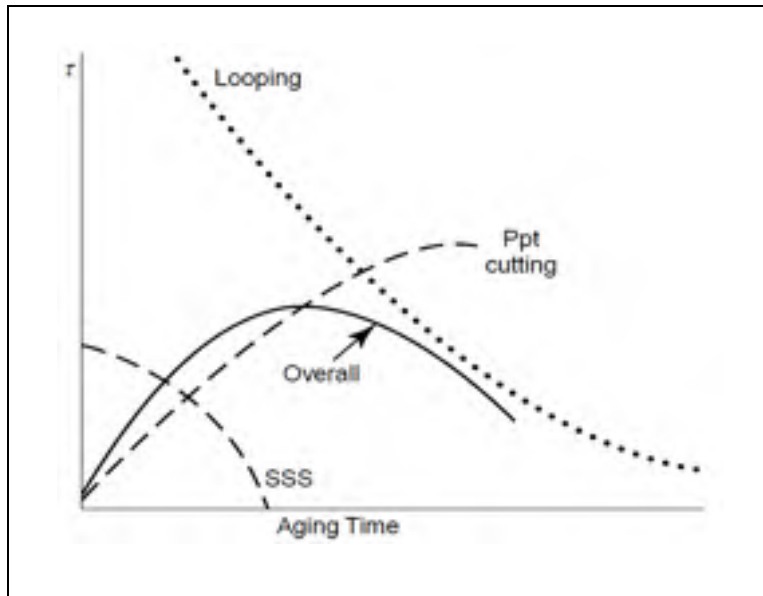


Figure 1.4 Main role of the age hardening mechanism [19]

1.4.4 Precipitation Hardening (Heat Treatment) of Aluminum Alloy 6061-T6

The term age hardening is used when the material's strength develops over time. Precipitation hardening of Al6061-T6 is accomplished by two stages; the first stage uses solution heat treatments and the second stage uses precipitation heat treatment, as shown in Figure 1.5 and Figure 1.6 [20].

1.4.4.1 Solution Heat Treatment

The first step of the precipitation hardening procedure is solution heat treatment. The aluminum silicon magnesium solution is heated to a specific temperature, T_0 , within the α phase and held until all the β phase (Mg_2Si) is totally dissolved. The supersaturated solid solution is then quenched to room temperature T_1 after quenching a supersaturated solid solution (SSS) of magnesium, silicon, and some other elements formed in aluminum matrix at room temperature.

After this process, the alloy is referred to as T4 temper. The alloy after quenching is said to be a supersaturated solid solution SSS with respect to solute β in solvent α , and the alloy is comparatively soft and weak [20].

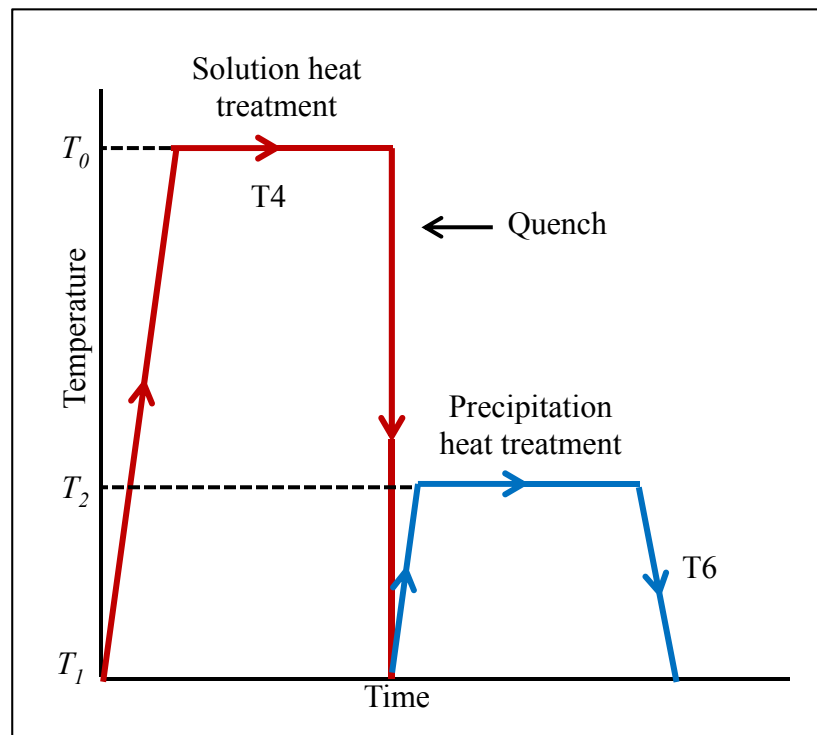


Figure 1.5 Two stages of precipitation hardening in (T6) heat treatment

1.4.4.2 Precipitation Heat Treatment

The second stage in the T6 precipitation hardening process is precipitation heat treatment. During this stage, the supersaturated α phase solution is heated to an intermediate temperature between 175°-195°C, for a specific period of time within the $\alpha + \beta$ phase region. Three different time-temperature cycles can be used for aging: one hour at 200°C, five hours at 175°C, or eight hours at 165°C. The three cycles can accomplish the same result T6 [19].

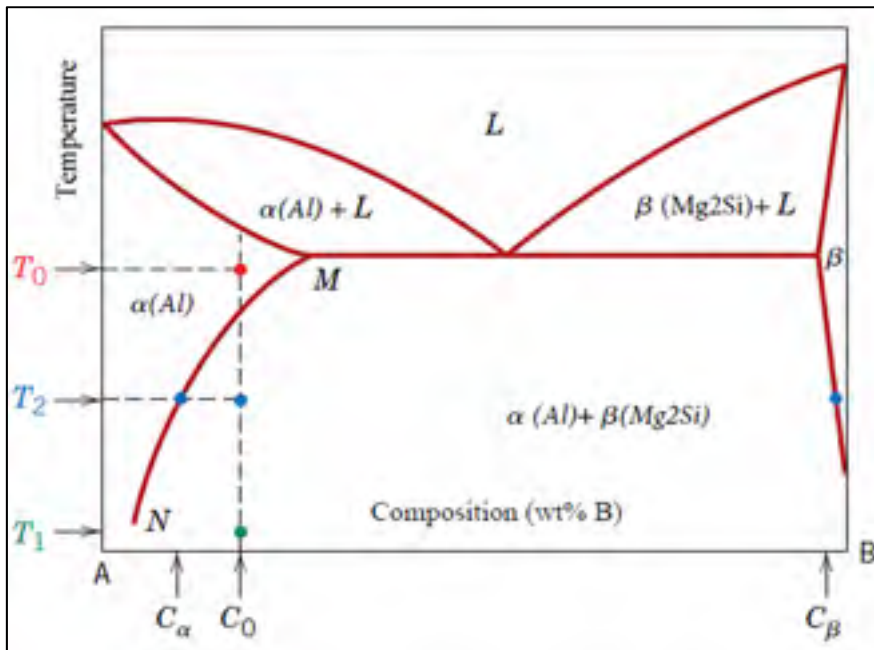


Figure 1.6 Phase diagram for precipitation-hardenable Mg₂Si aluminum

During the primary aging time, microscopic clusters, or GP zones, of Mg₂Si atoms form at countless positions in the α phase, as shown on the strength-aging diagram in Figure 1.7. As aging time increases, the constant diffusion of Mg₂Si causes the zones to increase their size to form particles.

The precipitated particles go through two phases, signified as β'' and β' , before the equilibrium phase β forms as finely dispersed particles of Mg_2Si . The β'' phase shows the peak strength of the aged alloy, which is conserved upon cooling to ambient temperature at the suitable aging time [20].

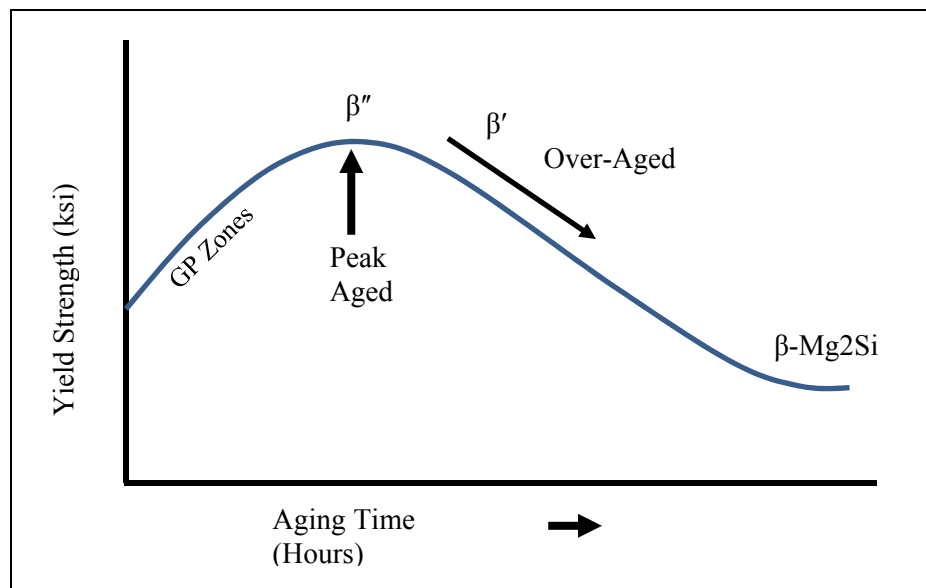


Figure 1.7 Strength vs aging time

1.5 Gas Metal Arc Welding (GMAW)

Gas metal arc welding (GMAW) is a conventional fusion joining method, which is commonly referred to as metal inert gas (MIG). There are other kinds of aluminum welding methods including: plasma arc welding (PAW), laser-beam welding (LBW), stud welding (SW), gas tungsten arc welding (GTAW), and friction stir welding (FSW).

GMAW and GTAW fusion joining are commonly used to weld aluminum alloys [21]. To facilitate the welding and avoid hot cracking, filler metal is used. Different alloys are compatible with different filler metals depending on the alloying elements in the welded alloys. In the 1940's, GMAW was invented for joining aluminum and other materials. Generally, GMAW is appropriate for thick materials [22].

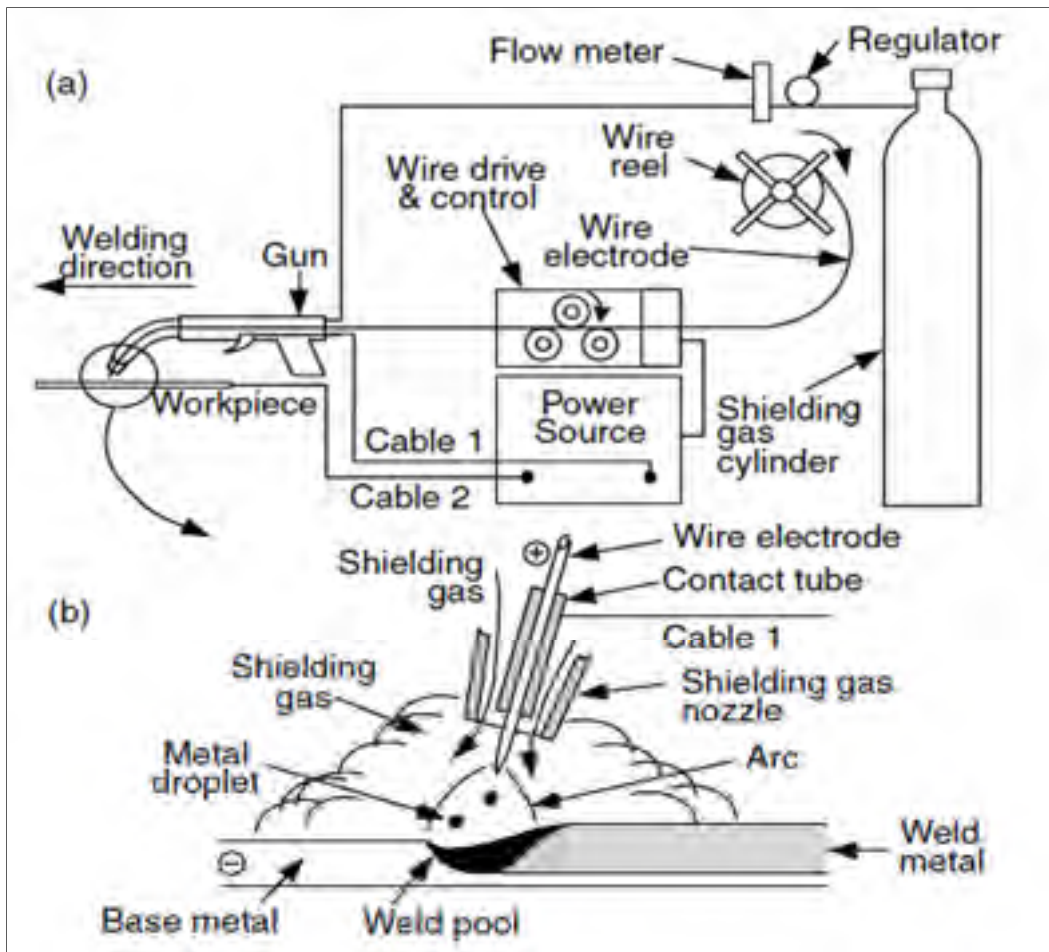


Figure 1.8 Schematic of gas metal arc welding process, a) process overall, b) fusion area [23]

The GMAW method uses inert gas to protect the welding bead. Robotic GMAW welding was used for this investigation owing to its wide range of applications. Moreover, steady welding velocity facilitates the capturing of the welding thermal cycle, since it is eliminating the variation in the thermal cycle along the welding line. Three key factors control the procedure for GMAW of aluminum: the availability of equipment, the welded material thicknesses, and the alloy content [23]. The schematic in Figure 1.8 shows the GMAW process.

1.5.1 Welding Thermal Cycle

Thermal cycle in welding is the variation of temperature over time. It affects the microstructure and the mechanical properties of the welded material. During fusion welding, interaction among the parent metal and the heat source causes a rapid heating and melting in a small volume of the metal during a short time. In the welding pool, the high temperature causes the loss of alloying elements by evaporation, and the absorption of gases such as hydrogen. The properties of the material in the HAZ and fusion zone depend upon the alloy composition and the past processing history of the base and filler material along with the thermal history experienced during welding. As a moving heat source (welding arc) approaches the closest distance to the location of interest, first temperature increases, then gradually decreases. Each point in the material has a different weld thermal cycle as a function of its location relative to the moving heat source as illustrated in Figure 1.9.

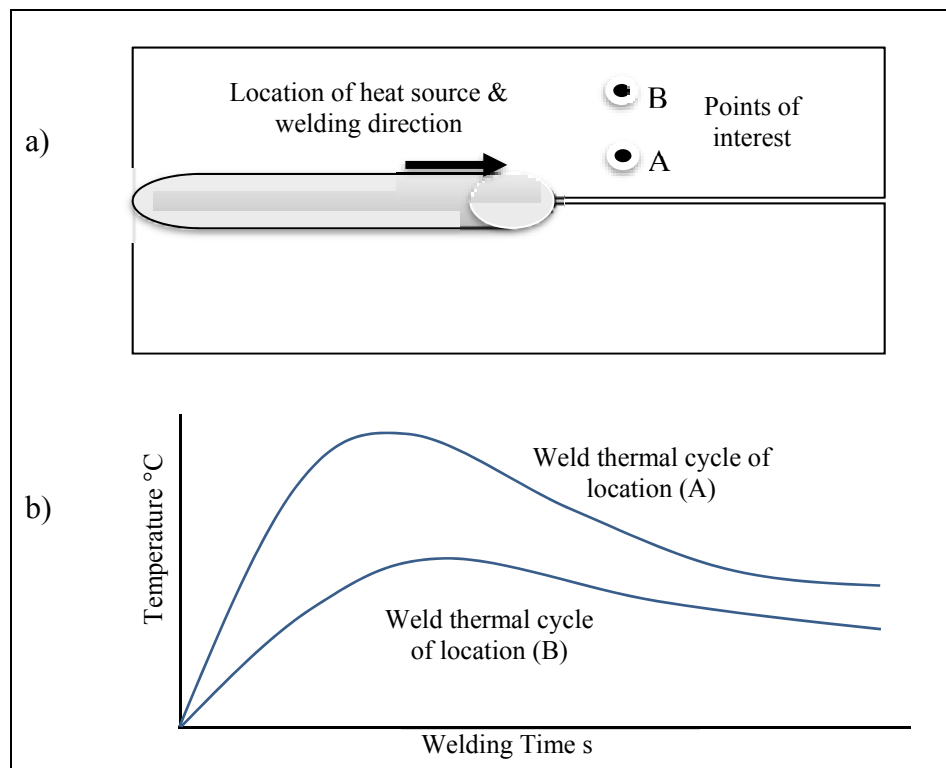


Figure 1.9 a) Welded plate, b) different temperature at different points

There are many analytical solutions used to calculate the thermal cycle and heat distribution. Rosenthal's solution is used for two and three-dimensional heat flow to calculate the thermal cycles in the workpiece during welding as shown in Equations (1.1) and (1.2).

$$\frac{2\pi(T-T_0)}{Q} = \exp\left(\frac{v_x}{2\alpha}\right) k_o\left(\frac{v_r}{2\alpha}\right) \quad (1.1)$$

$$\frac{2\pi(T-T_0)}{Q} = \exp\left[\frac{-V(R-x)}{2\alpha}\right] \quad (1.2)$$

1.5.1.1 Thermal Cycle Measurement

Welding temperature can be recorded using different techniques such as thermocouples, non-contact method infrared radiation (IR), or temperature indicating paints. Thermocouples are one of the most reliable methods for recording the thermal profile of welding, used with ceramic tubes to protect the thermocouples from welding spatter especially when the thermocouples are attached near the welding line. Many studies have been conducted to measure the thermal history of welded joints and cooling curves [16, 24].

Because the IR method is based on radiation and requires no physical contact with the workpiece, it is suitable to measure the temperature in the weld pool (fusion zone). In a study conducted by Guoli, the welding temperature profile of AZ31B alloy welded by GTAW was measured by IR, and thermocouples were used to measure the cooling curves. In his study the peening method was used to attach K-type thermocouples to the workpiece, and the thermocouples were connected to the INV306DF data acquisition throw amplifier. A data logger was adjusted to record 10 readings per second, and the result was found to be reliable [25].

Another investigation was carried out by Ambriz to measure the thermal profile during the welding of aluminum alloy using indirect electric arc welding method. In the study, K-type thermocouples were used. The result of the study was that the cooling slopes of the thermal profile correlated with the TTT diagram to explain the transformation that occurred and this predicted the material behavior in the HAZ [26]. V. Malin [27] used temperature indicating paints to capture the welding thermal cycle for AA6061 during GMAW-P. He reported that the maximum reliable temperature recorded was 371°C and he extrapolated until reach the solidus temperature.

1.6 Heat Affected Zone

The heat affected zone (HAZ) is the region between the melted zone (nugget) and the unaffected material of base metal. The HAZ is exposed to the most variation in temperature as it is rapidly being heated and cooled. This variation is a function of the distance from the fusion zone. The variation in the thermal cycle introduces variation in the microstructure and mechanical properties across the HAZ [28, 29].

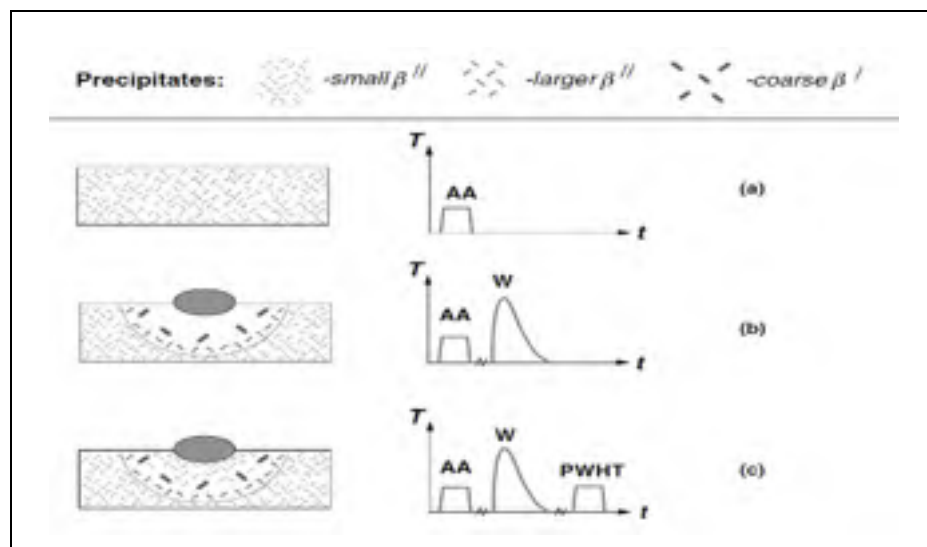


Figure 1.10 Precipitation transformation through multistage thermal processing of (Al-Mg-Si) alloy during welding and PWHT [17]

Because the temperature during the welding process is not high enough to melt the HAZ, it contains a mix of recrystallization and over aged materials [30]. Typically, increasing the heat input will result in growth of the HAZ size and will degrade the mechanical properties across the HAZ as shown in Figure 1.10. Quenching the welded material to increase its hardness will cause the HAZ to become distorted, as a result the metal must be introduced into its intended uses in as-welded condition. In a study conducted by Ambriz [31], he reported the effect of arc welding on AA6061-T6 microstructure and mechanical properties.

The previous study by Ambriz reported that the cause of hot cracking during GMAW was owing to the very high thermal expansion of the aluminum alloys, as well as their wide range of solidification temperatures. The weld was performed on AA6061-T6 alloy using the indirect electric arc (IEA) method, which involves a single weld pass with feeder strips positioned on top of the workpiece. This technique successfully decreased the heat input during the welding which decreased the HAZ size as illustrated in Figure 1.11. This method requires the base metal to be preheated before welding.

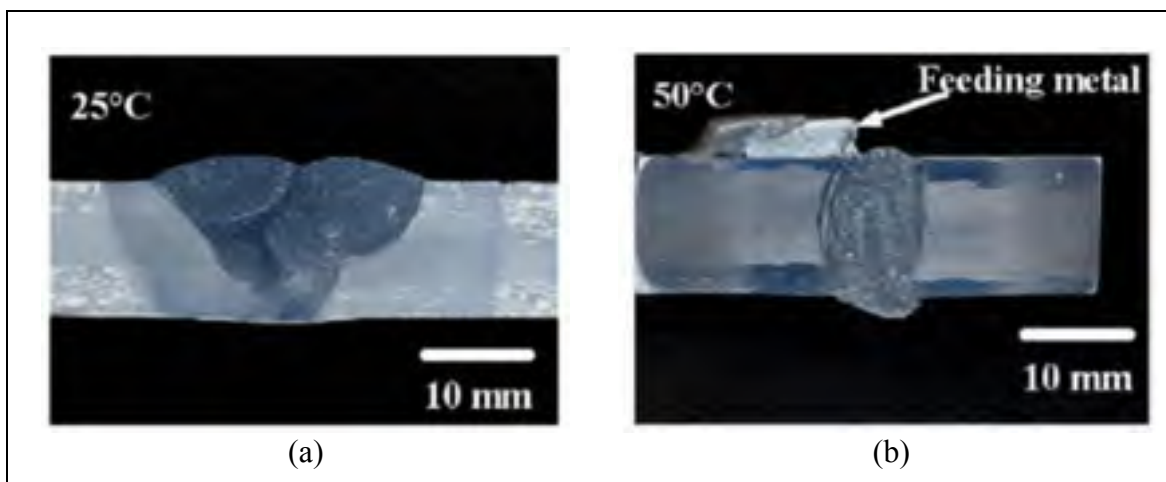


Figure 1.11 Cross-section of (a) direct electric arc welding; (b) indirect electric arc welding

Ambriz studied the effect of material preheating to 50°C, 100°C, and 150°C on the mechanical properties of the HAZ. He determined that the HAZ size was reduced for both

the 50°C and the 100°C preheating treatments, but with the 150°C preheating treatment it was larger than what would be obtained using single V direct electric arc welding. In Figure 1.11 above, the difference in the HAZ cross-sections of the two welds can be seen.

Hirose [32], performed a study of the heat affected zone in laser welding using AA 6061-T6. More heat input during the welding process caused a lower hardness value in the heat affected zone; consequently, a welding technique with low heat input is desired. In the Hirose study, laser welding with a CO₂ laser and TIG welding were performed on a 1-mm thick piece of AA6061-T6. Hirose reported that the heat affected zone for laser welding was roughly 1/7 to 1/4 of the size of that obtained using TIG welding. Moreover, for laser welding the hardness of the HAZ was almost fully recovered with artificial aging.

1.6.1 Microstructure of the heat affected zone

When the heat affected zone is exposed to the welding thermal cycle, it results in recrystallization, recovery, grain growth and precipitation reaction. The area close to the fusion zone forms large equiaxed grains. In non-heat treatable alloys, the recrystallization process causes the most of the loss of strength that occurs. However, in heat treatable alloys such as 6xxx, grain growth contributes only slightly to overall strength loss as in Figure 1.12. This problem can be mitigated by using grain pinning dispersoids. Figure 1.12 shows that there is no significant effect of grain growth on mechanical properties for heat treatable alloy A356 until the grain size exceeds an average size of 1mm.

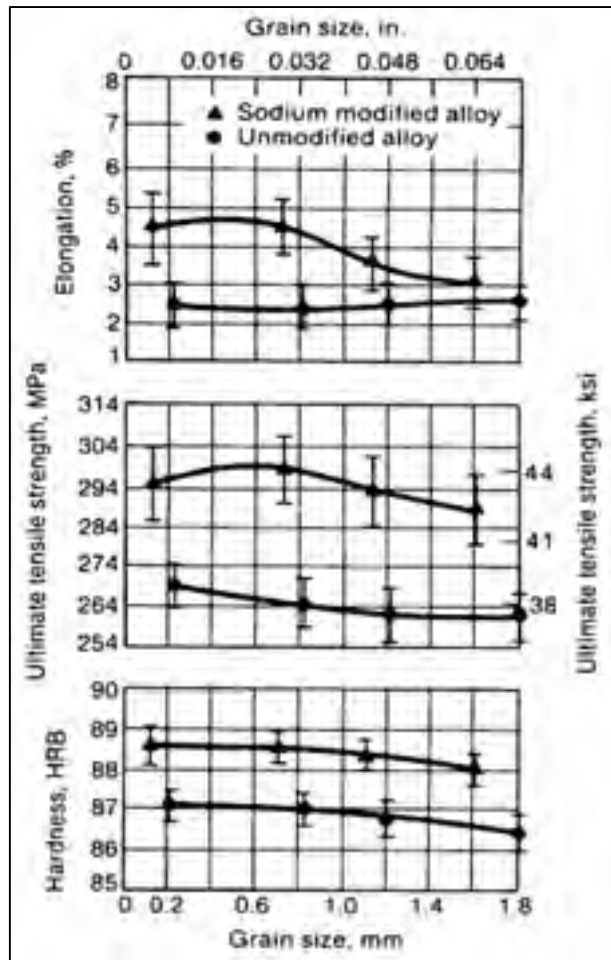


Figure 1.12 Grain size Mechanical properties relation of A356 alloy [33]

In heat-treated alloys such as Al-Mg-Si, the thermal cycle introduces severe strength loss. This strength loss is due to the transformation of β'' precipitates involving dissolution or coarsening to β' or β when exposed to the welding thermal cycle [34]. When the temperature surpasses the solvus temperature in the HAZ, the precipitates β'' completely dissolve and in cases where the temperature is lower than the dissolving temperature, the precipitate grows and forms β' or β .

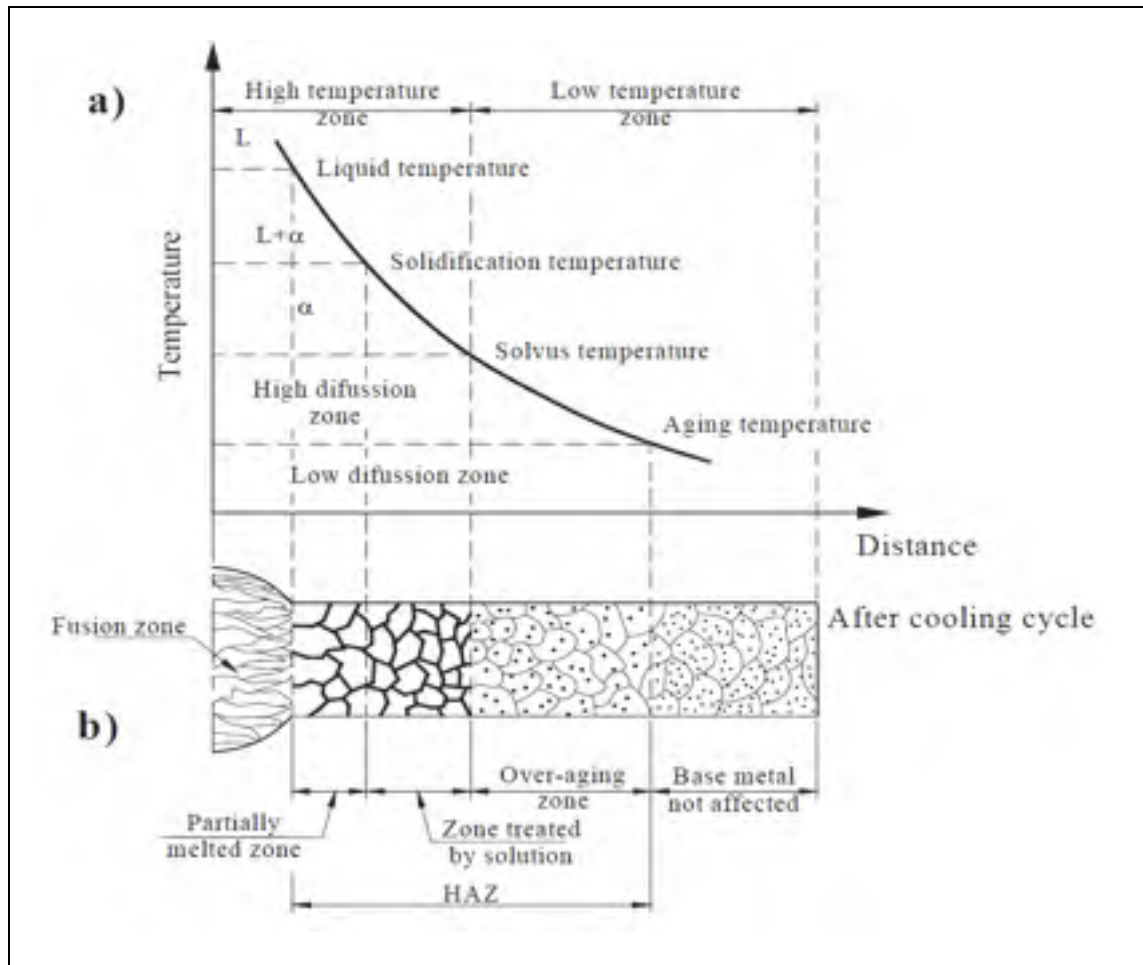


Figure 1.13 Microstructure changes through a fusion joining method. a) cooling slope of welding thermal. b) different microstructures in different HAZ subzones [26]

The formation of dissolution of the precipitate leads to decreased strength in the HAZ. In the heat affected zone that is located far from the FZ boundary, where the peak temperature does not surpass the solvus temperature, the precipitates suffer either partial dissolution or coarsening. Dissolution and coarsening will differ across the HAZ as a function of thermal cycle peak temperature.

1.6.1 Mechanical Properties of HAZ

The welding thermal cycle causes a degradation of the mechanical properties of the material that is adjacent to the fusion zone. Because the mechanical behaviour depends on the microstructure of the HAZ, many studies have been carried out to determine the effects that welding has on the mechanical properties of the welded materials. In AA6061-T6, the needle shape β'' precipitate is the main phase that contributes to hardening, and because β'' is very small (20 - 100 nanometers in length, and 6 nanometers in diameter), it can only be observed via transmission electron microscopy (TEM). However, the contribution to the hardening can be measured using microhardness and tensile strength tests[35].

In a study by V. Malin [27], tensile and hardness tests were performed on a workpiece of AA6061-T6 that had been welded using gas metal arc welding GMAW with a filler wire AA4043. A Knoop microhardness test with a 100-garm load was used to generate a microhardness profile. The hardness measurements were taken transverse to the weld line, and in increments of 0.9 mm and 1.8 mm from the weld line. The study reported that the microhardness profiles in the heat affected zone were around 70% of the base material hardness. Malin also used a helpful representation of hardness distribution across the HAZ to characterise the subzones of the HAZ. Moreover, the average hardness values in these subzones were correlated with the thermal gradient and width of the HAZ. Hardness average across subzones was expressed as:

$$G_{H ave} = \frac{\Delta H}{W} \quad (1.3)$$

where ΔH is the change in hardness values at the borders of the zone, and W is the width of the subzone [27]. During welding, the exposure to high temperature causes grain growth in the HAZ, making it softer and more susceptible to failure. However, in the previous study there was no attempt to measure the grain size in the HAZ and correlate it to thermal cycle

and mechanical properties. The study reported that the yield strength of the AA6061-T6 material before welding was 305MPa, which decreased to an average value of 206MPa after welding. Moreover, seven specimens out of the 12 tested in the study failed in the HAZ. The failure location ranged from 10.16 mm – 11.85 mm from the fusion line.

1.6.1.1 Correlation between welding thermal history and hardness across HAZ

The change in HAZ hardness is caused by the welding thermal cycle, therefore variation in the thermal cycle will cause variation in hardness across the heat affected zone [36]. The correlation between welding peak temperature and microhardness of a gas metal arc process on welded joints was studied by V.Malin. Microhardness and peak temperatures were measured across the welded joints, which were also subjected to tensile tests. The study reported that there is a relationship between the peak temperature and the average hardness value in the HAZ.

It was noted in the investigation by Myhr and Grong [37] as illustrated in Figure 1.14 a, b and c) that the thermal slopes have direct correlation with the mechanical properties of the HAZ. A lower thermal gradient correlates to lower tensile strength in the welded joint. It was also found that the minimum hardness in the HAZ occurred in the region subjected to a temperature between 240°C and 380°C. Two main factors were identified that affect the loss of strength and hardness in the HAZ. The first factor is the peak temperature of the critical zone (zone exposed to a peak temperature range of 240°C - 380°C) and the second factor is the time of its exposure to this critical temperature.

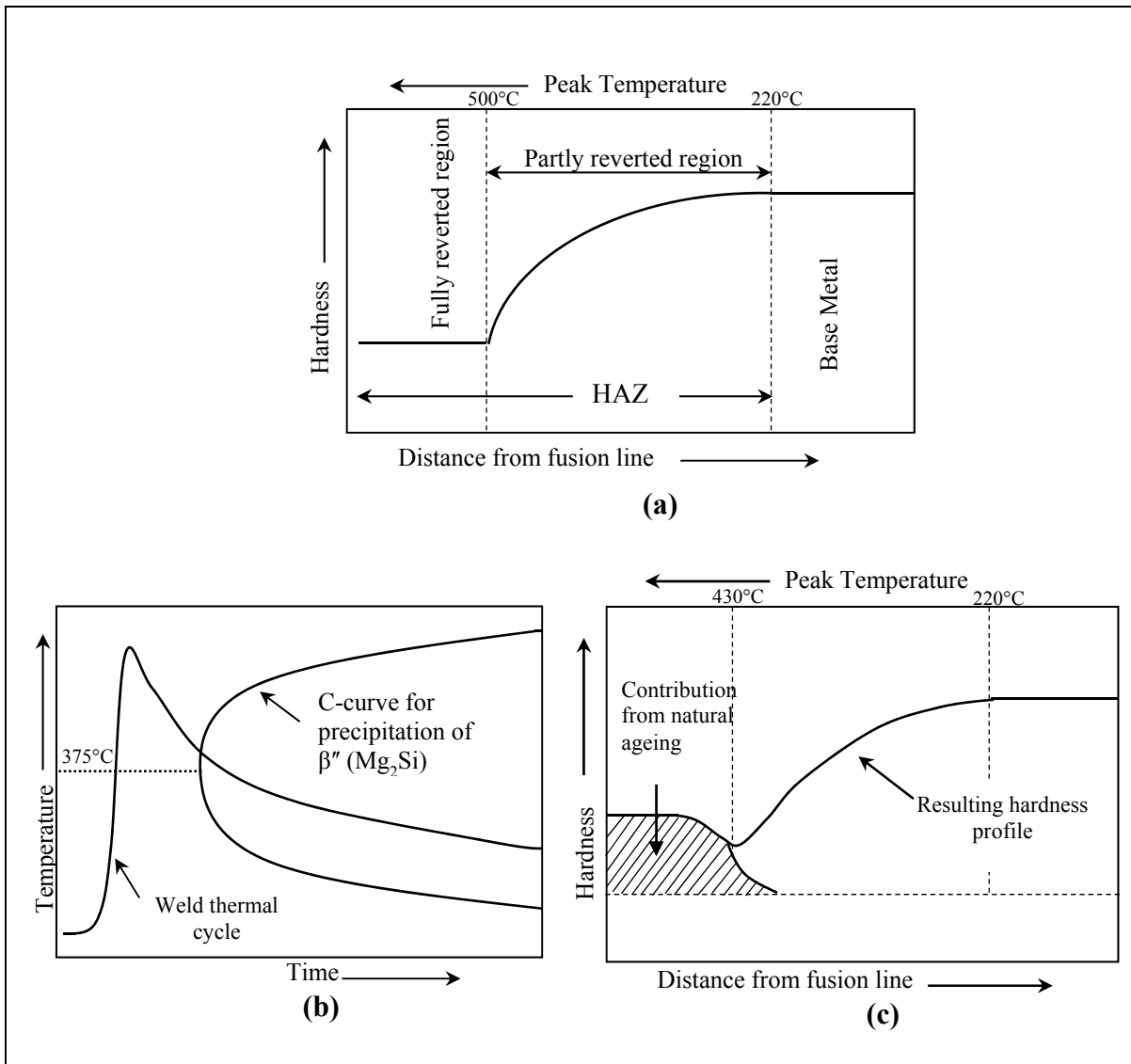


Figure 1.14 Heat effected zone of 6082-T6 aluminium; a) hardness profile; b) precipitate β' during cooling; c) hardness profile after aging [37]

1.6.1.2 Mechanical properties characterization of HAZ

The comprehensive properties of the welded material are subject to the distribution of mechanical behaviour across the HAZ. Therefore, it is important to characterise the local mechanical behaviour of subzones in HAZ. An extensometer can measure the average strain over a larger gauge length but not the local variation in strain. Digital image correlation

(DIC) can be used to characterise the local mechanical behaviour and obtain local stress strain curves in different zones within the HAZ [38].

DIC is a technique that applies correlation analysis to study digital images produced while a specimen is under traction test. This method involves capturing repeated images with a high resolution camera while simultaneously applying a load to evaluate the local deformation and characterise the local behavior of the material under incremental loads as shown in Figure 1.15 [39].

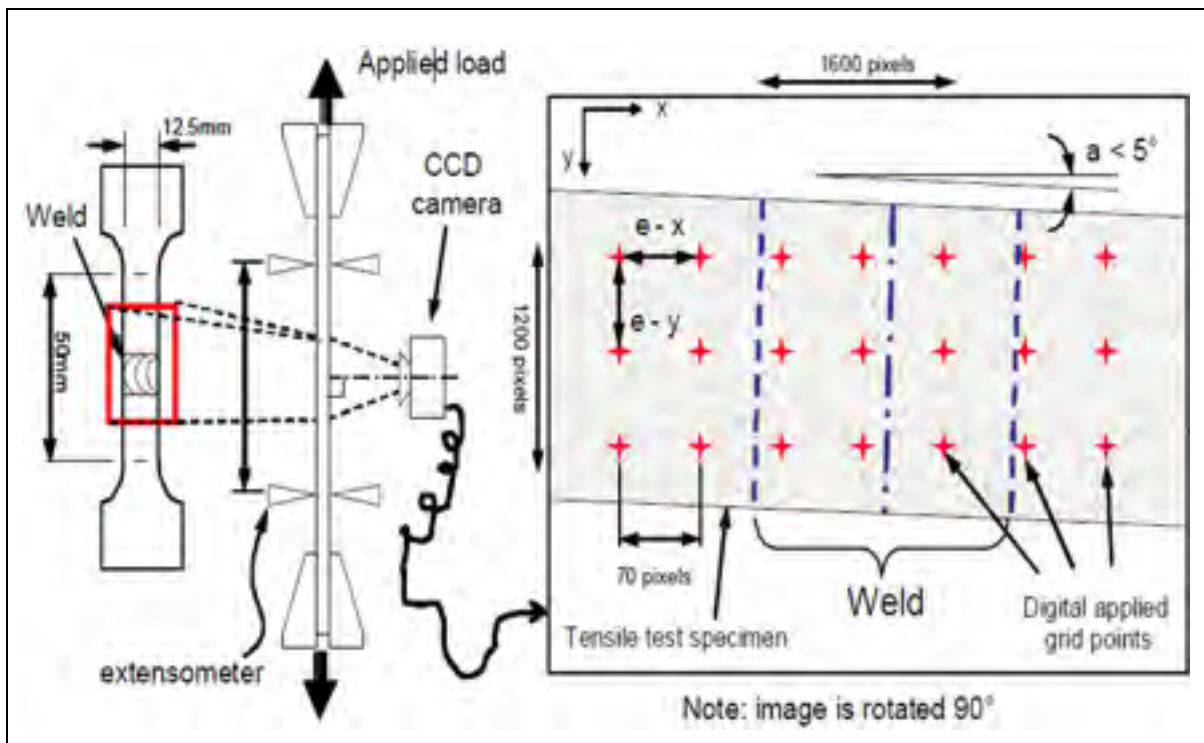


Figure 1.15 The illustration of the test setup of DIC to characterise the local material properties [38]

An investigation of the influence of thermal cycle on mechanical behaviour of subzones in the HAZ, must begin with a classification of non-homogenous subzones within the heat affected zone [40, 41]. Many investigations have been conducted in this field to characterise the mechanical properties of GMAW, laser welding and FSW using transverse tensile weld

sample loading and assuming iso-stress conditions. The stress strain results determined by mapping the local strain captured using DIC corresponds to global stress as shown in Figure 1.16 [42, 43].

Lockwood [44] examined the local behaviour of a friction stir welded joint of aluminum alloy AA2024 numerically and experimentally. Measurements of local field deformation were performed on tensile samples using the DIC method. The results obtained for different weld zones were used to establish a 2D finite element model. Evaluation of the model outcomes and the experimental outcomes were used to evaluate the viability and validity of the model.

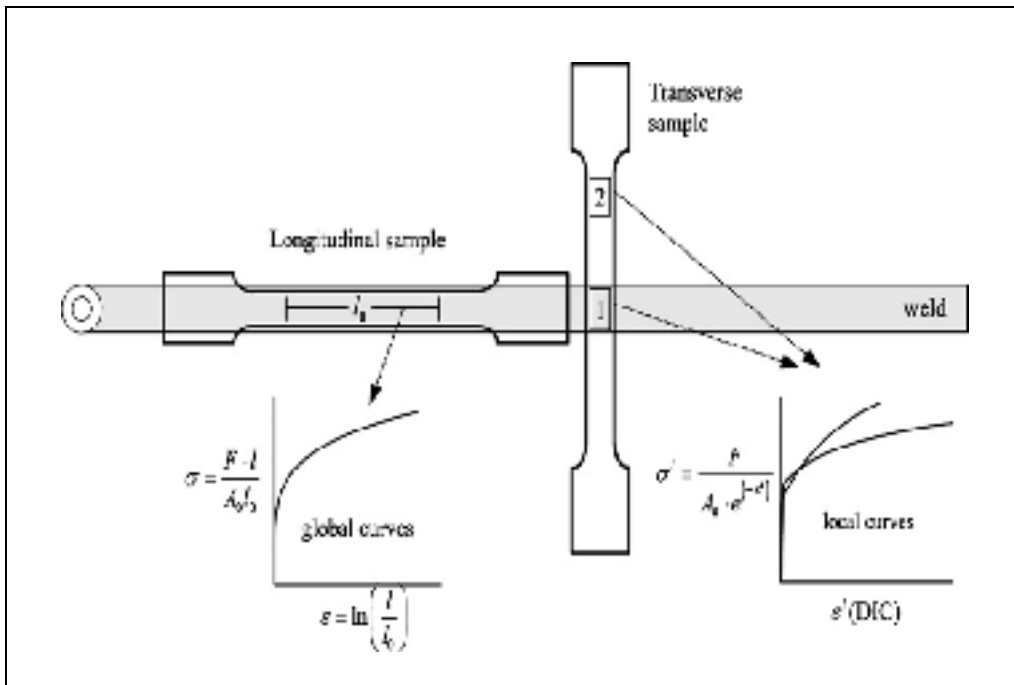


Figure 1.16 Global strain of the specimens estimated with extensometer, local deformation fields characterised using DIC [43]

A study by Reynolds [45] used a tensile test specimen extracted from the welded region and used the DIC method to determine the mechanical properties of FSW welded joint of aluminum AA5454-O and AA5454-H32. The study characterised the mechanical behaviour

of the material by carrying out a tensile strength test transverse to the weld. The stress strain behaviour of the welded sample was analysed by assuming that the deformation occurs under iso-stress conditions and the weld was a composite material.

Lakshminarayanan [46], studied the influence of single pass welding performed by GMAW, GTAW, and FSW on the mechanical behaviour of welded samples 6.4mm in thickness. The base metal of the butt joint was AA6061-T6 aluminum alloy, and AA4043 was used as filler material. The three joints were compared using microhardness, microstructure, and tensile tests, and fracture surface morphology. The investigation showed that FSW joints have fine microstructure in the weld zone and are superior in terms of mechanical properties to GMAW and GTAW.

1.7 Summary

This literature review was conducted to analyse the influence of welding thermal history on the mechanical behaviour and microstructure of the material. First, the physical metallurgy of aluminum, and aluminum joining processes were investigated in short. Then different investigations were reviewed examining welding thermal cycle, and problems caused by welding including change in microstructure, hardness and mechanical properties response. Finally, analyses of the characterisation of mechanical behaviour of the heat affected zone consisting of experimental investigations were reviewed. This investigation is required to examine the thermal history, microstructural, and mechanical correlations during welding procedures to characterise the mechanical behaviour of the HAZ.

CHAPTER 2

EXPERIMENTAL PROCEDURE

The objective of this experimental investigation was to characterise the microstructure and mechanical properties of the HAZ and correlate them with the welding thermal cycle of 6061-T6, as shown in the flowchart in Figure 2.1.

A robotic welding system was used to perform a gas metal arc welding (GMAW) weld on 6061-T6 plates. Thermocouples integrated with data acquisition were used to capture the welding thermal cycle. SYSWELD software was used to simulate the GMAW of AA 6061-T6 to evaluate the temperature distribution in the HAZ. The thermal profile obtained by experimentation was used to calibrate the heat source. The microstructure transformation of the HAZ was calculated.

Transverse cross-section specimens extracted from the welded samples were used to characterise the microstructure of the HAZ and to generate a microhardness profile for the HAZ and base metal. To characterise the variation of mechanical properties across the HAZ, local stress–strain curves across the HAZ were obtained by transversely loaded DIC sample. More details about each process and characterisation are explained in the following sub sections.

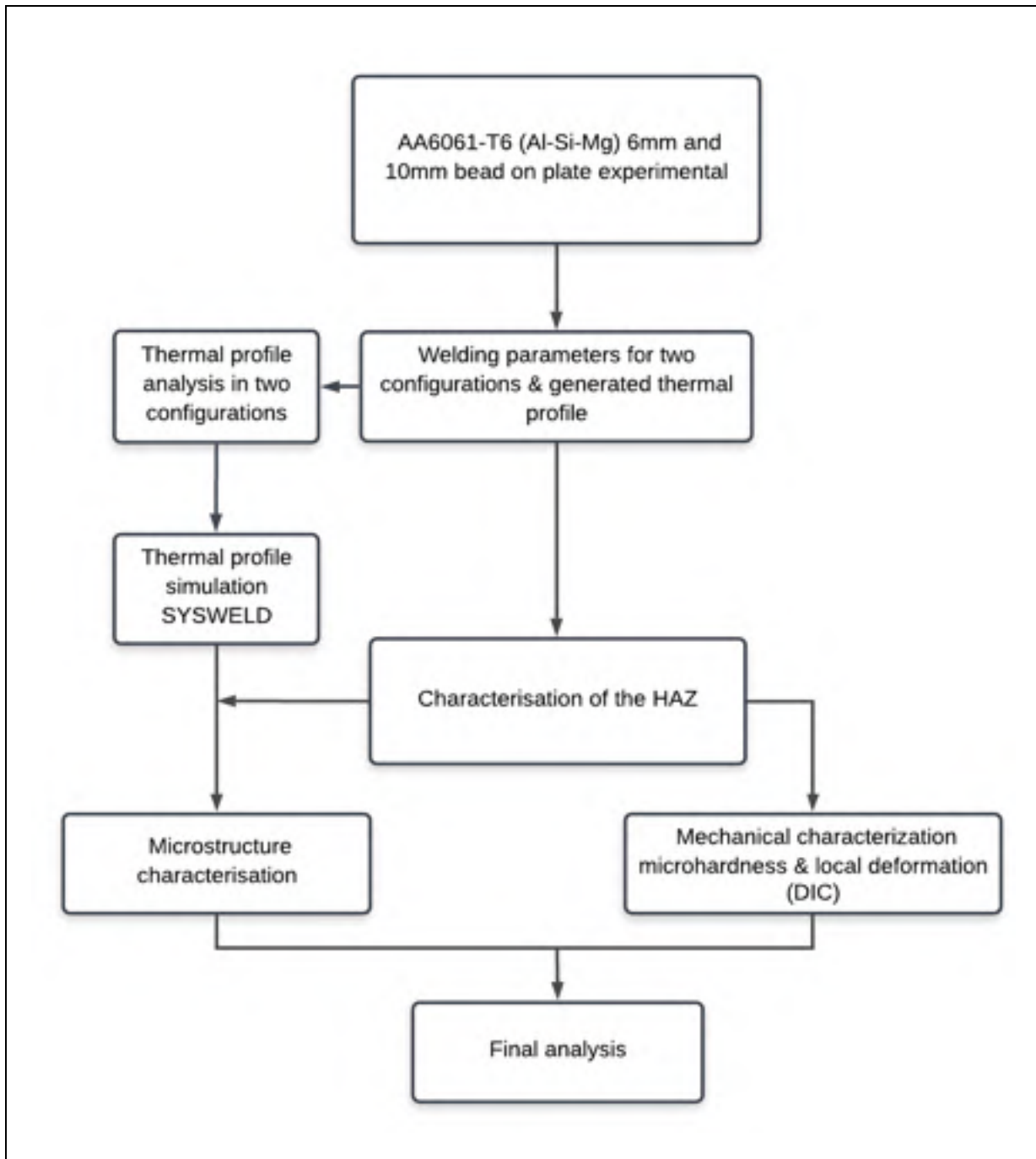


Figure 2.1 Schematic representation of experimental procedure

2.1 Welding Equipment and Material Used

As GMAW is a continuously fed wire process, it can easily be mechanised. The welding torch can be used at different welding currents, which are limited only by the welding power source. (GMAW), also known as (MIG), was the method used to generate all the welds in this study.

A DX-100 Yaskawa robot integrated with a standard Fronius Trans Plus Synergic 4000 welding power supply was used for this investigation as illustrated in Figure 2.2 a) and b). The system provides a smooth and steady arc with a pulsed current output and transfers the filler metal to the arc in fine droplets. The flexibility of robotic welding operation means that steadier weld quality can be obtained with fewer defects.

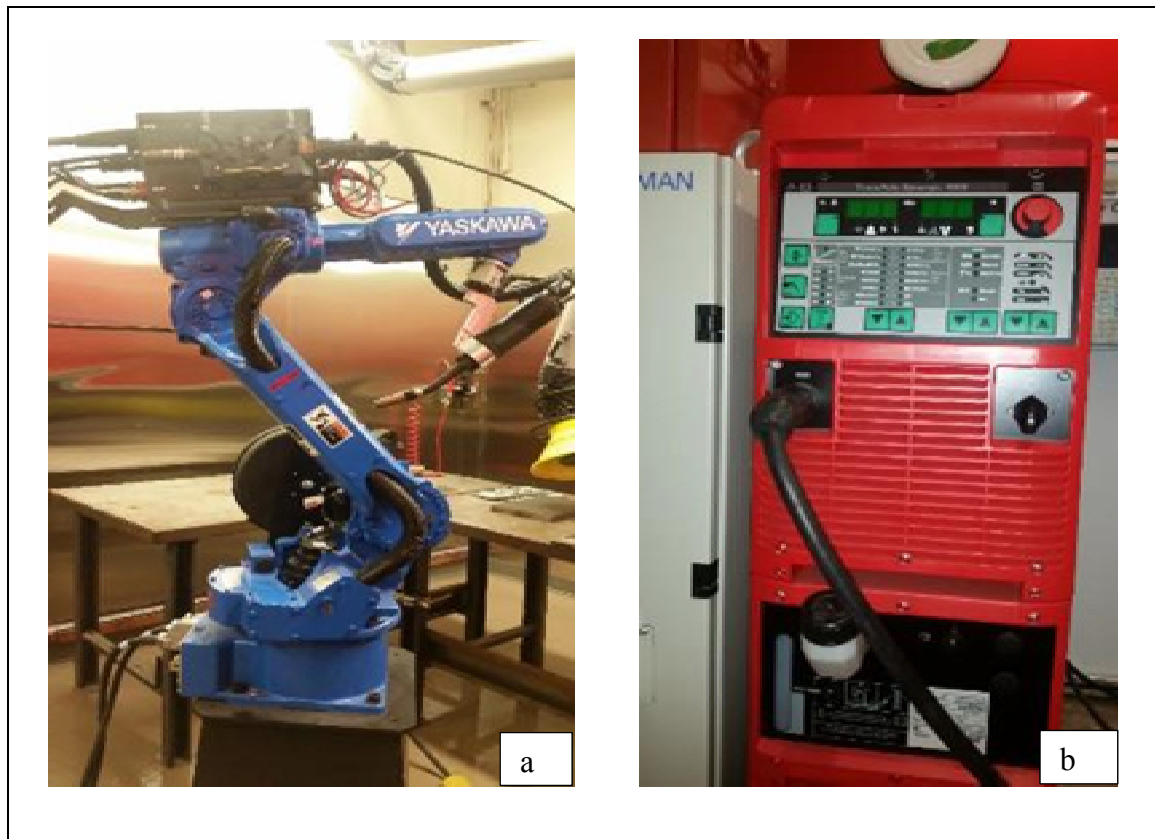


Figure 2.2 a) Welding robot, b) Fronius Trans Plus Synergic power supply

Material used

Plates of AA6061- T6 aluminum alloy sizes of (205mm x 50mm x 6mm) and (200mm x 50mm x 10mm) as shown in Figure 2.3 a) and b) were used in this study. The nominal chemical composition of the base material is listed in Table 2.1.

Table 2.1 Chemical composition of the base metals

	Al	Cu	Cr	Fe	Mn	Mg	Si	Zn	Ti
Base Metal (AA 6061)	98.6%	0.15%	0.004%	0.7%	0.15%	0.8%	0.4%	0.25%	0.15%

The T6 designation shows that the plates were solution heat treated and artificially aged to enhance their mechanical properties. The mechanical properties of the plates are provided in Table 2.2.

Table 2.2 Mechanical properties of base metal 6061-T6 and filler wire

Type of Material	YS (MPa)	UTS (MPa)	Elongation (%)	Hardness (VHN)
BM (6061-T6)	276	310	18	107
FW (AA4043)	70	145	22	47

Filler metal

AA4043 filler metal was used with a diameter of 1.2mm. The chemical composition of welding wire illustrated in Table 2.2 contains 5% silicon. This alloy is well known for its fluidity. Using AA4043 as a filler modifies the Si weight percentage in the fusion zone and as a result, the fusion zone is shifted to a composition that is less sensitive to hot cracking.

Table 2.3 Chemical composition of filler wire

	Al	Cr	Cu	Fe	Mn	Mg	Si	Ti	Zn
Filler wire (A4043)	Bal	---	0.3%	0.8%	0.05%	0.05%	5%	0.2%	0.1%

2.2 Sample preparation before welding

All required precautions were taken to avoid defects in the welding process such as lack of penetration, lack of fusion, and porosity. The surfaces of the specimens were cleaned using wire brush to remove the oxide surface film on the plate surfaces and were degreased using acetone. These samples were used directly after preparation to generate bead on plate welds.

2.3 Welding parameters and configuration

The welding parameters were selected for BOP experiments to form a pulsed GMAW arc with spray transfer mode. This mode provides full depth penetration, low porosity, no splatter and good cosmetic appearance which will be discussed in the following chapters. Table 2.4 shows the welding parameters that were used in two plate configurations.

Table 2.4 Welding parameters for two plate configurations

Welding parameters						Shield Gas	Feeding wire
	WFS mm/s	Voltage V	Ampere A	Welding speed mm/s	Welding angle	Argon	AA4043
Horizontal	271	23.2	174	15.2	15°	12 L/min	1.2mm
Vertical	127	22.2	154	16.8	15°	12 l/min	1.2mm

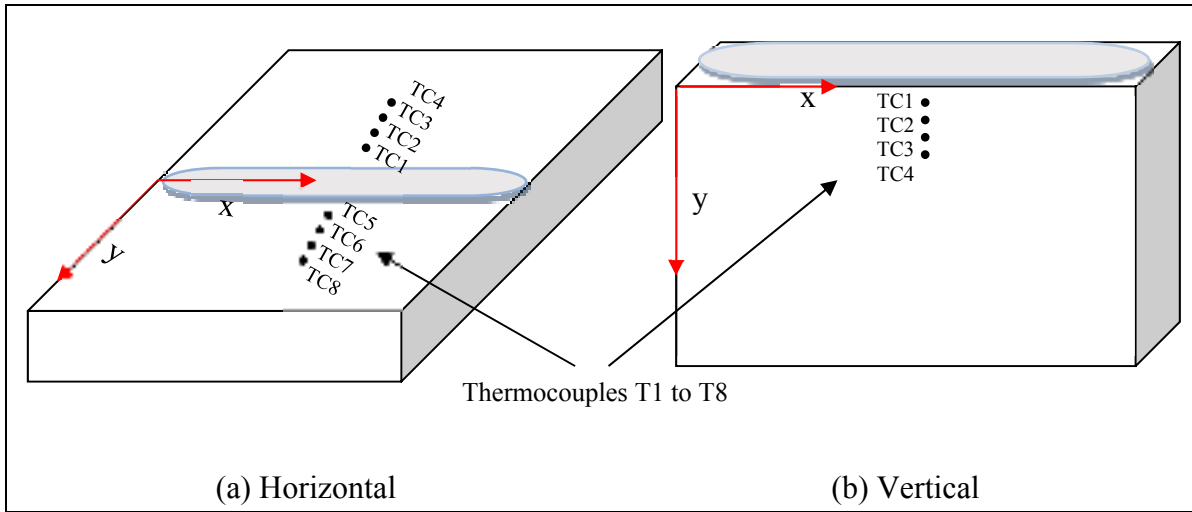


Figure 2.3 a) Horizontal welding configuration; b) Vertical welding configuration

Table 2.5 Location of thermocouples for temperature measurement

Horizontally welded plate			Vertically welded plate			
Thermocouples	X (mm)	Y (mm)	Thermocouples	X (mm)	Y (mm)	Z (mm)
TC1	100	5	TC1	100	3	-9
TC2	100	7	TC2	100	6	-9
TC3	100	9	TC3	100	9	-9
TC4	100	11	TC4	100	12	-9
TC5	100	-5				
TC6	100	-7				
TC7	100	-9				
TC8	100	-11				

X = distance from weld start
 Y = distance from welding center line

Table 2.5 and Figure 2.3 show the location of thermocouples (TCs) in two welding configurations. Each sample has 4 TCs on each side of the welding line.

2.4 Welding thermal cycle measurement

GRAPHTECH GL220A data acquisition system and thermocouples type K with diameter of 0.5mm were used to measure the temperature across the HAZ. The datalogger was set to record 10 readings per second from each thermocouple. Thermocouples were installed using a TW163/V variable energy TCs welding unit. Eight thermocouples were installed with four on each side of the welding line as shown in Figure 2.4.

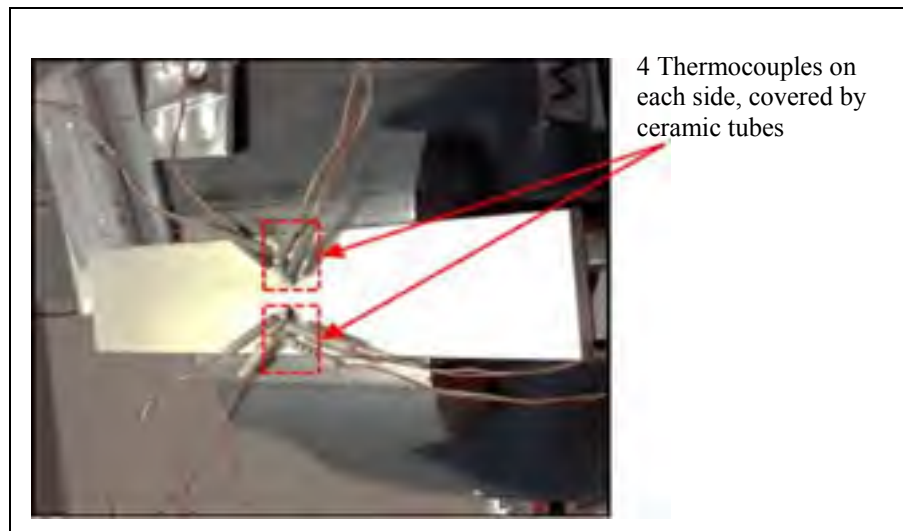


Figure 2.4 Location of installed thermocouples

The thermocouples record the temperature at the first point along the two wires. If any other intersection is there along the thermocouple wires, the thermal cycle measurement will not be accurate. Ceramic tubes are used to maintain the distance between the thermocouple wires and to protect the thermocouples from splatter. Table 2.5 shows the distance of each thermocouple from the welding line.

2.5 Procedures for characterisation of the HAZ

In order to examine the influence of welding thermal history caused by GMAW on microstructure and mechanical behaviour, an optical microscopy observation of the base metal structure, fusion zone and HAZ was performed. The mechanical characterisation of these regions was obtained by microhardness and micro-tensile tests using the DIC method.

2.5.1 Microstructure characterisation

The characterisation of microstructural was performed on test samples from each weld. Specimens of a cross section transverse to the welding line were prepared, as illustrated in Figure 2.5. The sample was sectioned with a META-CUT water-cooled abrasive cutter. The first 30 mm of the weld was discarded to avoid unsteady-state conditions.

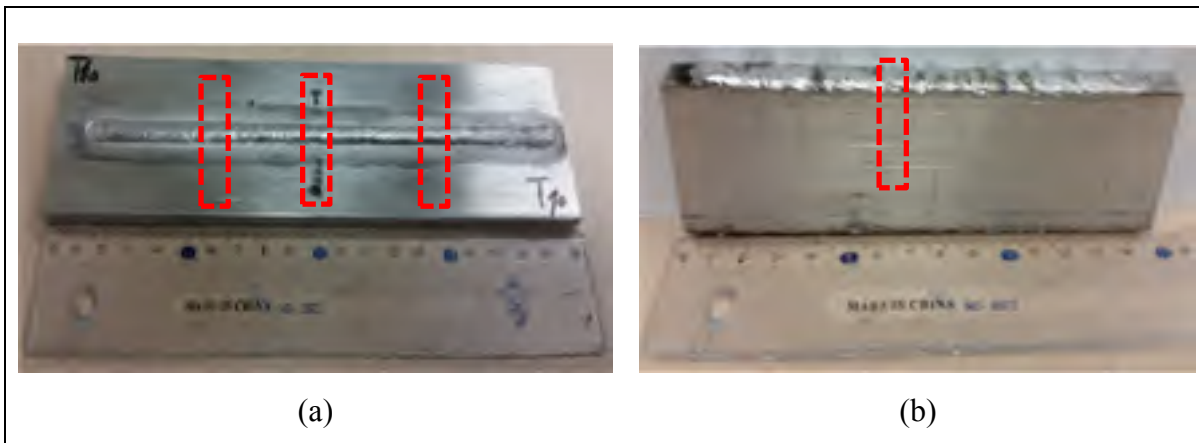


Figure 2.5 Extracted specimen from the a) horizontal welded plate, b) vertical welded plate

Next, the specimens were mounted and polished using a PACE TCH NANO 2000T polishing machine. The polishing was performed using grades of silicon carbide paper, from 400 up to 2400 grit, then followed by 3 μm , 1 μm and 0.05 μm size polishing pads in sequence.

Acetone and dried hot air were used to clean the samples in between polishing steps as shown in Figure 2.6. To prepare the specimen for optical microscopy, samples were etched with Caustic Sodium Fluoride Etch (93 mL water, 2 g NaOH, 5 g NaF). Specimens were examined with an Olympus Lext 4100 light microscope to observe the presence of defects and the main microstructural characteristics of the GMAW zones: base metal, heat affected zone, partially melted zone, and fusion zone. Intercept technique used to measure the change in grain size cross HAZ.



Figure 2.6 Polished and etched sample for microstructure characterisation extracted from horizontally welded plate

2.5.2 Mechanical Characterisation

Microhardness and micro flat tensile tests using the DIC technique were performed on specimens extracted from welded samples to characterise the mechanical properties of the FZ, heat affected zone and base metal.

2.5.2.1 Microhardness Tests

Microhardness measurements were carried out on the mounted specimen at room temperature in a cross section transverse to the welding line to cover all zones affected by the thermal cycle and the parent metal. Automatic microhardness Clemex CMT used to measure

the hardness with a dwell time of 15 sec and load of 100 g according to ASTM E92 standard procedure for Vickers hardness testing of metallic materials.

The parameters were kept constant for all indentations with 250 μ m distance between each indentation. The microhardness measurement was analysed as a function of its distance from the bead center. A 2D map was generated to cover all zones in the cross-section and to investigate the hardness distribution. Figure 2.7 below shows the indentation distribution.

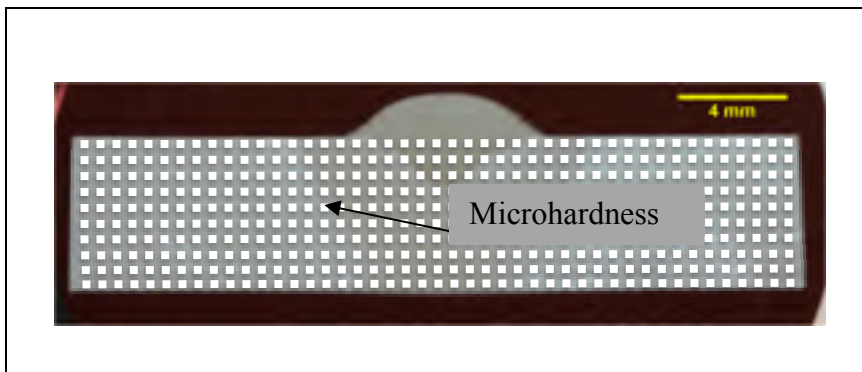


Figure 2.7 Distribution of microhardness indentation

2.5.2.2 Micro flat tensile test with DIC transverse to welding direction

Digital image correlation is an image analysis method where a series of images is compared to a reference image at various stages of a stress strain test. This correlation method confirmed a high accuracy of local deformation measurements, demonstrated mainly by speckle pattern and illumination [47].

Micro-tensile specimens transverse to the welding line were extracted from a welded plate and used in this investigation. A diagram of micro-tensile samples is shown in Figure 2.8. Dog-bone sub-size tensile samples were machined from the welded plates using a CNC machine. The specimen machined normal to the welding line is shown in Figure 2.8.

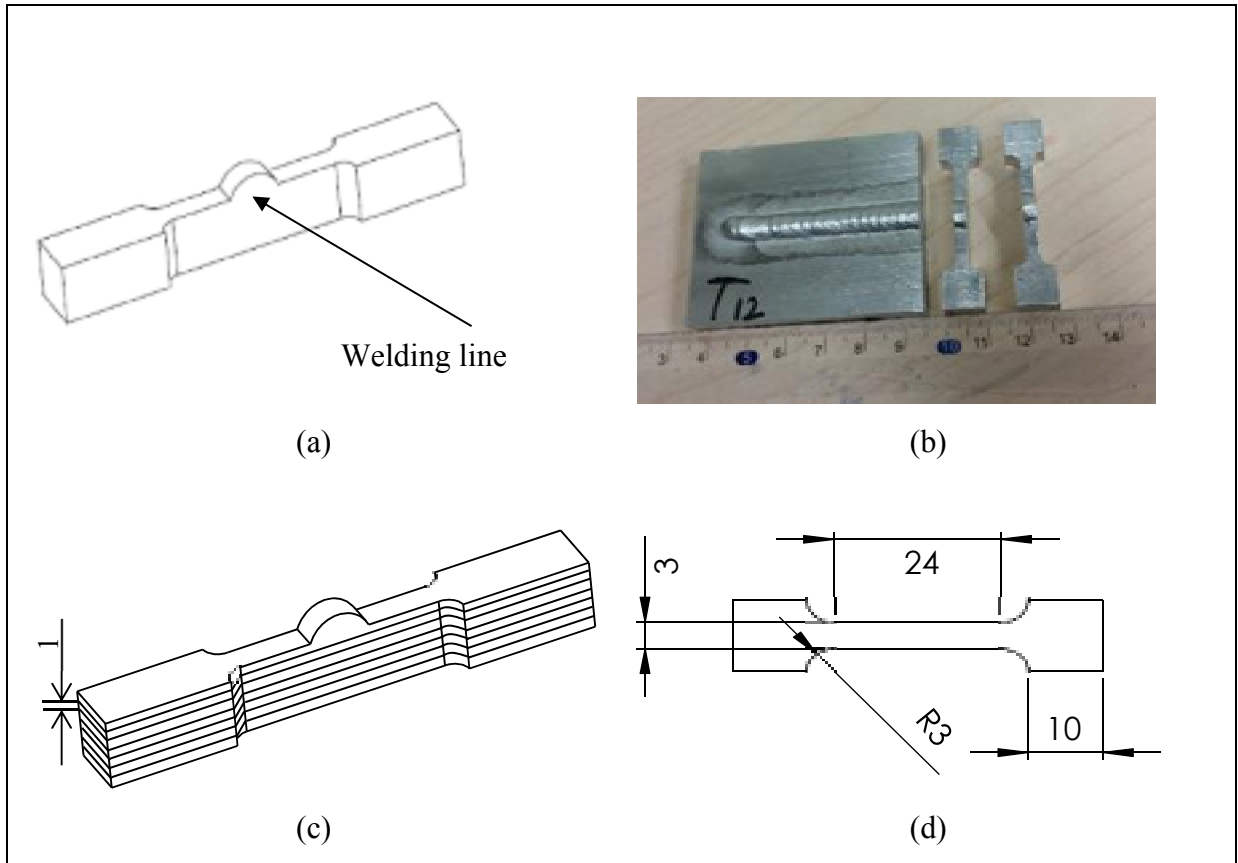


Figure 2.8 DIC of machined samples transverse to the weld direction, a) and b) machined specimen, c) and d) the extracted samples

A 24 mm gauge length was chosen to cover different areas of the sample such as the BM, HAZ, PMZ, and FZ. A series of specimens were extracted from the machined part using precision cutting machine. The extracted samples were approximately 1mm thick with care taken to avoid any deformation or sequencing errors. Figure 2.8 illustrates the cutting arrangement for the machined sample.

Speckle with high contrast pattern is critical to accurately determine the local deformation of the sample. The speckle patterns were produced using black and white paint and a mini air brush gun to obtain a very fine pattern as illustrated in Figure 2.9. The fine speckle pattern minimises noise and increases track certainty. The mechanical properties of the base metal were determined using a coupon extracted from the base metal as shown in Figure 2.8.

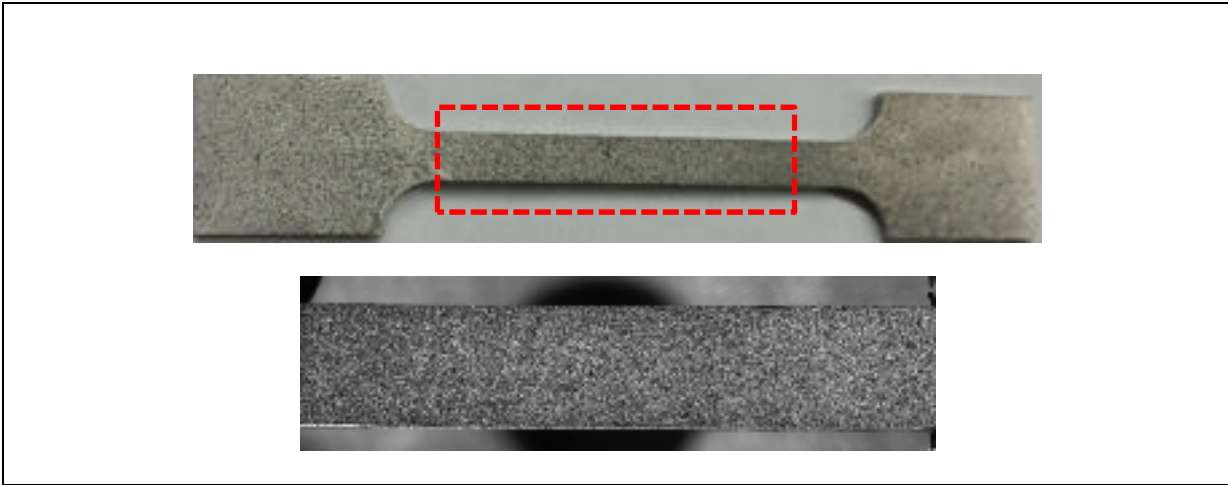


Figure 2.9 Speckle patterns for DIC

Micro flat tensile tests were performed using a 10 kN tensile machine (Weisse & Kamrath) under crosshead velocity control (approximately $2.1 \times 10^{-4} \text{ s}^{-1}$). The displacement was documented to within $1 \mu\text{m}$ of accuracy, and non-contact laser extensometers were used to measure elongation during the test. A high resolution camera was used to record images (at a rate of 1 image per second) simultaneously during the tensile test as shown in Figure 2.10. GOM correlation software was used to calculate the in-plane displacement [48]. The displacement calculated from the image correlation was used to obtain the in-plane local strain field.

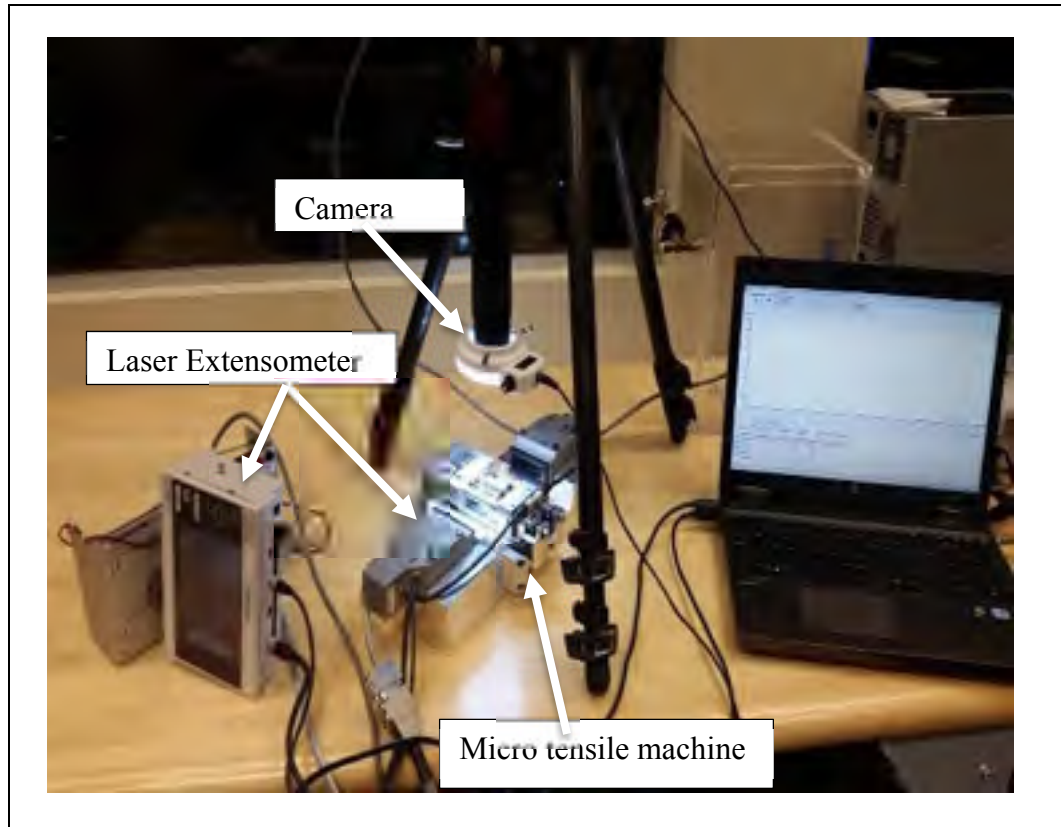


Figure 2.10 Set up of micro tensile test with DIC

2.5.2.3 Micro flat tensile test for samples extracted parallel to welding direction

Micro flat tensile specimens parallel to the welding line were extracted from the welded plate and used in this investigation. A diagram of the flat micro-tensile samples is given in Figure 2.8. Dog-bone sub-size tensile specimens were machined using CNC as shown in Figure 2.11. Different samples were extracted from different subzones in the HAZ, and every specimen presents a different thermal history based on its distance from the FZ.

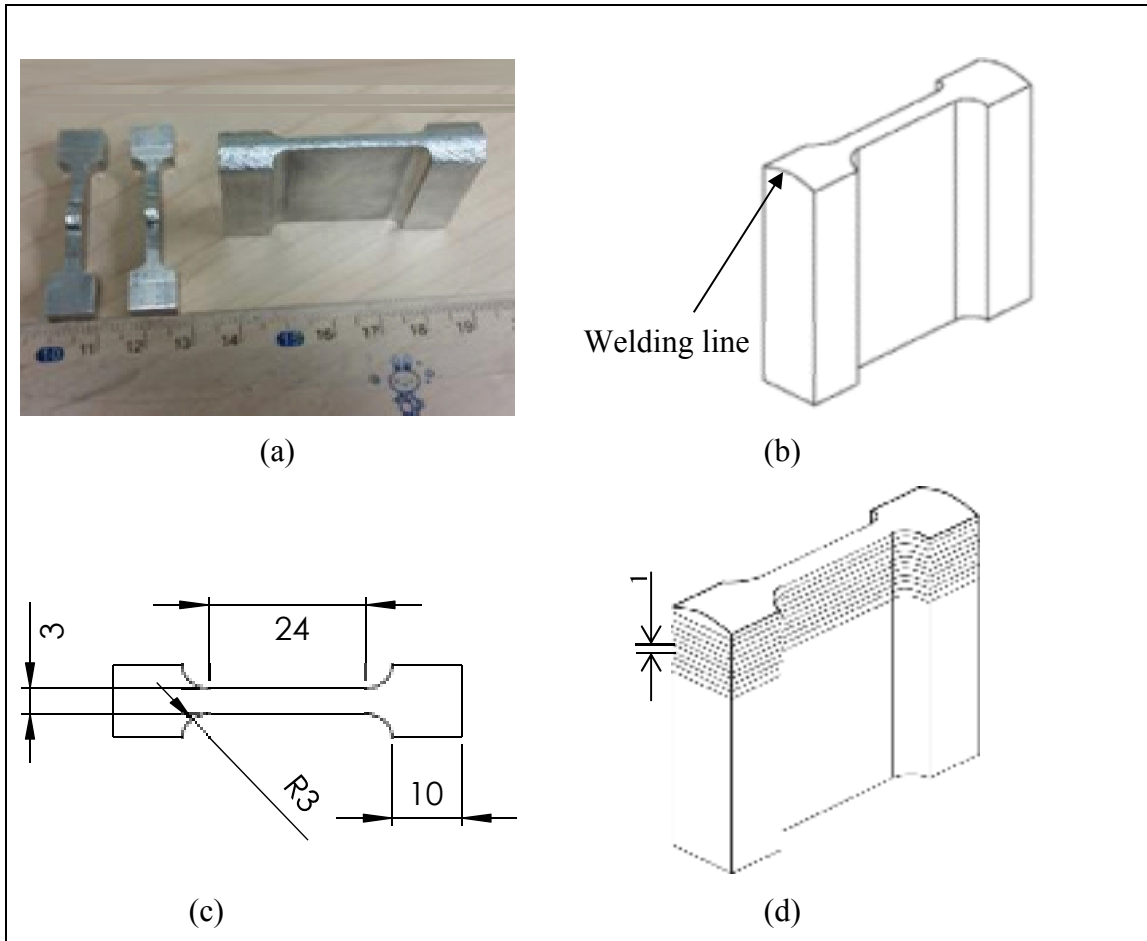


Figure 2.11 HAZ extracted micro-tensile specimens parallel to welding line, dimensions in mm, a) and b) machined specimen, c) and d) the extracted DIC samples

CHAPTER 3

THERMAL ANALYSIS OF TWO GMAW CONFIGURATIONS

3.1 Welding thermal profile

This chapter presents the experimental and simulation results of the welding thermal profile as taken from thermocouples compared with simulation results for two welding configurations. Because the temperature in the HAZ of the GMAW tests remains well below 850°C, the experimental method used (K-type, Chromel - Alumel) thermocouples (TCs). Horizontal configuration thermal profile. Figure 2.3 shows the position of TCs used to record the welding thermal profile. These TCs were welded on the upper surface of the welded plate in horizontal configurations on both sides of welding line. It is to be noted that TC1 to TC4 were on one side and TC5 to TC8 were on the other side of the welding line, and the two sets of TCs have the same positions, therefore they should ideally show the same thermal profile. However, there were slight differences observed for thermocouples that had corresponding locations. These differences may be attributed firstly to the time delay response of 20 ms of the TCs and, secondly, to the variance in total heat energy absorbed by the test plates. Figure 3.1 illustrates the experimental thermal cycles for the eight TCs on both sides of the welding line.

Table 3.1 Standard deviation of peak temperature in horizontally welded plate

Distance of TC from Welding line	5mm TC1-TC5	7mm TC2-TC6	9mm TC3-TC7	11mm TC4-TC8
Max T °C	453	331	276	239.8
STDEV (%)	6.5	6.1	5.2	4.2
Heating rate (°C/s)	156	102	81	43
Cooling rate (°C/s)	-13.6	-6.8	-4.7	-2.5

Table 3.1 shows the standard deviation of thermal history for the horizontal plate with the 26 TCs obtained from the three tested samples (8 TCs per plate). It is to be noted that the temperature measured near the FZ (TC1&TC5) which is close to the heat source has a higher standard deviation of 6.5%. This is due to external effects such as the shielding gas, compared to TC4 & TC8 which are located at 13 mm far from the welding line.

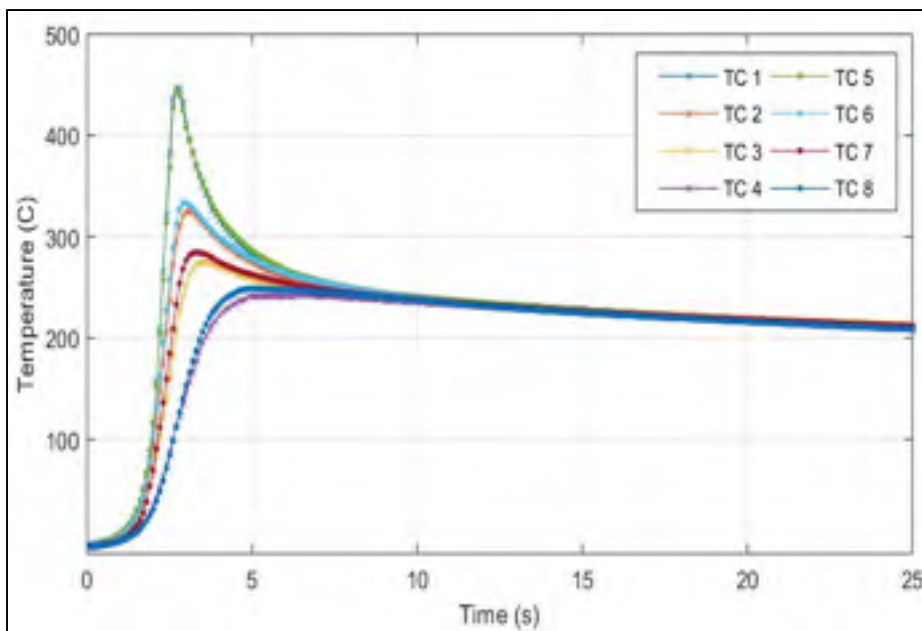


Figure 3.1 Experimental thermal profile recorded by four TCs on each side of welding line in horizontally welded plate

3.1.1 Vertical configuration thermal profile

This test case involved welding the plate in a vertical position. Thermocouples were placed on both sides of the plate at distances from the edge of the plate of 3mm, 6mm, 9mm, and 12 mm respectively as shown in Figure 2.3. The thermal profile for the eight TCs, four on each side, are illustrated Figure 3.2. The figure shows almost identical thermal history with respect to the distance of each TC, and this is owing to the steady welding speed of the robotic apparatus and less due to external effect because the TCs were located on the side of welded

plate. The peak temperature recorded by TCs in the vertical plate is lower than that of the horizontal plate considering the distance from the welding center line and this affects the size of the HAZ.

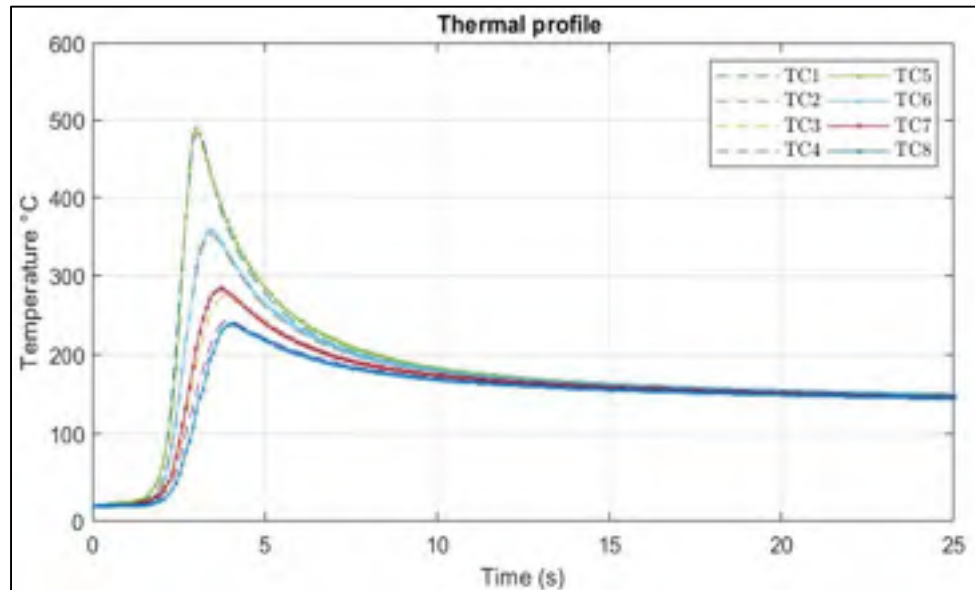


Figure 3.2 Experimental thermal profile of vertical plate

The standard deviations of the three tested samples and 24 TCs are shown in the Table 3.2. It is noted that the samples welded in the vertical configuration have lower standard deviation than the horizontally welded plates in terms of peak temperature as the former is less affected by external factors such as shielding gas and arc.

Table 3.2 Standard deviation of peak temperature in vertical welded plate

Distance of TC from Welding line	3mm TC1&TC5	6mm TC2&TC6	9mm TC3&TC7	12mm TC4&TC8
Max T	492	358	276	223
STDEV (%)	6	5.5	4.7	3
Heating rate (°C/s)	245	163	109	75
Cooling rate (°C/s)	-52.7	-40.7	-23.9	-22.2

3.2 SYSWELD models

The finite element welding model may help to predict the mechanical and metallurgical properties of the material by taking into consideration the interactions between the heat transfer and phase transformations. The interaction between thermal-metallurgical, thermal-mechanical and mechanical-metallurgical reactions is linked by weak or strong couplings as shown in Figure 3.3.

The coupling thermomechanical action occurs when thermal expansion produces internal stresses, and when plastic deformation releases heat. Thermo-metallurgical coupling occurs when the elevated temperature changes the microstructure, inducing phase changes, and conversely, when the metallurgical reactions release or absorb latent heat. Mechanical-metallurgical coupling occurs when the state of stress impacts the kinetics of phase changes, and when the metallurgical impacts upon mechanical properties such as hardness.

SYSWELD is a commercial finite element software designed by ESI Group specifically for welding processes and it has tools devoted to simulating welding processes such as pre-defined moving heat sources, including the conical Gaussian 3D heat source model. It allows us to simulate and analyse the link between the microstructure, and thermal, and mechanical interfaces by modeling the distribution of the temperature as a function of time, distortions and metallurgical properties such as phase transformation [49].

In this study, the coupled thermal mechanical analysis provided by SYSWELD was used to performed GMAW simulation. The thermal analysis results (thermal cycle distribution) were compared to experimental thermal profile.

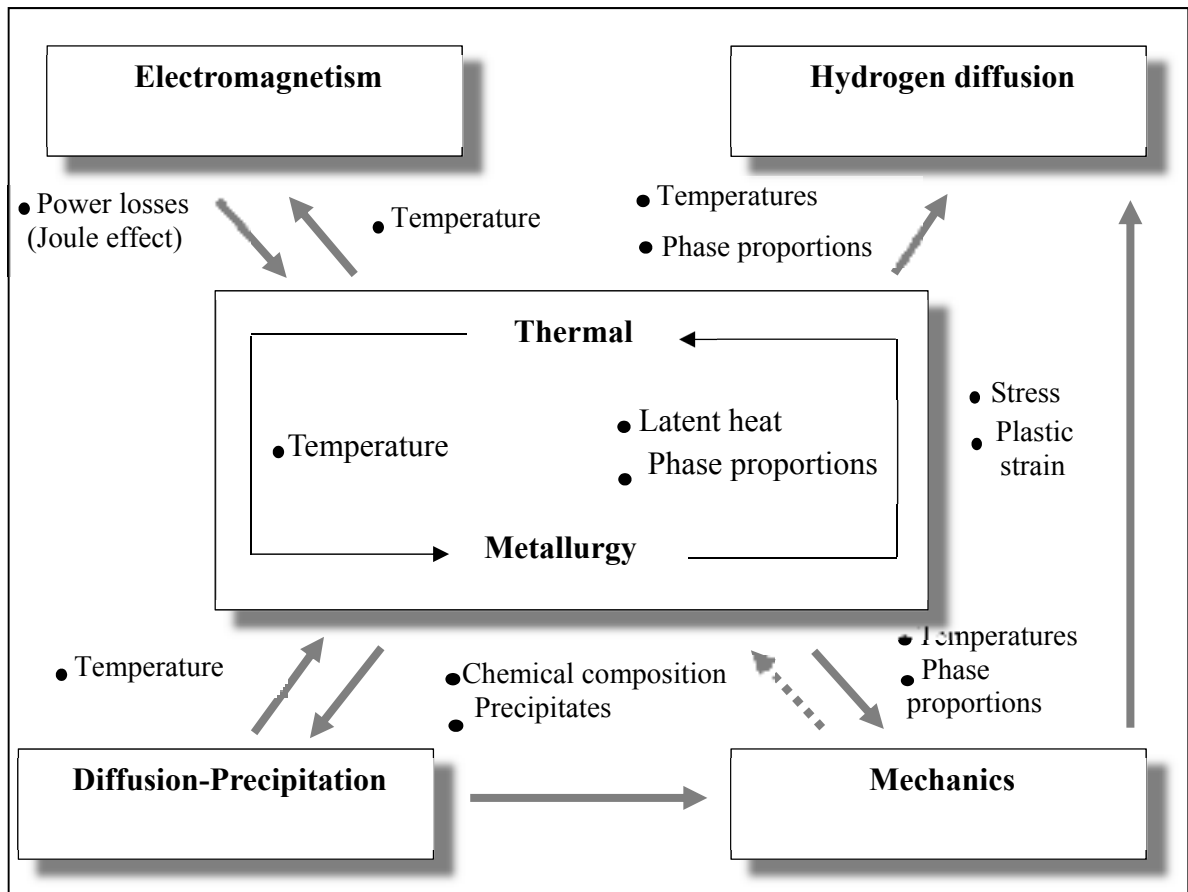


Figure 3.3 SYSWELD simulation process

3.2.1 Heat source used in SYSWELD

Three predefined shapes of heat source are available in SYSWELD: A volumetric conical heat source, double ellipsoid heat source and Gaussian heat source. This investigation applied a conical Gaussian volumetric as shown in Figure 3.4.

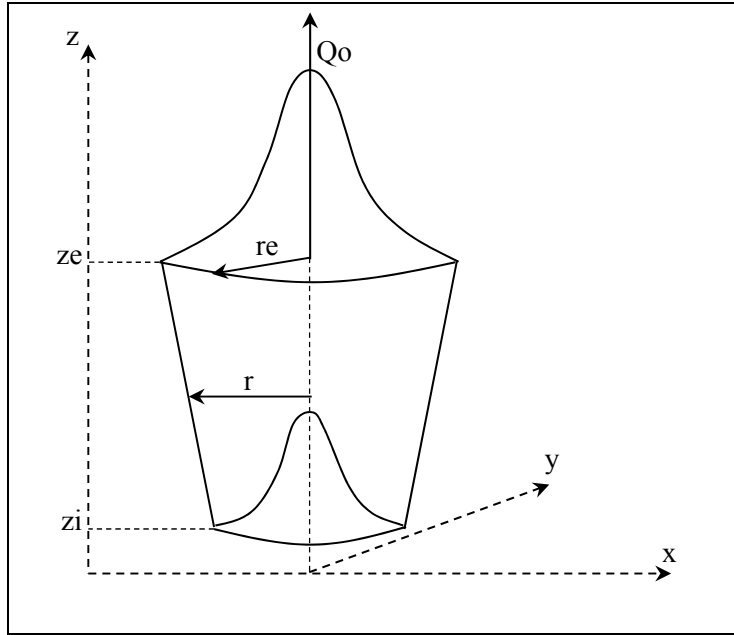


Figure 3.4 Conical Gaussian volumetric heat source model

The heat density of the Gaussian distribution is expressed as follows:

$$Q(r, z) = Q_0 * e^{\left(-3 \frac{r^2}{r_0^2}\right)}; \quad (3.1)$$

$$r^2 = (x - x_0)^2 + (x - x_0 - v * t)^2; \quad (3.2)$$

$$r_0 = r_e - \frac{(r_e - r_i) * (z_e - z) + z_0}{(z_e - z_i)}; \quad (3.3)$$

where Q_0 is maximum thermal density (W / m^3), z and r are the radial coordinates of the thermal density (m), x_0 , y_0 and z_0 is the local reference of the thermal source (m), v is the velocity (m/s) and t is the time (s).

3.2.2 Mesh and boundary condition

In this study, the fine mesh around the welding trajectory is important because the thermal gradient is high in this zone. A mesh size of 1 mm around the melting zone and 3mm for the area around the HAZ where the thermal cycle is not high enough to change the material properties is illustrated in Figure 3.5. An attempt was made to use a smaller mesh of 0.25mm and 0.5mm in order to compare with the thermal and metallurgical results obtained using the 1mm mesh, but this finer resolution analysis caused the simulation time to double and provides approximately the same result. The plates were fixed far from the thermal source to reproduce boundary conditions identical to the experimental boundary conditions for the two configurations, to eliminate the mechanical effect on the metallurgical properties and to produce the same thermal history.

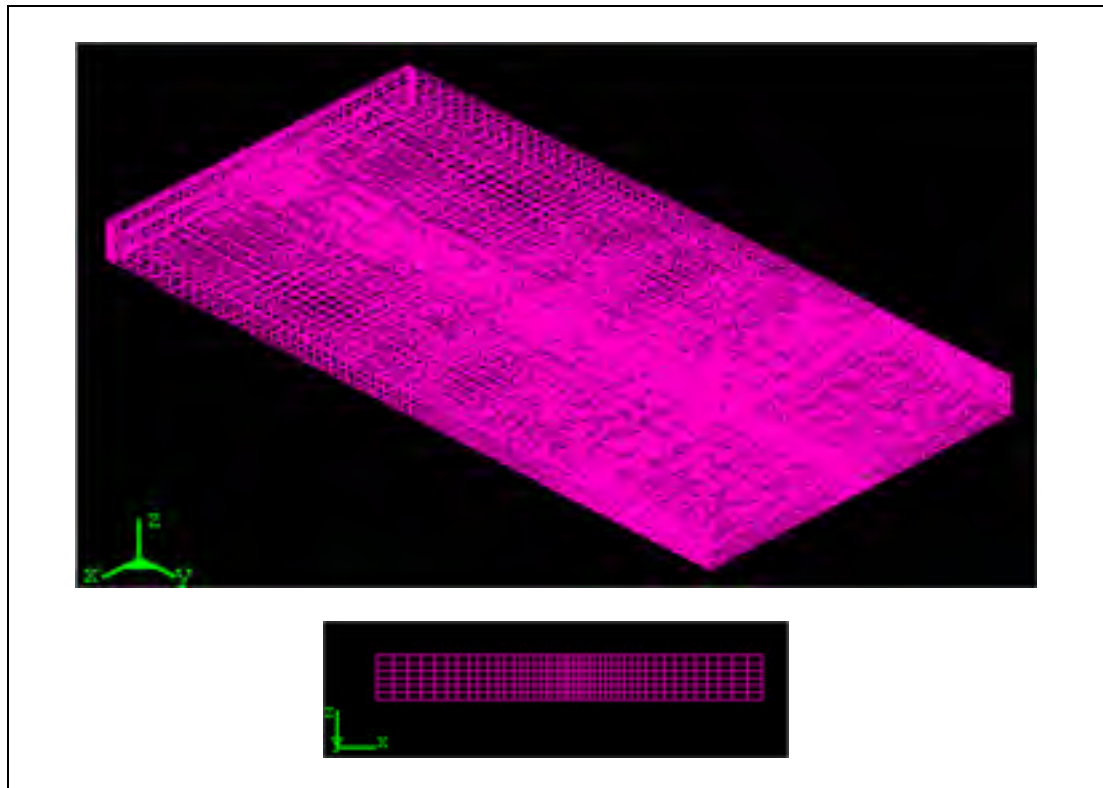


Figure 3.5 Mesh for simulation (with 1mm size in the HAZ, and 3mm outside the HAZ)

3.2.3 Calibrating the heat source of the vertical plate

The heat source parameters shown in Figure 3.6 have been used to reproduce similar thermal profiles and melting pool size to those that were experimentally observed, by adjusting the predefined 3D conical Gaussian heat source. The calibration was performed in two configurations: a vertically welded plate and a horizontal welded plate.

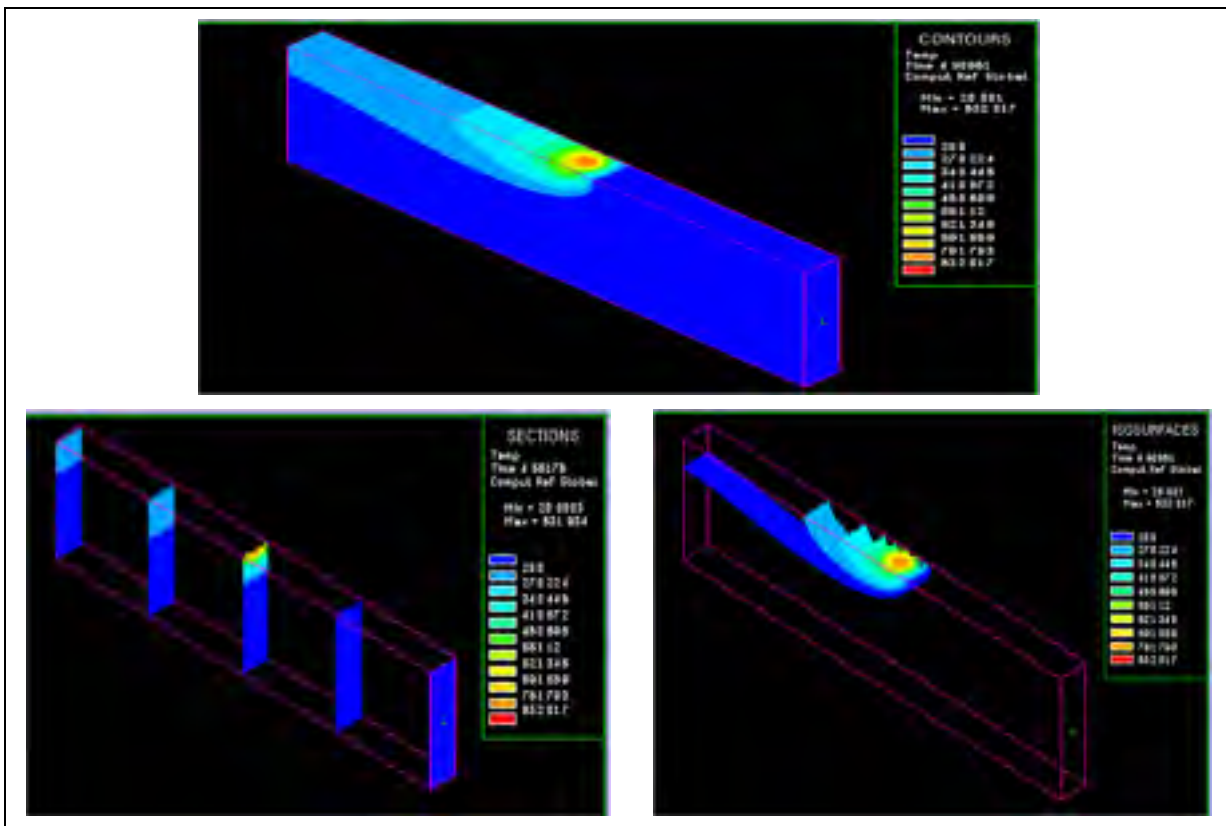


Figure 3.6 Thermal distribution at the moment when the heat source was in the center of the part

Table 3.3 Gaussian 3D conical heat source parameters for vertical plate

Welding speed (mm/s)	Q_0	r_e	z_e	r_i	z_i	x	y	z	ay	Power
16.8	53.6	6	3	5.5	2	0	0	0	0	2460

3.2.3.1 Thermal profile

The 3D conical Gaussian model produced a thermal profile that closely matched the experimental results as shown in Figure 3.9. The differences in peak temperature were -5.2%, -4.4%, -2.8%, -1.7% in the TCs as compared to the experimental thermal profile as illustrated in Table 3.5 and Figure 3.9.

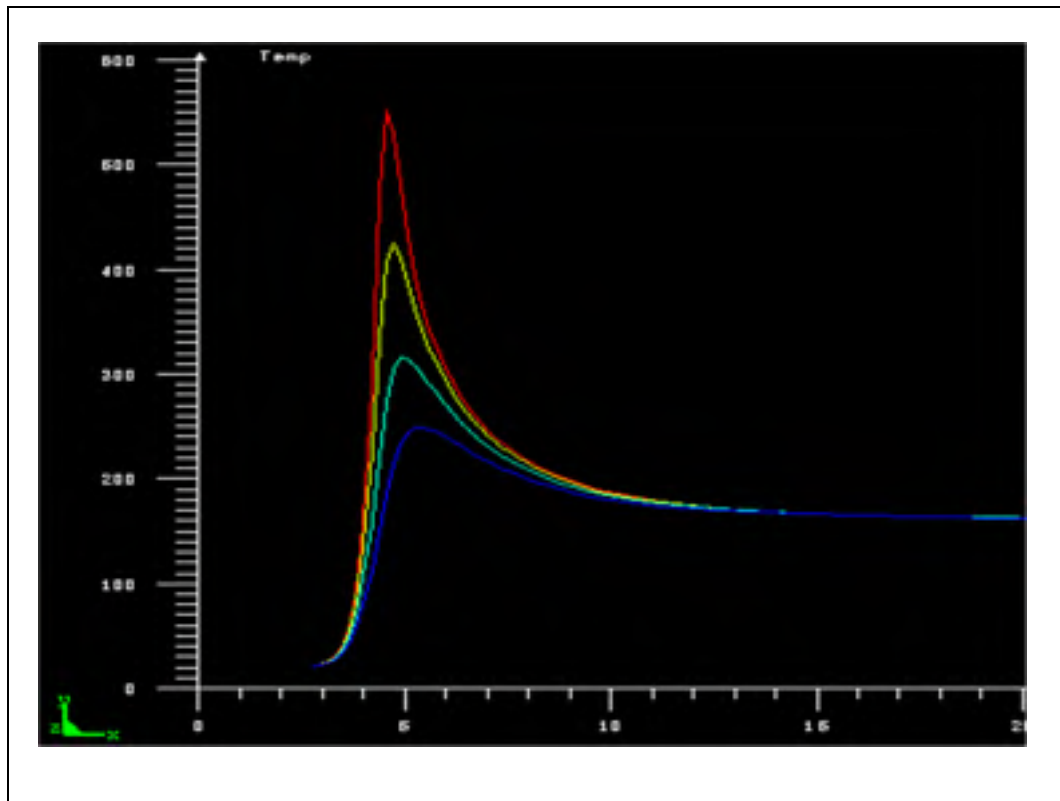


Figure 3.7 Simulated thermal profiles at the same locations as the 4 thermocouples

The heating and cooling rates in Table 3.4 show that the differences in heating rate between experimental and numerical results are -8%, -7%, -6.5%, -4% respectively at different TCs. Based on this finding, it was concluded that the calibrated thermal model represents well the experiment.

Table 3.4 Heating and cooling rates in vertical welded plate

	TC1	TC2	TC3	TC4
Heating rate Exp (°C/s)	245	163	109	75
Heating rate FE (°C/s)	265	175	116.5	78
$\frac{Exp-FE}{Exp}\%$	-8%	-7%	-6.5%	-4%
Cooling rate Exp (°C/s)	-52.7	-40.7	-23.9	-22.2
Cooling rate FE (°C/s)	-55.5	-42	-25	-21
$\frac{Exp-FE}{Exp}\%$	5.3%	-3.2%	4.6%	5.4%

Melting zone

The melting temperature of 6061-T6 aluminum is around 650°C. A geometric comparison of the melting zone shows a close resemblance to the shape of the melting zone obtained by the numerical simulation and the melting zone observed in the cross-section of the actual welding, as in Figure 3.8.

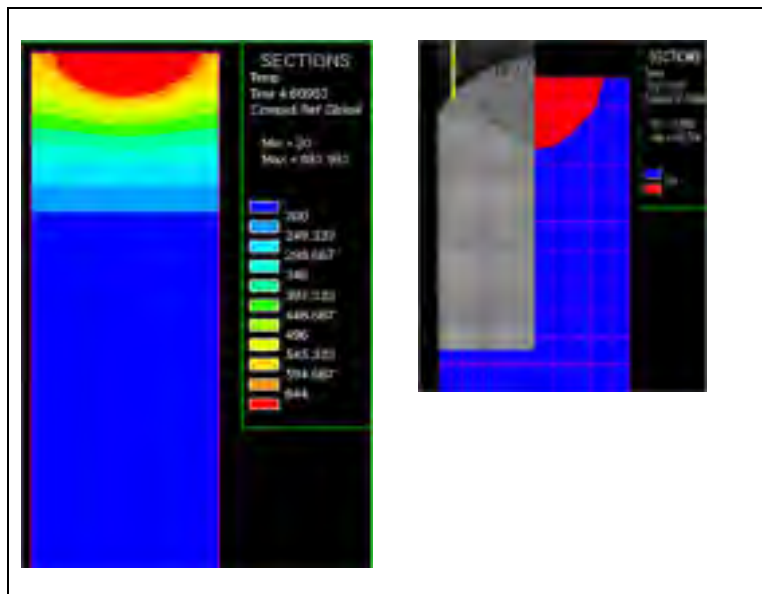


Figure 3.8 Fusion zone of vertical welded plate

Moreover, comparing the temperature distribution and the size of the HAZ obtained by FEA with the measured hardness profile shows good agreement. This will be discussed in more detail in Chapter 4.

3.2.3.2 Comparison between experimental and FE thermal profile

Figure 3.9. (a) illustrates the thermal profile calculated by finite element simulation model compared with the experimental result. It is clear that the result has generally acceptable agreement; however, there are noticeable differences in the peak temperature, and this difference increases as the distance from the welding center line decreases.

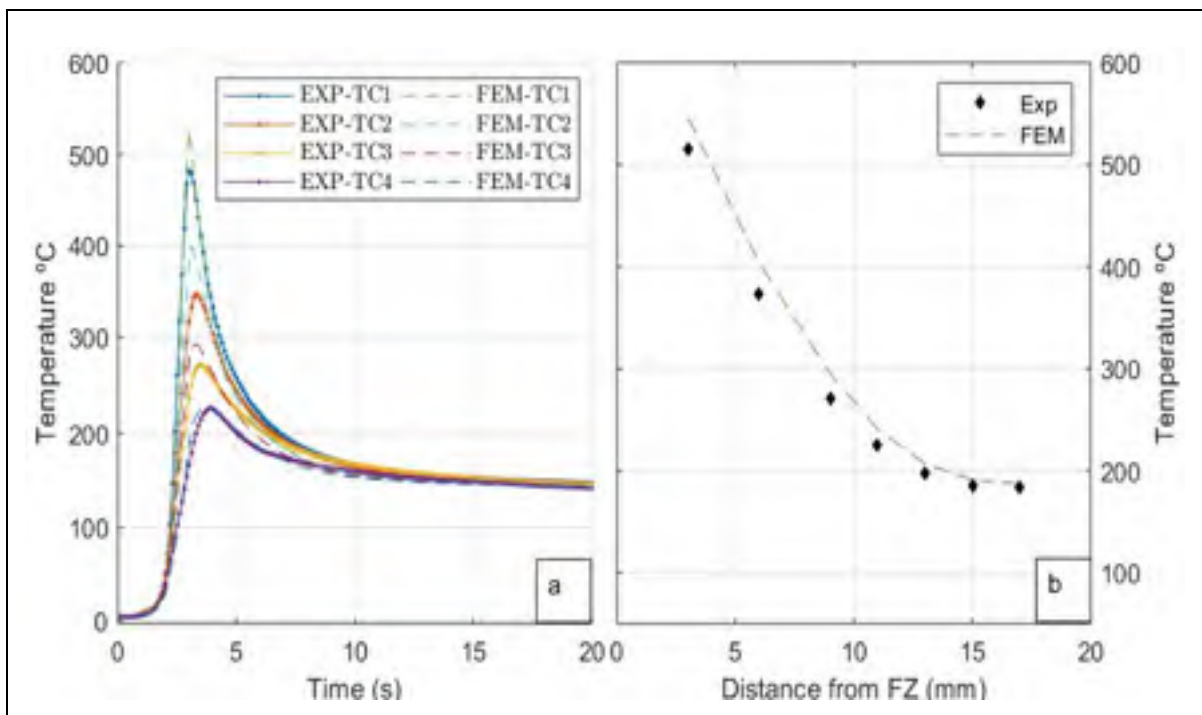


Figure 3.9 Thermal profile of vertical plate, a) thermal profile comparison between experimental results and finite element simulation of points at different distances from the welding center line, b) peak temperature comparison

Table 3.5 Difference in % of peak temperatures in vertically welded plate

TCs	Max °C TC1	Max °C TC2	Max °C TC3	Max °C TC4
Exp	492	358	276	223
FEA	517	374	284	227
Difference in%	-5.2	-4.4	-2.8	-1.7

Table 3.4 shows that the maximum temperature of the point located at 3mm distance from the edge of melting zone was 508°C. It is worth noting that the relationship between temperature and distance is nonlinear, owing to the nonlinear difference of the material's thermal properties at different temperatures. The region near the FZ boundary experiences a high temperature gradient (up to 42°C/mm).

3.2.4 Adjusting heat source of the horizontal plate

3.2.4.1 Thermal profile

The same 3D conical Gaussian heat source used in the vertically welded plate was used for the horizontally welded plate. The FE thermal profile shows similar results with differences of 6.36%, 4.5%, 3.1% and 2.5% respectively compared to thermal profiles recorded by experimentation.

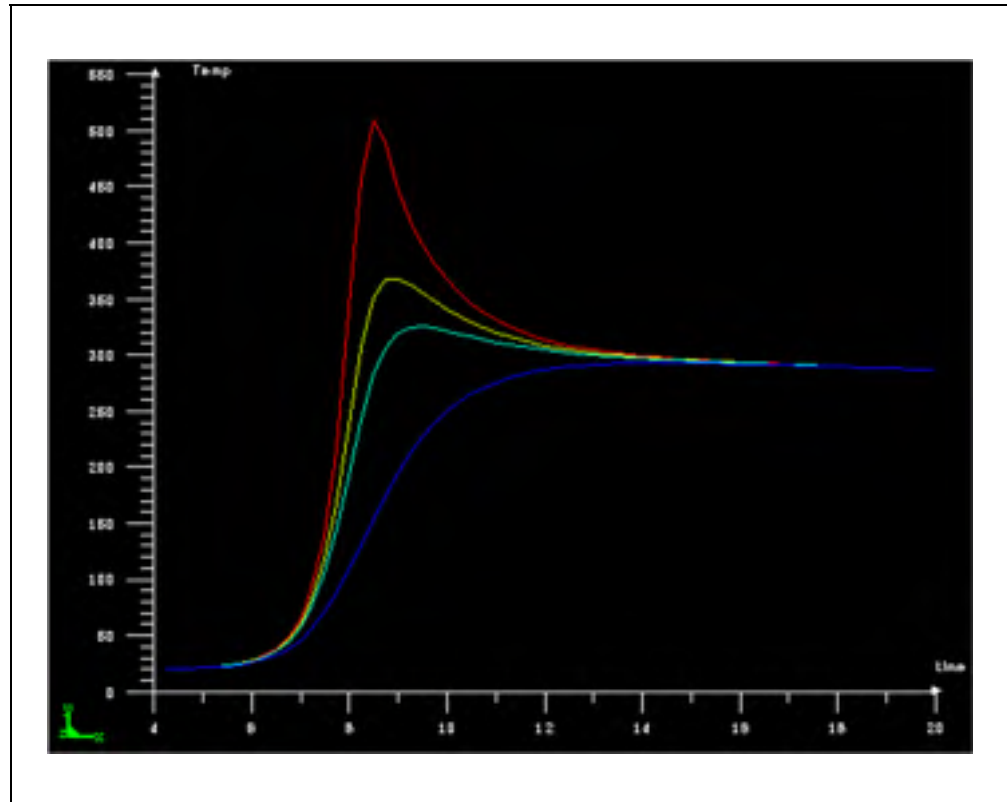


Figure 3.10 Thermal profile of 4 nodes in the horizontally welded configuration corresponded to the location of TCs

The difference in heating rate was 5.5%, 7.5%, 10.7% and 11.6% respectively as shown in Table 3.7. When the heating source passed the TCs plane, the cooling began with the values presented in Table 3.7. Based on this result, the calibrated heat source reproduces the thermal profile very close to the experimental work.

Table 3.6 Gaussian 3D conical heat source parameters for horizontal plate

Welding speed (mm/s)	Q_0	r_e	z_e	r_i	z_i	x	y	z	ay	Power
15.2	32.7	6	3	4	1	0	0	0	0	3150

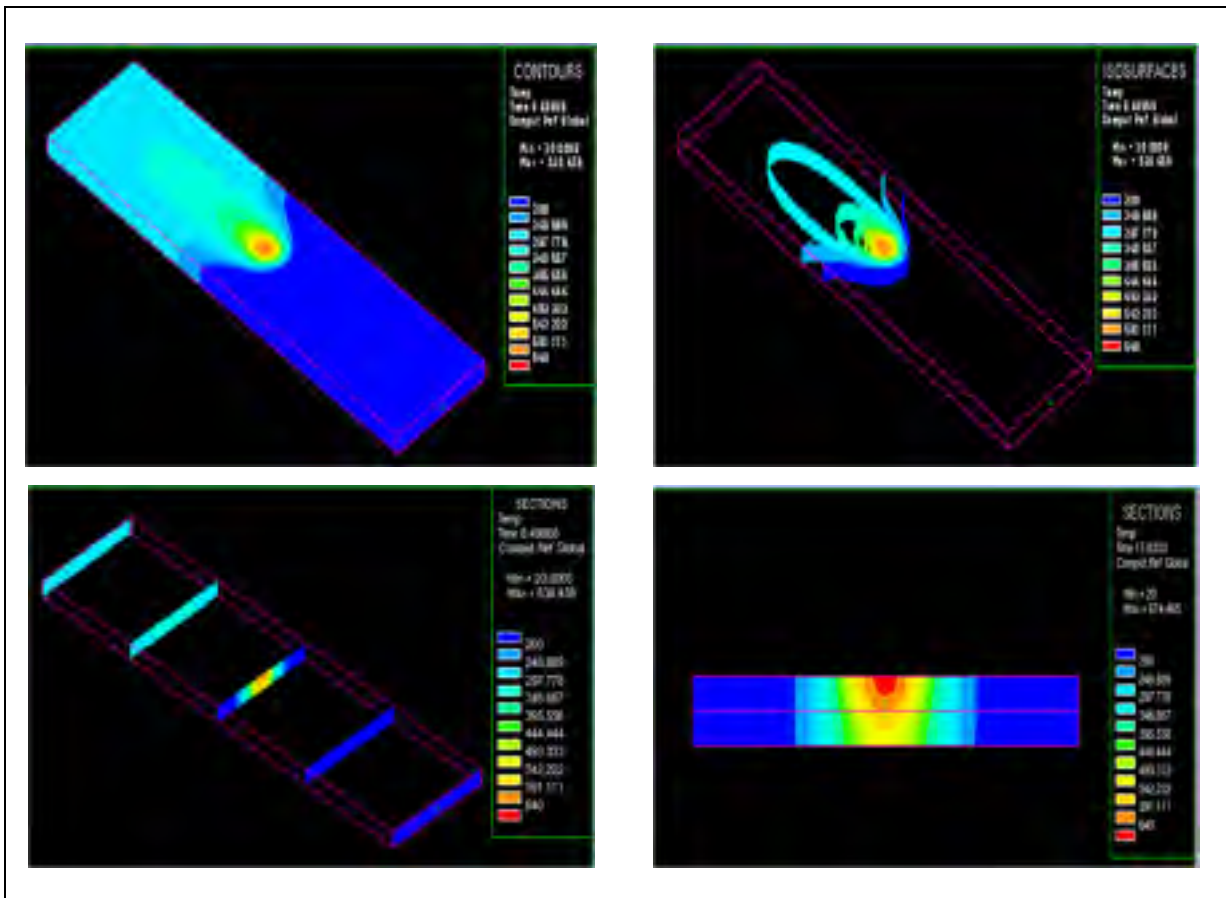


Figure 3.11 Thermal distribution in horizontal welded plate

Table 3.7 Heating and cooling rates in horizontal welded plate

	TC1	TC2	TC3	TC4
Heating rate Exp (°C/s)	162	106	84	43
Heating rate FE (°C/s)	153	98	75	38
$\frac{Exp-FE}{Exp} \%$	5.5%	7.5%	10.7%	11.6%
Cooling rate Exp (°C/s)	-6.3	-5.2	-3.6	-2
Cooling rate FE (°C/s)	-5.9	-4.9	-3.4	-1.9
$\frac{Exp-FE}{Exp} \%$	6%	5.7%	5%	5%

Molting zone

The comparison of melt pool shape in Figure 3.12 indicates that the melting zone obtained from the simulation resembles the measured fusion zone obtained by experimentation, therefore the simulated fusion zone shapes validate the implementation of the heat source model used in this study.

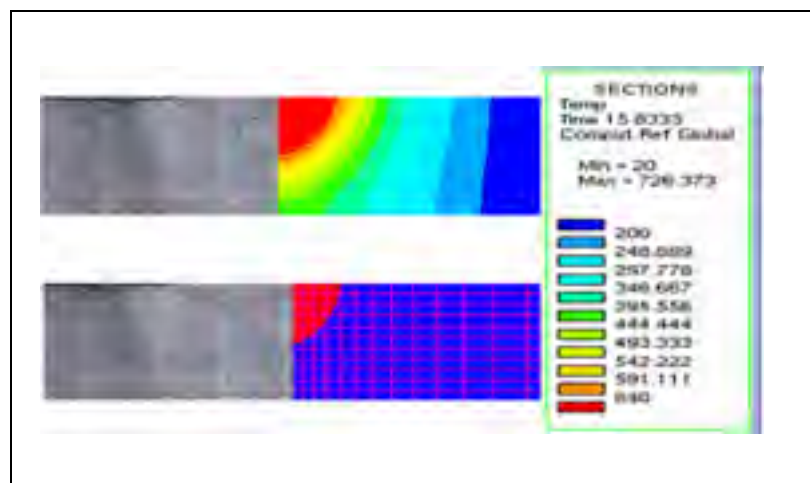


Figure 3.12 Melting zone

3.2.4.2 Comparison between experimental and FE thermal profile

Figure 3.13 shows the weld thermal profile measured experimentally compared with the numerical simulation result for the horizontal configuration. It shows that the heat source used in numerical provides good approximation of 8.3 % difference compared to the experimentally obtained results. Table 3.8 and Figure 3.13.b) shows the comparison of peak temperatures between the experimental and simulated results.

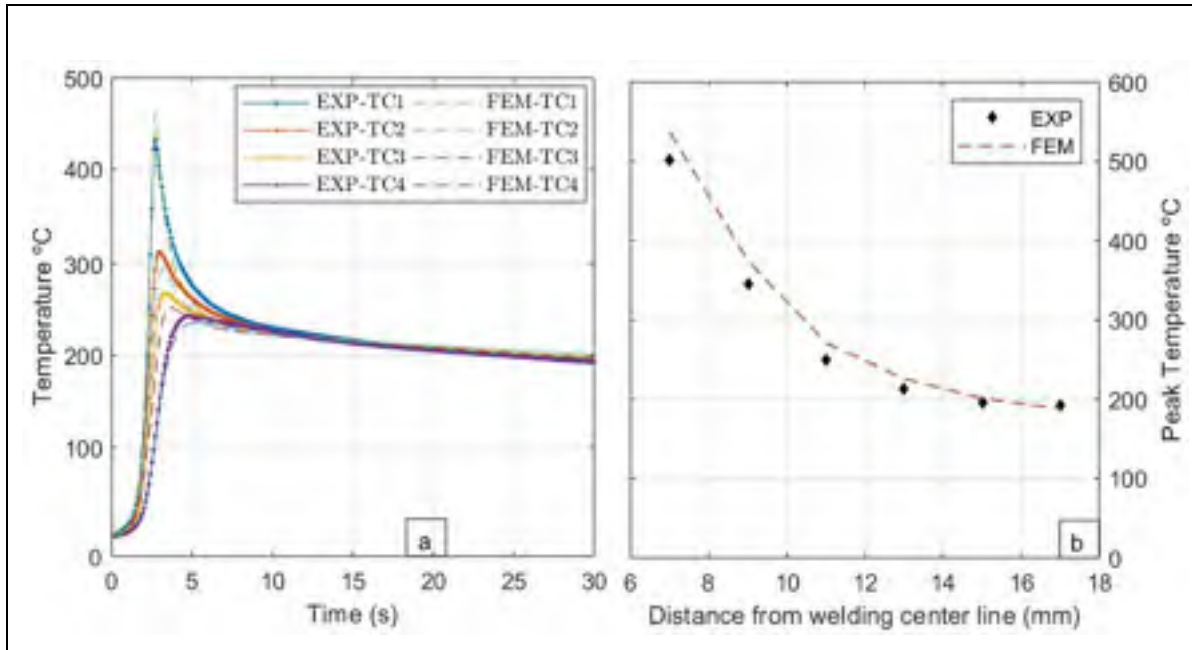


Figure 3.13 Thermal profile of horizontal plate, a) thermal profile comparison between experimental and finite element simulation from points at different distances from the welding center line, b) peak temperature comparison

Table 3.8 Difference in % of peak temperatures in horizontally welded configuration

TCs	Peak Temperature °C			
	TC1	TC2	TC3	TC4
Exp	453	331	276	246
FEA	424	316	267	239.8
Difference in %	6.36	4.5	3.1	2.5

The highest temperature recorded by the thermocouple located at 3mm distance from the boundary of the melting zone and 7mm from the welding center line reached 496 °C, which is less than the solubilization temperature (~520 °C) [50]. The region between the melting zone and up to 10 mm (HAZ) underwent a high temperature gradient (up to 49 °C/mm), and the slope decreases as the distance from welding centerline increases until it reaches 1.26°C/mm.

CHAPTER 4

CHARACTERIZATION OF MICROSTRUCTURE AND MECHANICAL PROPERTIES

This chapter provides a detailed description of the experimental measurements taken before, during and after the welding. These results were classified into two groups; first, a study of the microstructure of the HAZ using visual and optical inspection, and second, characterization of the mechanical properties of the HAZ using microhardness profile and micro-flat tensile tests via digital image correlation (DIC), and third, the influence of welding thermal history on the transformation of the microstructure and mechanical behaviour of HAZ subzones.

4.1 Heat affected zone width

The size of the HAZ is critical to determining the global mechanical behaviour of the welded specimen. The region of the heat affected zone near the FZ can be distinguished by the discolouration of the base metal as illustrated in Figure 4.1. In this study, subzones in the heat affected zone were determined using their microhardness profiles correlated with the welding thermal cycle distribution through the weld cross section, where the peak temperature has risen above 200 °C. The result in Figure 4.2 illustrates the width of the HAZ, which is approximately 12 mm on both sides of the welding center line of horizontally welded with respect to the heat source. The size and shape of the HAZ depend mainly on the welding thermal profile. This characterization shows agreement between the microhardness measurement profile and the welding thermal distribution across various zones of the HAZ as shown in Figure 4.2 and Figure 4.3.

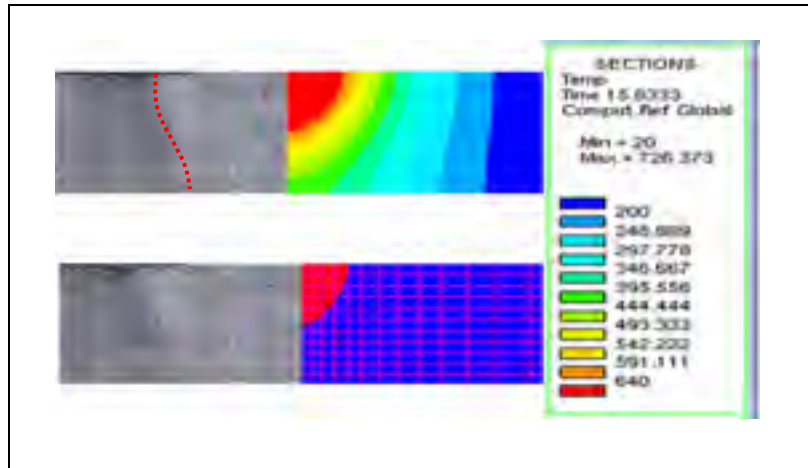


Figure 4.1 Comparison between HAZ of optical image (discolouration) of welding cross section and FE result

Furthermore, micro-tensile tests were performed on the specimen extracted from the welded samples parallel to the welding line and used to characterise the local mechanical behaviour of subzones in the HAZ. This will be discussed in more detail in Section 4.3.1.

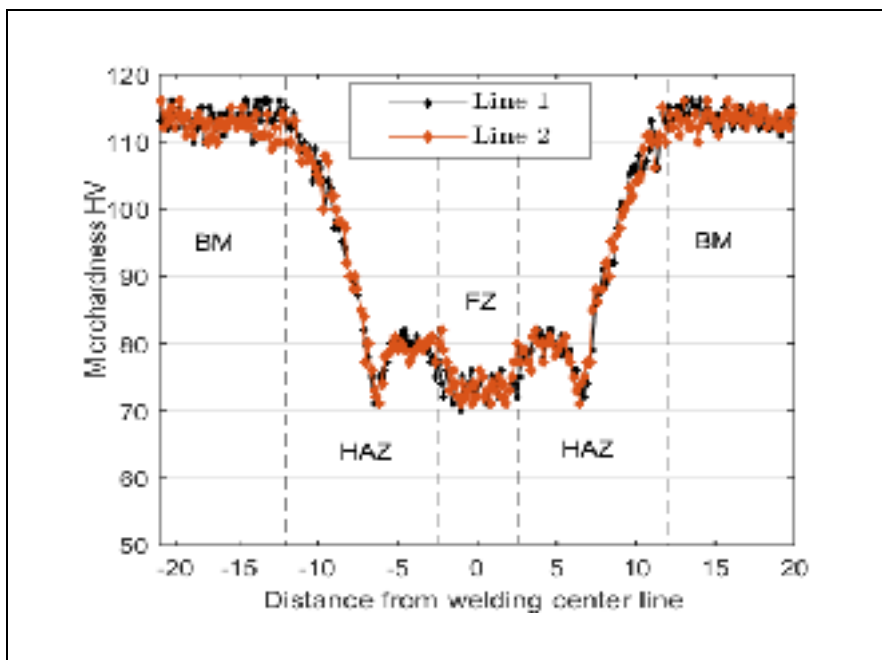


Figure 4.2 HAZ width characterised by microhardness profile on sample cross section in horizontal plate

It is worth noting that the lowest hardness measurement was located between 6 mm to 7 mm from the welding center line in both sides of horizontal plate, and this coincides with the end of the grain growth zone. Based on literature review, grain size contributes slightly to mechanical properties, and this was confirmed in this study. At approximately 6.5 mm from the welding center line, even when the grains have almost the same size as the base metal, it still has the lowest hardness value. This plane (softest zone in the HAZ) will be discussed in more detail in the microstructure analysis section 4.2.

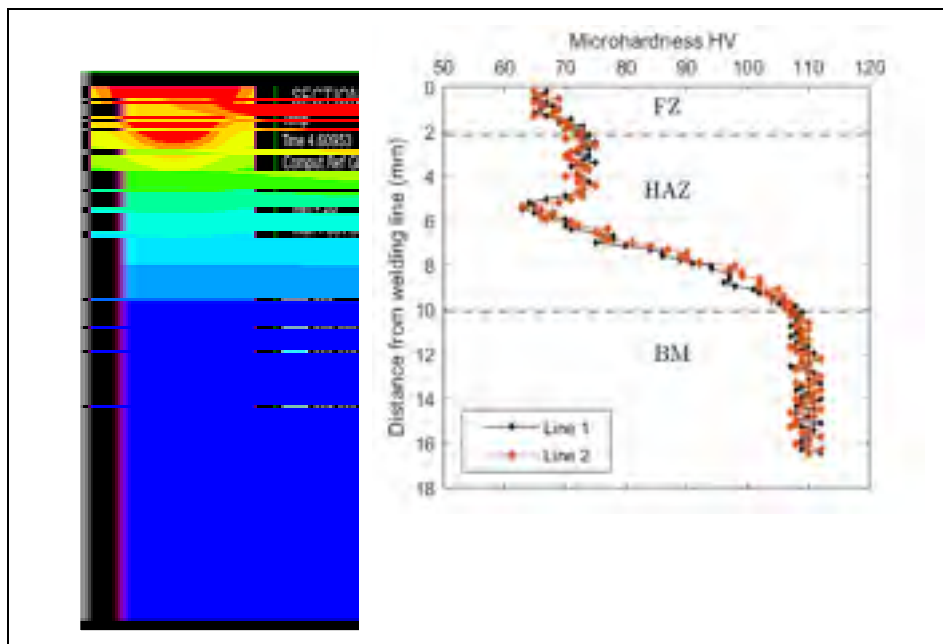


Figure 4.3 Size of HAZ in vertical welded sample

Figure 4.3 (a) and (b) shows the HAZ width in the vertical plate. The thermal and hardness profiles show that the HAZ extended to 10 mm from the specimen's edge. The hardness profile in Figure 4.3 (b) shows that the lowest hardness measurement is located between 5 mm to 6 mm from the specimen's edge. This softest plane was exposed to a peak temperature ranging between 290 °C to 370 °C, which is the critical temperature for phase transformation as mentioned in the literature review [36].

4.2 Microstructure characterization of HAZ

In this investigation light optical photomicrographs were taken with different magnifications to study the initial microstructure variation across different zones such as the FZ, subzones of the HAZ and the BM. This is shown in Figure 4.4 - 4.8. The gradual variation in microstructure from the FZ boundary to the base metal shows that the zones adjacent to the FZ were exposed to various welding thermal cycles.

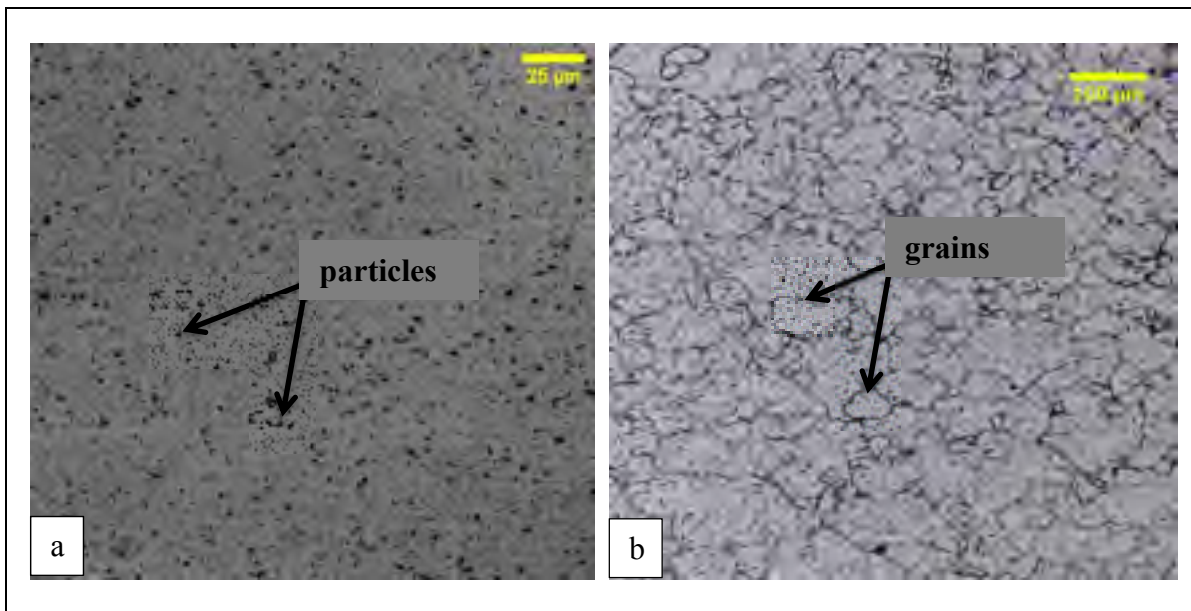


Figure 4.4 Base metal of 6061-T6, a) coarse second phase particles distributed randomly, b) grain size of base metal

The microstructure of the base metal AA6061 in the T6 condition is shown in Figure 4.4. Figure 4.4. (a) which is polished and not etched sample shows nonuniform distribution of intermetallic particles through the microstructure of the base metal. The etched sample in Figure 4.4 (b) mainly shows the grains of the base metal and the grain boundaries which appear as a thick, dark, etched layer. The base metal has a mean equiaxed grain size of 43 μm.

Normally, weldment solidifies through epitaxial solidification in the FZ. Epitaxial solidification in the FZ begins with the deposition of crystals from the weld pool on incompletely melted grains in the PMZ, and nucleation is not essential in order to complement the solidification. Figure 4.5 (b) shows that the low melting phases segregated on the grain boundary and large grains adjacent to the FZ grow to complete the epitaxial solidification.

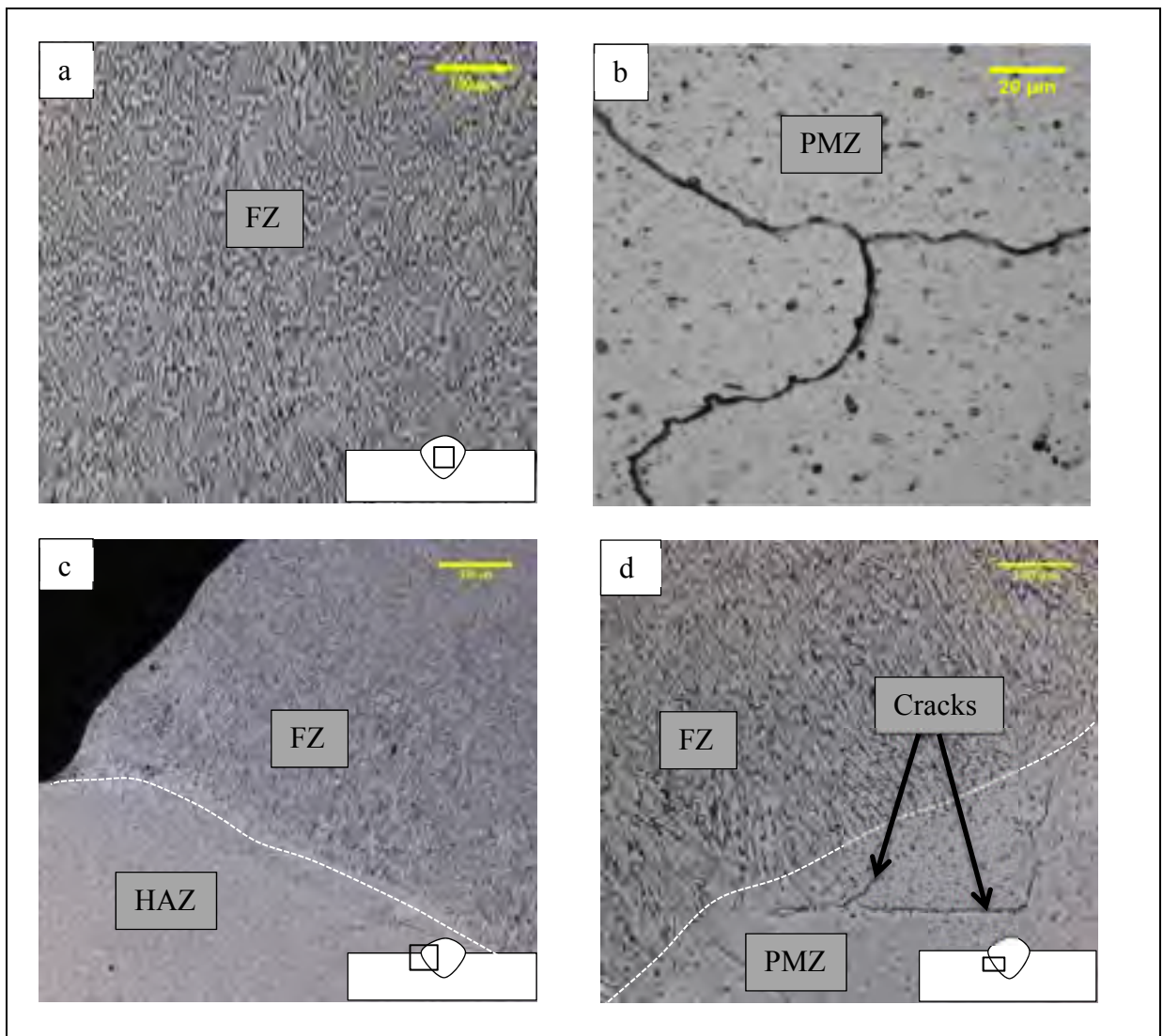


Figure 4.5 Light optical micrographs of microstructure of FZ and PMZ; a) grains in FZ, b) low melting phases segregated on the grain boundary, c) The interface between the HAZ and fusion zone showing fine microscopic hot cracks, d) high magnification of figure (c)

The as welded condition of AA6061-T6 shows a well-defined grain boundary at the fusion zone (FZ) as in Figure 4.5 (a). There is a clear difference in microstructure between the FZ and the HAZ. The FZ consists of small grains of varying shape that range from 10 μm to 20 μm . Figure 4.5 (d) shows columnar grains. Meanwhile; the centre of the welded metal was solidified into equiaxed grains with the presence of small sized porosities.

A fine microscopic liquation crack was observed in 6061-T6 welded with AA4043 filler metal. Figure 4.5 (c) reveals that the crack began at the interface of the FZ and PMZ, and propagated into the HAZ. The difference in density between the solid and liquid aluminum caused the weld pool to contract and pull on the solidifying adjacent material in the partially melted zone during solidification, and the tension caused cracks in the PMZ.

4.2.1 Grain growth in HAZ

Grain growth in aluminum reduces the mechanical properties, for example tensile strength, especially in non-heat treatable alloys. However, grain growth also has a slight effect on the mechanical properties of heat treatable alloys because these alloys derive strength from precipitation hardening [51, 52]. Areas adjacent to the fusion zone boundary would be exposed to high temperatures for a longer time, which provides enough time to produce the largest grain size in the HAZ as shown Figure 4.7 (a). In this investigation, the linear intercept technique was applied to determine the average grain size in the HAZ.

The elevated temperature generated by the welding thermal cycle in the area adjacent to the FZ helps to release the grain surface energy by grain growth and results in large, equiaxed grains along the fusion boundary. Figure 4.6 shows the average grain size measured across the HAZ as a function of the distance from the welding centre line. The average grain size increased gradually from 43 μm in the zone 6 mm from the FZ boundary to 310 μm at the FZ boundary. In the zone adjacent to the FZ, which was exposed to the highest thermal cycle, the grain size was six times that of the base metal grain size.

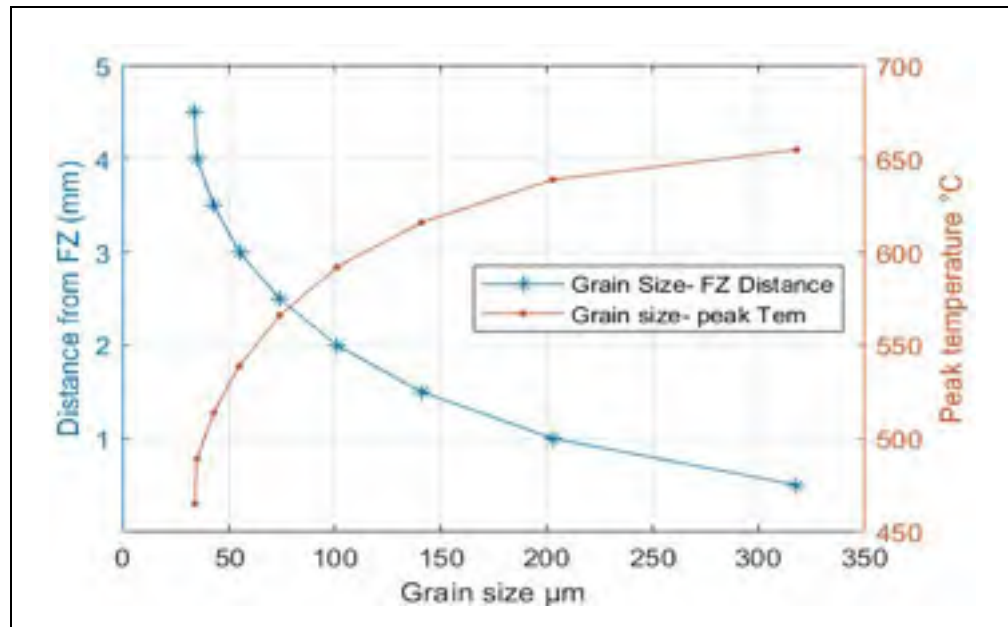


Figure 4.6 The relationship between average of grain growth and peak temperature across the HAZ

Figure 4.6 shows the relationship between the peak temperature and the average of the grain coarsening effect. The area adjacent to the FZ with an average peak temperature of 610 °C has the coarsest grains. This zone has an average grain size of 318 μm. Grain size decreased steeply in the HAZ until the grain size has the same grain size as the base metal at a distance of 6.5 mm from the welding center line. It can be noted that the grain coarsening takes place at the first 3.5mm of the HAZ starting from the FZ boundary. This zone where grain growth occurs has a variation in hardness value that ranges from 77 HV to 83 HV. No clear relationship was found between the variation of hardness value and grain size. It is worth noting that no observed coarsening occurred where peak temperature remained below 450 °C.

Figure 4.7 shows grains in the zone adjacent to the FZ where the grains have an average size of 318 μm and the size decreases gradually as a function of distance from the welding line. Figure 4.7 (b) was taken beneath the fusion zone as is illustrated in the schematic drawing. Grain growth has a proportional relationship to the thermal cycle with respect to time. However, grain growth has a lesser effect on mechanical properties than precipitation

transformation, and this can be shown by comparing grain size with lowest hardness in the HAZ, which will be discussed in more detail in the next section.

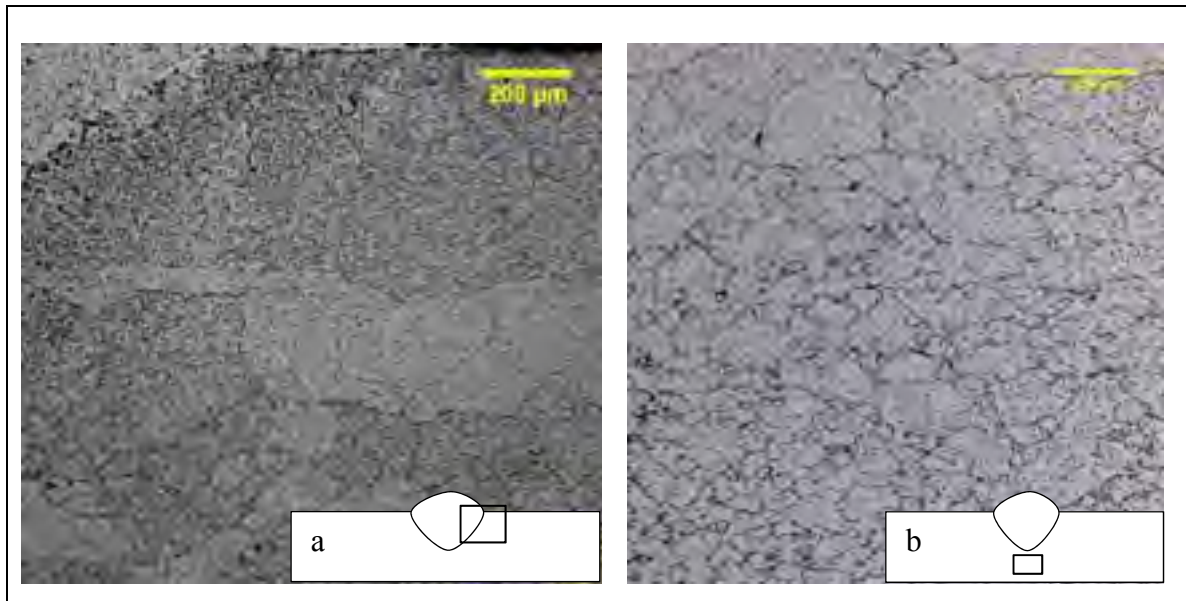


Figure 4.7 Light optical micrographs of recrystallization and grain growth; a) zone adjacent to FZ, b) gradual change of grain size

4.3 Mechanical characterization of HAZ in vertically welded plate

Mechanical properties of a welded plate vary significantly across the HAZ and correspond to the microstructure that is produced by the welding thermal profile. The aim in this section is to characterise the mechanical properties of subzones across the HAZ. The microhardness tests were conducted four weeks after the welding to minimise the natural aging effect. The most hardness recovery occurred in the first and second weeks with a recovery rate of 2.3% per day, and in the fourth week, the hardness recovery rate was 0.4% per day as reported by V. Malin [27].

4.3.1 Microhardness behaviour across the HAZ

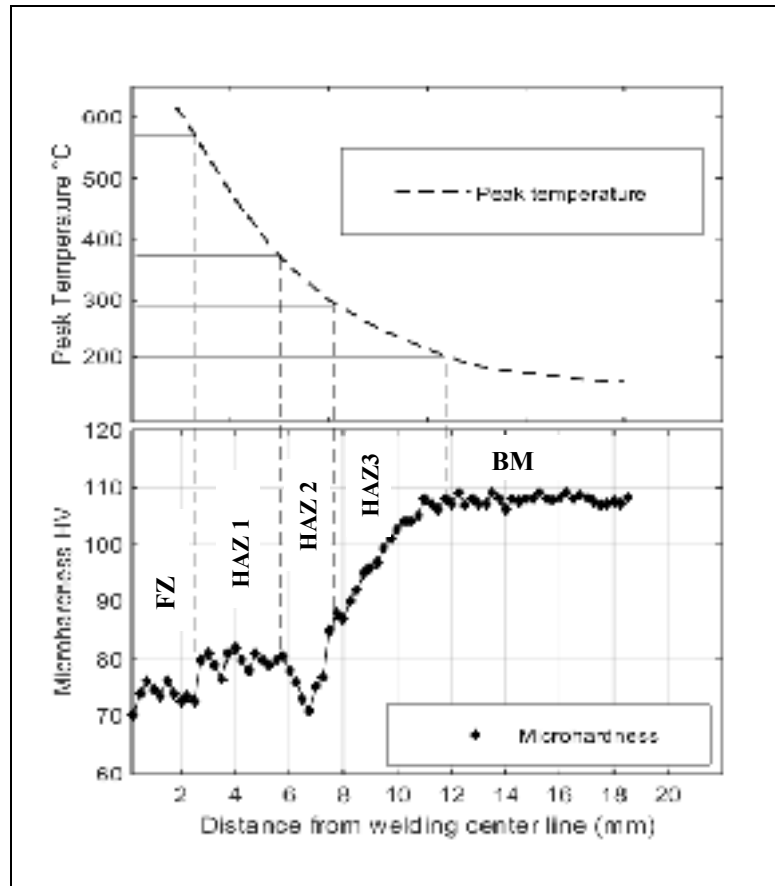


Figure 4.8 Correlation between thermal cycle and microhardness values in HAZ

Figure 4.8 illustrates the T_{MAX} profile with microhardness results placed over each other. Studying the relationship between the T_{MAX} and hardness shows that the FZ, which was exposed to T_{MAX} over 580°C has a low average hardness value of 73 HV. The low hardness value could be attributed to the lack of precipitates, the change in chemical composition and the porosity that is present in this zone.

As observed in Figure 4.8 the zone adjacent to the FZ (HAZ 1) was subjected to peak temperature between 380°C to 580°C . This zone has an average hardness value of 80 HV. In this zone, the precipitates of β'' dissolved or transformed to β' (with respect to the distance

from the welding center line) and the material became a combination of $\alpha+\beta'$ phases. The hardness increases to 80 HV after four weeks in this zone due to naturally aging of β'' precipitate. The plane which separates HAZ1 and HAZ3 was subjected to a critical temperature and had the highest β' phase fraction because the critical temperature caused needle shaped fine precipitates of β'' to dissolve and the biggest one started to grow and form a rod shape β' [17, 32, 53]. This plane had the lowest hardness value of 70 HV. HAZ3 where the temperature below 290°C the hardness increased until it reaches the hardness of base metal where the peak temperature remain less than 200 °C. It was not affected by the welding thermal cycle.

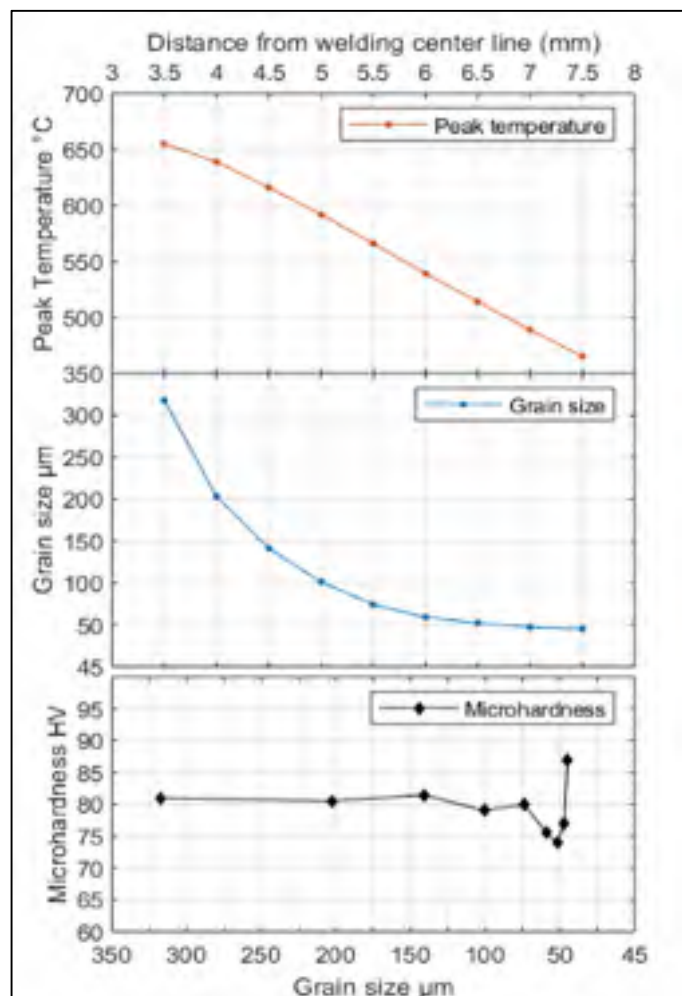


Figure 4.9 Correlation between grain size, microhardness, and peak temperature across the HAZ

Figure 4.9 shows the relationship between grain coarsening and microhardness. Although the grain size in the closest zone to the FL was an average size of six times bigger than the base metal and steeply decreases as the distance from the FL increases, the observation of hardness that resulted across these zones shows almost steady hardness values. The lowest hardness value located at a distance of 3.5 mm from the FL (6.5 mm from welding center line) and the average grain size at this zone of 55 μm is almost equal to the grain size of the base metal. From these observations it can be noted that there is no important effect of grain growth on mechanical behaviour at the over-aged zone where grain size is equal or less than 320 μm .

4.3.2 MFT parallel to the welding line

Figure 4.10 illustrates the cutting arrangement for the machined sample parallel to the welding line. As showed in Table 4.1, each specimen had a different thermal cycle; moreover, microhardness values across the thickness of the MFT sample and across the gauge length for each sample were used to characterise each MFT specimen. The result shows that the softest zone in the HAZ is located at 3.5 mm to 5 mm from the welding center line.

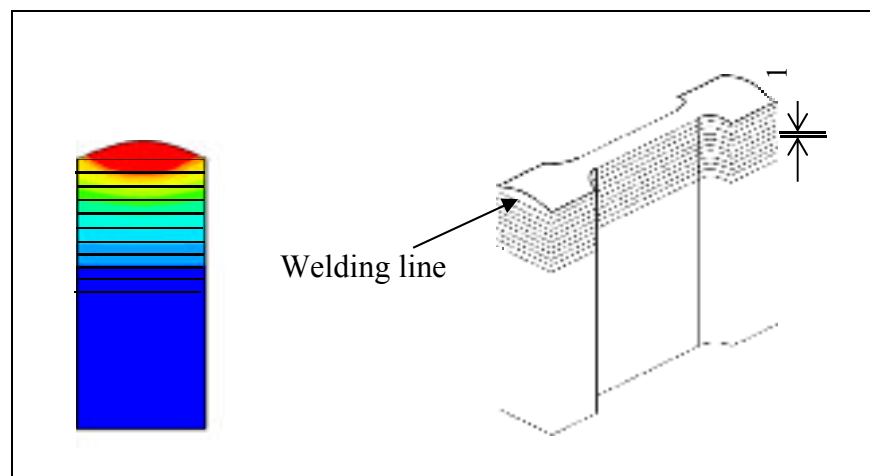


Figure 4.10 Cutting arrangement for the machined sample

Test 1 and Test 2 are the specimen that extracted parallel to the welding line from the vertical plate, and samples in the both tests have the same welding and testing procedure. Figure 4.11 shows the location of microhardness measurement cross the gage length of MFT test.

Sample 1

Table 4.1 Shows microhardness and peak temperature with the MFT result for each specimen parallel to weld

Specimen No	Distance from FL (mm)	Peak Temperature (°C)	Average of Hardness Cross A	Average of Hardness Cross B	Tensile Test		
					UTS MPa	YS MPa	Elongation %
01	FZ	820-640 (FZ)	67	68	---	---	---
02	0-1	625-538	72.5	73	274	208	13.6
03	1.5-2.5	508-442	73	74	263	173	15.2
04	3-4	410-358	74	73	260	146	22
05	4.5-5.5	340-296	68.5	74	249	147	21.5
06	6-7	286-258	75	74	265	232	8.7
07	7.5-8.5	245-220	90.5	92.5	292	260	8.3
08	9-10	210-180	103	101	296	269	7.4
09	BM	BM	110	112	304	269	7.2
10	BM	BM	108	110	309	271	6.9

NOTE: A: is across the thickness of the MFT sample, B: is across the gage length of the MFT sample

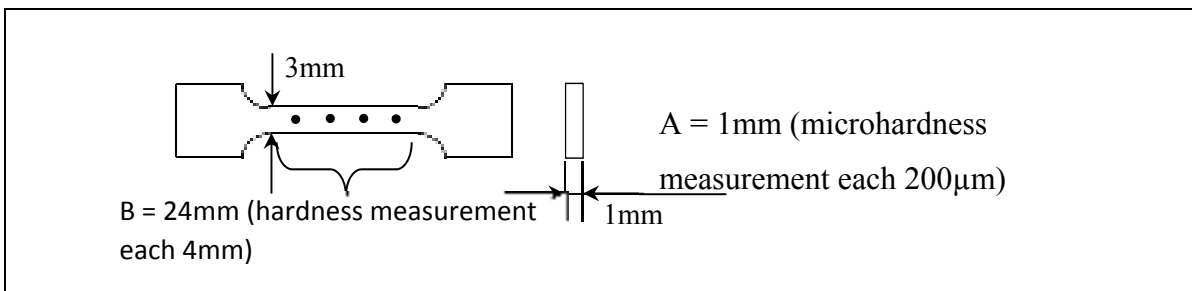


Figure 4.11 Microhardness measurement locations in the MFT samples

Sample 2

Table 4.2 Shows microhardness and peak temperature with the MFT result of each specimen parallel to weld

Spaciemen No	Distance from FL (mm)	Peak Temperature (°C)	Average of Hardness Cross A	Average of Hardness Cross B	Tensile Test		
					UTS MPa	YS MPa	Elongation %
01	FZ	820-640 (FZ)	68	69	---	---	---
02	0.5-1.5	625-538	73	74	267	202	13.2
03	2-3	508-442	73.5	74.5	273	167	13.8
04	3.5-4.5	410-358	74.5	74	263	151	19
05	5-6	340-296	69	68	252	157	20.1
06	6.5 -7.5	286-258	73.5	75	258	253	9.6
07	8-9	245-220	88.5	90.5	285	267	7.3
08	9.5-10.5	210-180	99.5	102	292	273	8.3
09	BM	BM	110	112	307	268	8.1
10	BM	BM	108	110	314	274	7.4

The subzone that extends from the FZ boundary to 3.5 mm and was exposed to a peak temperature between 625 °C and 442 °C shows a 15% decrease of UTS and a 30% decrease in YS. Meanwhile, the elongation increased 47% compared to the BM. The overaged zone which extended from 4 to 6 mm with peak temperature between 410 °C and 296 °C shows the least favourable mechanical properties. The UTS in this zone decreased 20%, and the YS decreased 45%. As a result of over aging the, elongation increased 230% compared to the base metal. Beyond the end of the over aged zone at 6.5mm from the welding center line, the mechanical properties start to improve intensely, until the mechanical properties match those of the BM at 10 mm.

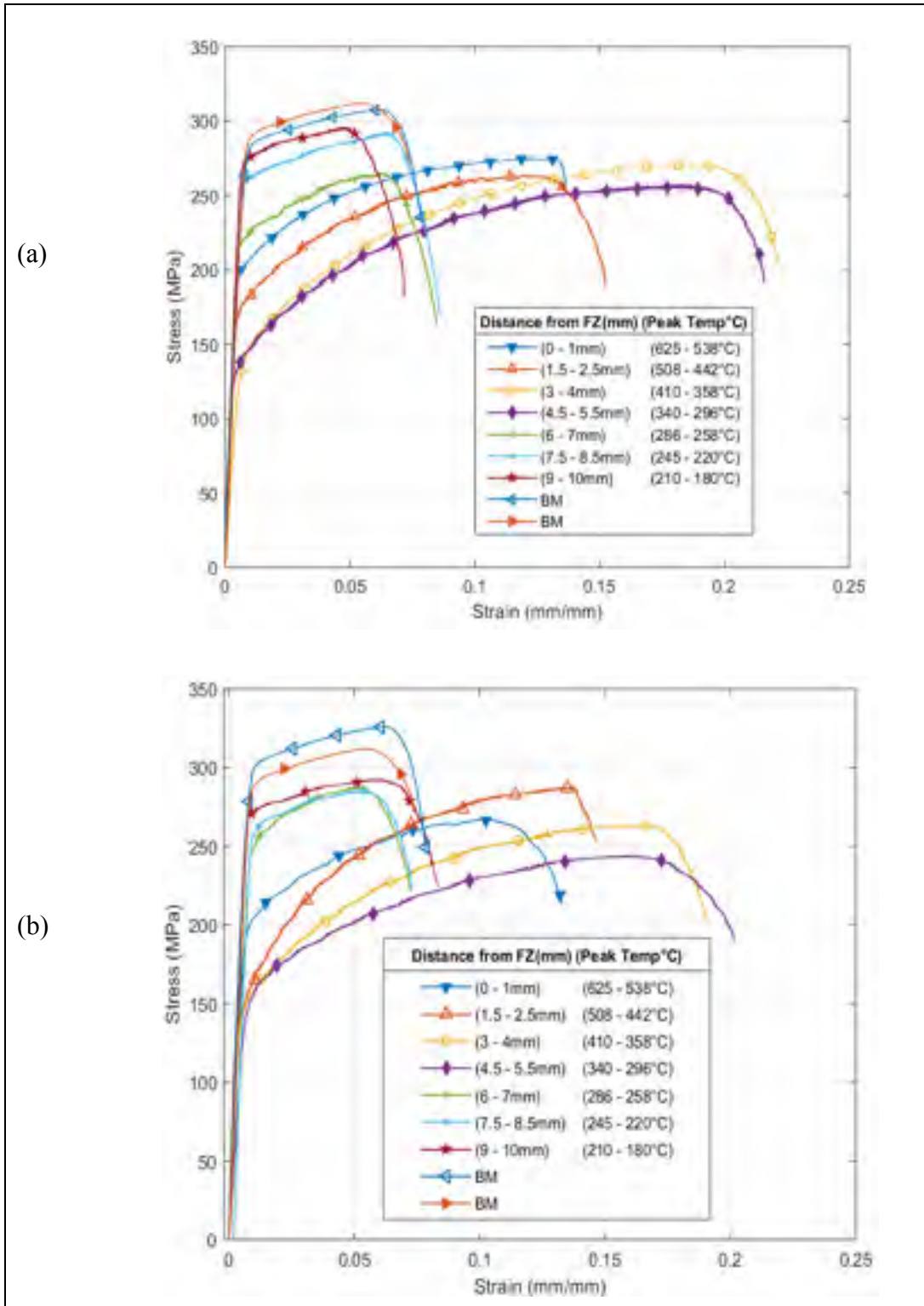


Figure 4.12 Stress- strain for different specimen extracted from different HAZ, a) Test 1, b) Test 2

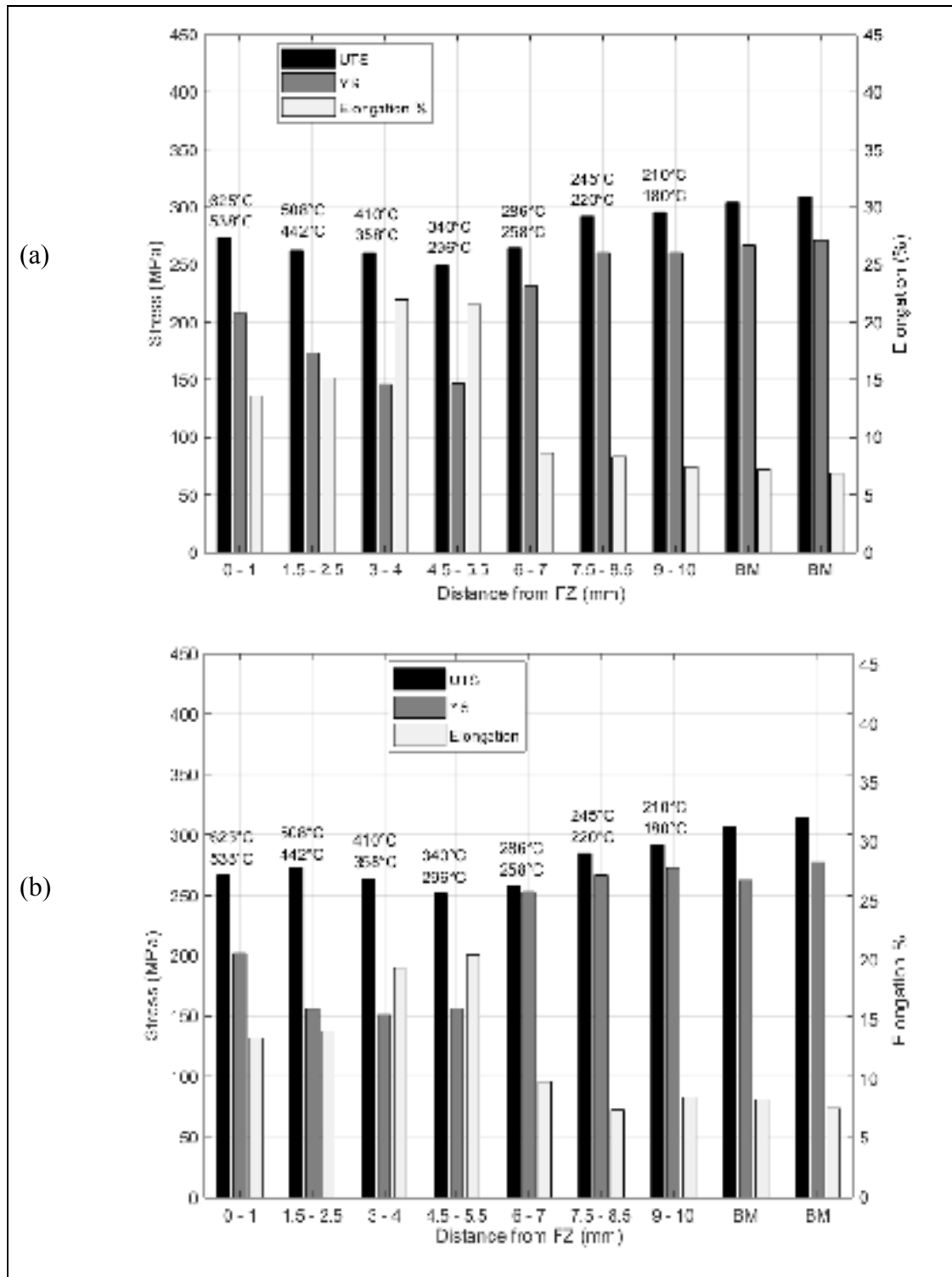


Figure 4.13 Tensile properties in different zones, a) Test 1, b) Test 2

4.3.3 Micro-flat tensile test (DIC)

A comparison of the experimental results of the stress-strain tests for global response of the base metal and welded samples is illustrated in Figure 4.14, and the mechanical behaviour of the base metal and welded specimens are shown in Table 4.3.

Table 4.3 Properties of base metal and welded specimens

Description	Welded sample			Base metal		
	Test 1	Test 2	Ave	Test1	Test2	Ave
(a) Yield Stress (MPa)	153	162	157.3	271	271	274
(σ max) Ultimate strength (MPa)	220	231	226	301	308	305
Elongation (%)	6.8	6.7	6.8	9.1	9.8	9.4

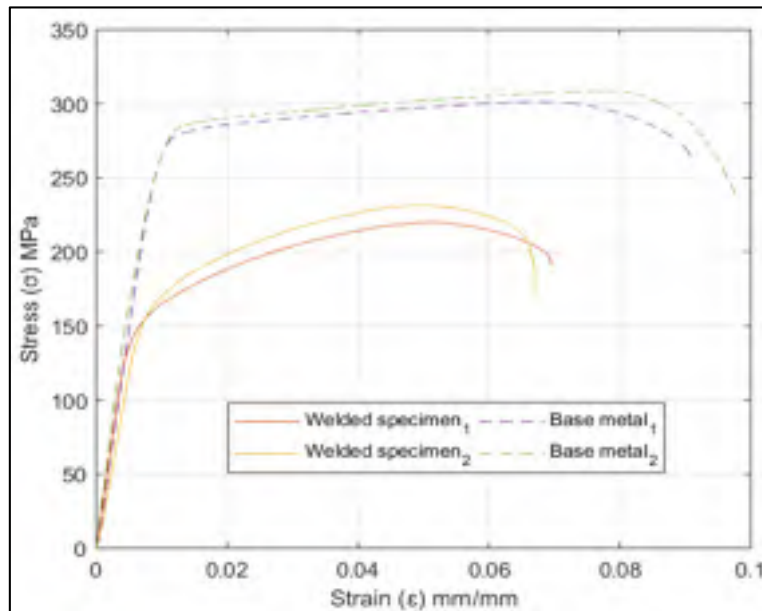


Figure 4.14 Global response (stress-strain) curves for welded sample and parent metal

An offset of 0.2 % yield strength (YS) of 157 MPa and an ultimate tensile strength (UTS) of (226 MPa at 4.4 %) plastic strain was found in the welded samples. The stress gradually

decreased as strain exceeded the UTS, and as a result of substantial necking at approximately 6.5 mm from the welding line, the samples finally fractured at 6.8% strain.

4.3.3.1 Local behaviour of welded specimen from MFT test with DIC

The two samples depicted in Figure 4.15 represent the deformation in X and Y directions measured with DIC. The results of the two tests are coherent and show that the local in-plane strain obtained from DIC can be utilised.

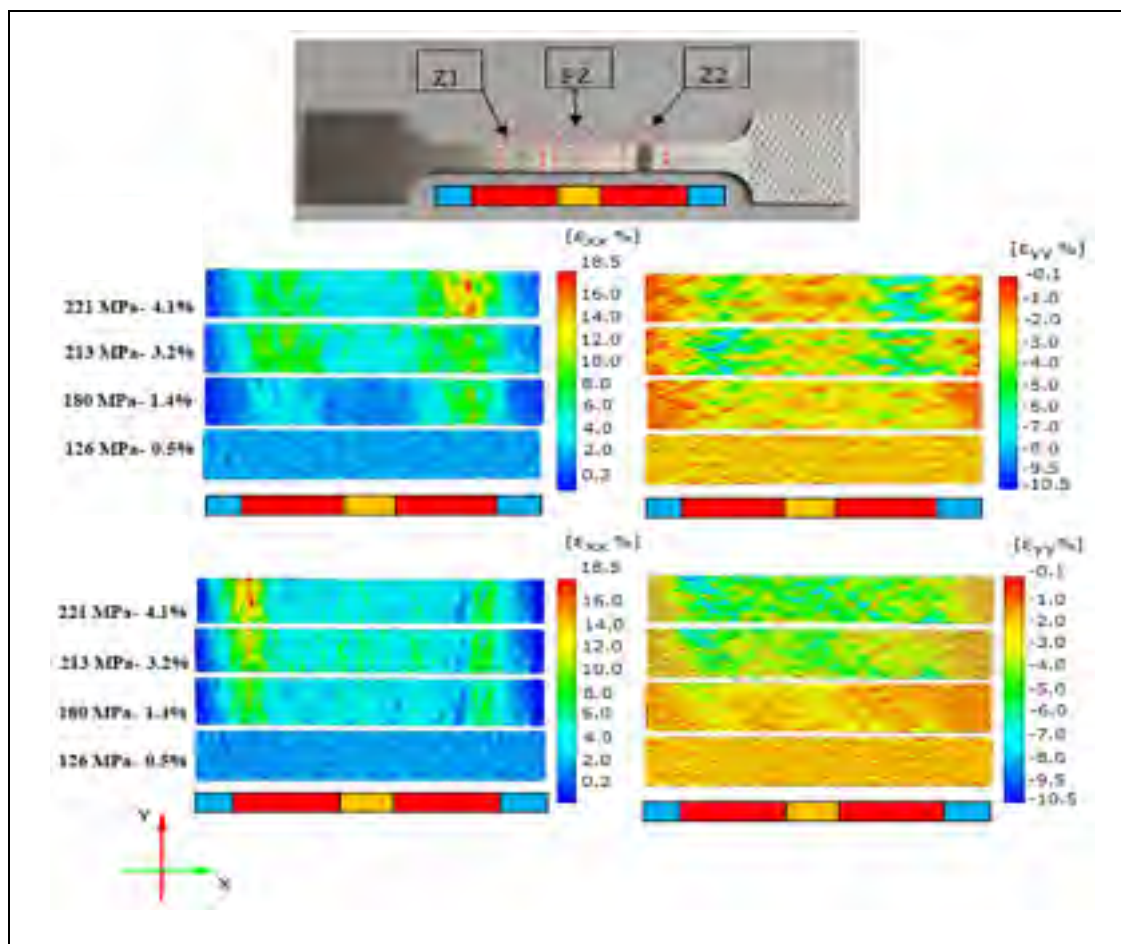


Figure 4.15 Illustration of distribution of local in-plane strain acquired using DIC equivalent to different strains (corresponding to 24 mm specimen gauge length) for two specimens

Strain measurements along the longitudinal direction of the specimens were captured at four stages (in elastic and plastic) of loading by DIC and the results for the two specimens were illustrated in Figure 4.15. The stages correspond to the principal stress and the mean value of strain. It is noted that strain was initially distributed evenly across the gauge length (FZ and HAZ) until the stress reached 126 MPa as shown in Figure 4.15.

At stage one, at a stress value of 180 MPa the strain starts to concentrate at approximately 6.5 mm from the welding line on both sides of the weld as shown in Figure 4.15. At stage two, increasing in stress value up to 213 MPa leads to strain concentration in these two planes (Z1 and Z2) as shown in Figure 4.15. And at stage three, when the stress value approaches the UTS value (221 MPa), the necking begins to occur at one of the two planes before the fracture.

The three stages depicted in Figure 4.16 represent the mean value of the local strains measured with DIC. The ϵ_{XX} and ϵ_{YY} strain fields correspond to the X and Y axes which are the cross welding direction and welding direction respectively. The average values of ϵ_{XX} and ϵ_{YY} for the regions of interest on both sides of the weld center line were plotted as a function of cross weld direction in Figure 4.16 for different strain levels. The overall deformation was not distributed evenly and showed different behaviours across the FZ, HAZ and BM.

At the first stage of deformation (126 MPa – 0.5%), the ϵ_{XX} strain fields exhibit equal strain distribution across the softened zone (FZ and HAZ, 9.5 mm from the welding center line on both sides), and above the BM. At this stage, the variation of local strain is only 0.25 % between the soft zone and BM. Increasing the load value (180 MPa – 1.4 %) shows concentration in strain being found in the plane 6.5 mm from the welding line on both sides of the welding center line. The strain value reaches an average of 8.5% at the high deformation plane (softest plane across the HAZ) compared to 2.5 % in the FZ and 0.35 % in the BM as shown in Figure 4.16 b).

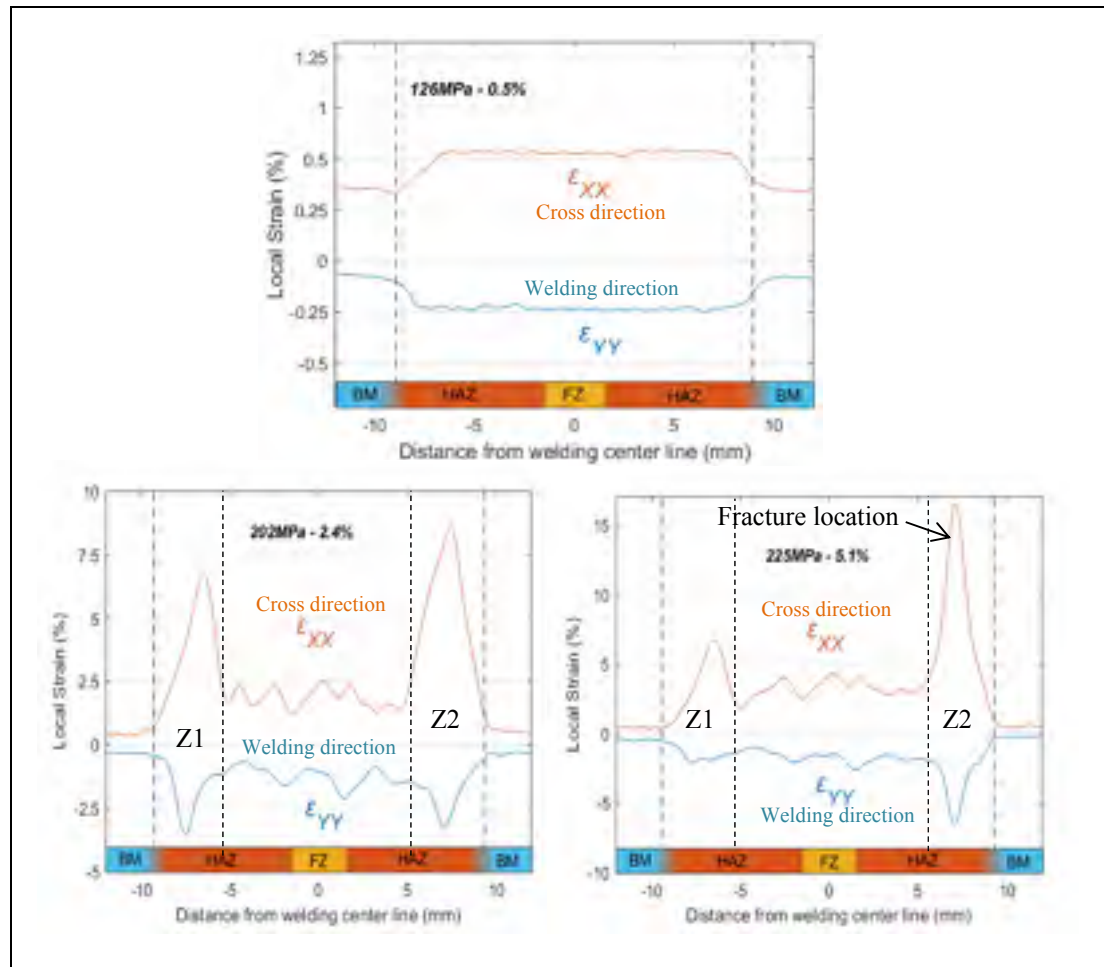


Figure 4.16 Average value of ϵ_{XX} and ϵ_{YY} in transverse weld direction for three stages of stress/strain condition. a) 126 MPa_0.5%, b) 202 MPa_2.4% and, c) 225 MPa_5.1% illustrating local in plane strain localisation zones

In the stage before necking (225 MPa – 5.1 %), the local deformation is mainly localised in one of the high deformation planes (Z1 and Z2) 6.5 mm from the welding center line, until the strain reaches 16 % compared with another plane which reaches 7 %, or approximately 40 % of the other zone. The mean strain value of the FZ and HAZ, excluding the softest plane, was around 5 %, which is 30 % of that found in the highly deformed plane. The local strain increases in this plane until the fracture occurs as shown in Figure 4.16 c). Interestingly, the ϵ_{XX} response remains in proximity even along the soft zone, with respect to each stage, except for the high deformation plane which suffers high deformation during the necking stage.

4.3.3.2 Local behaviour of HAZ

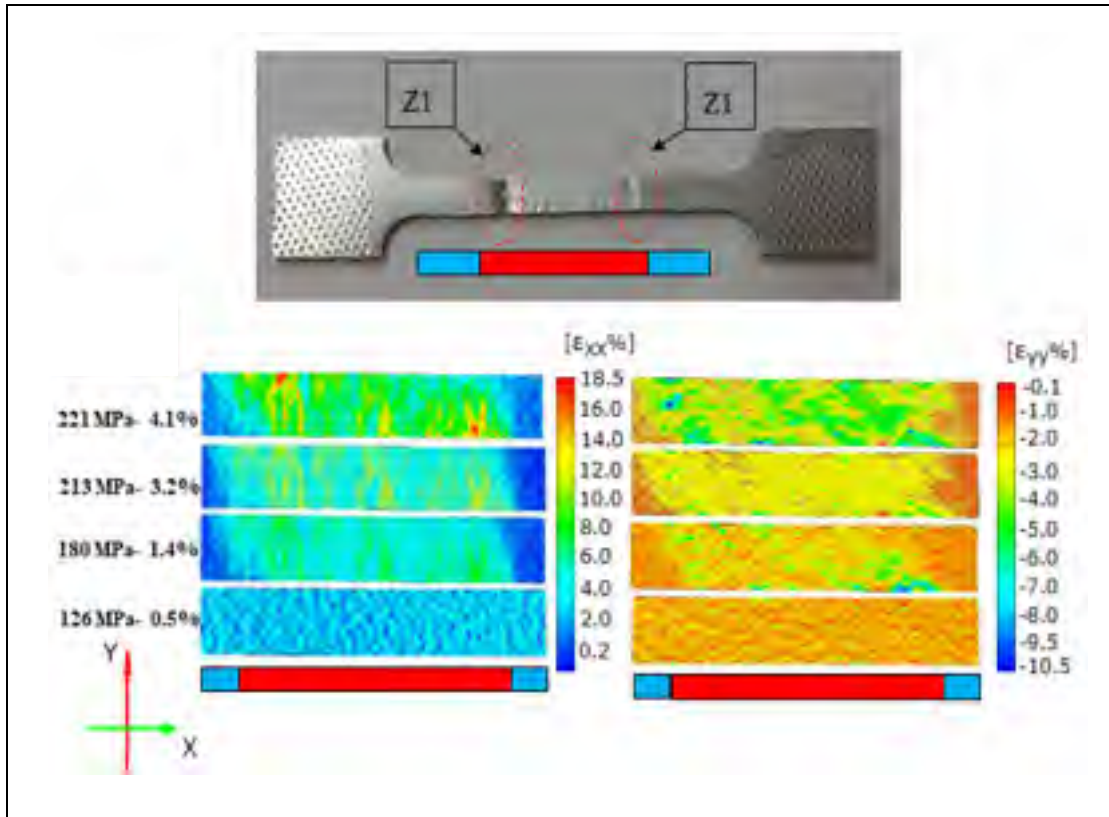


Figure 4.17 Illustration of distribution of local in-plane strain acquired using DIC equivalent to different strains (corresponding to 24 mm specimen gauge length) in the HAZ

Figure 4.17 shows the local strain distribution in the HAZ. It is noted that strain in stage one was distributed evenly across the gauge length until the stress reaches 126 MPa as shown in Figure 4.17. At stress value of 180 MPa, the strain starts to concentrate at the HAZ more than the BM. It is worth noting that the local strain continues to distribute almost evenly across the HAZ until 213 MPa compared with Test-1 and Test-2. At stage four, when the stress value reaches 221 MPa, the local strain starts to concentrate at approximately 6 mm from the weld line on both sides of the weld as shown in stage four in Figure 4.17. The concentration of strain in these two planes (Z1 and Z2) which is presented in Figure 4.17 leads to the fracture in one of these planes.

The three stages illustrated in Figure 4.18 represent the average values of ϵ_{XX} and ϵ_{YY} for a region of interest on both sides of the weld center line, and were plotted as a function of cross weld direction as in Figure 4.18 for different strain values. The overall deformation was not distributed evenly and showed different behaviour across the HAZ.

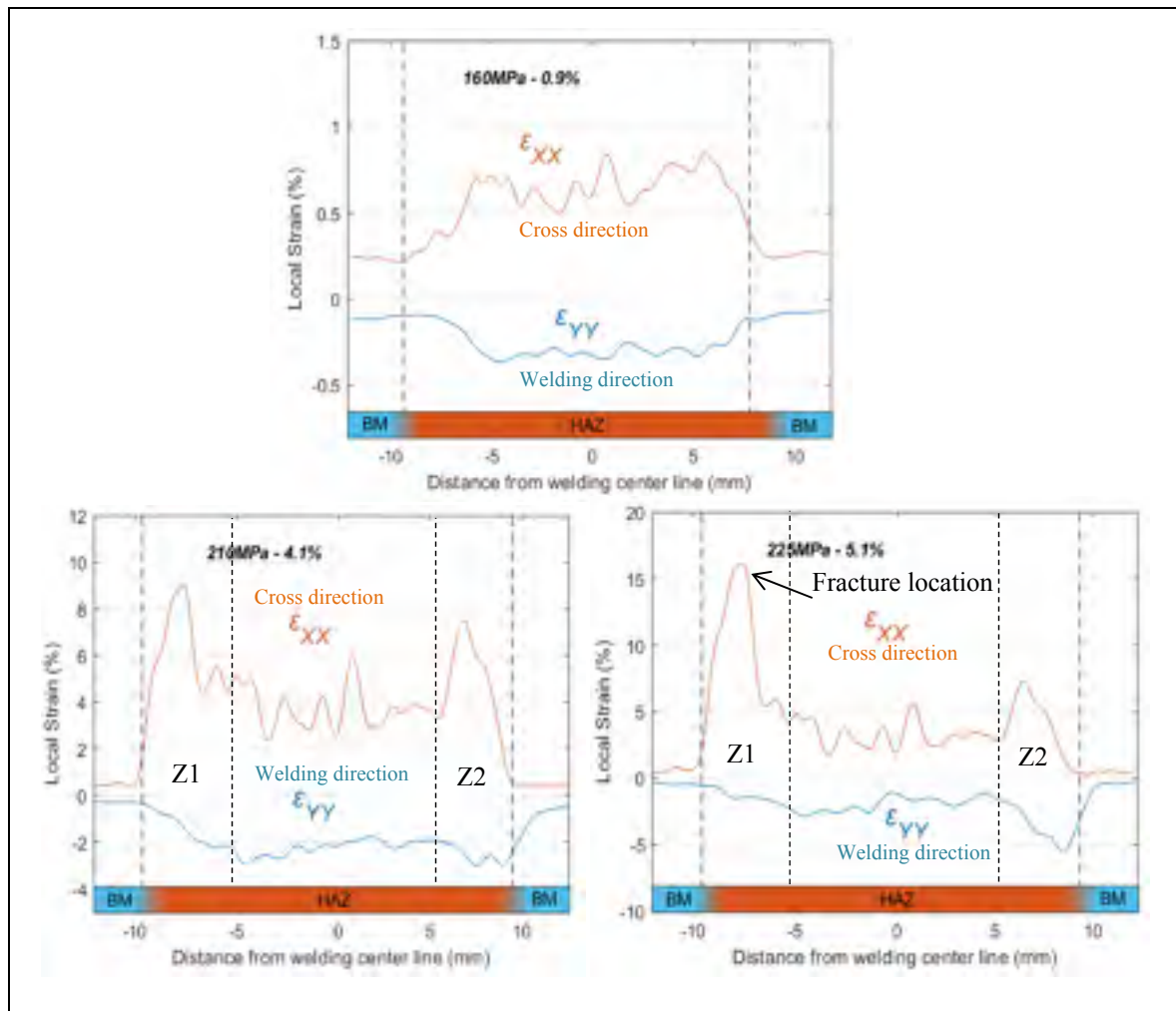


Figure 4.18 Average value of ϵ_{XX} and ϵ_{YY} in transverse weld direction for three stages of stress/strain condition. a) 160MPa-0.9%, b) 210 MPa-4.1% and c) 225 MPa-5.1% showing local in plane strain concentration zones

At the first stage of deformation (160 MPa - 0.9%) the ϵ_{XX} strain fields exhibit equal strain distribution across the HAZ, which is higher than that of the BM. At this stage, the variation

of local strain is only 0.35 % between the soft zone and BM. Increasing the load (210 MPa - 4.1 %) shows the subzones in the HAZ suffer high local deformation compared with Test1&2 where the local deformation starts to concentrate at an early stage (180 MPa - 1.4 %) at over-aged planes (Z1 & Z2).

In the stage before necking (225 MPa – 5.1%), the local deformation is mainly localised in one of the high deformation planes (Z1 and Z2) 6 mm from the welding center line until the strain reaches 15 % compared with another plane which reaches 7.5 %. The mean strain value in the HAZ, excluding the softest planes (Z1&Z2), was around 6 %. The local strain increases in the over-aged plane until the fracture occurs as shown in Figure 4.18.

4.3.4 Local behaviour of HAZ subzones in welded plate obtained by DIC

Figure 4.19 shows the location of local strain investigated in different zones: the fusion zone, HAZ, and base metal. Figure 4.19 shows local strain-time curves for the welded specimen. Different zones with different behaviour can be distinguished clearly in figure 4.19. From this depiction, it is possible to consider three stages. Stage one up to 50 s: at this stage all zones along the gauge length have the same behaviour (elastic). Stage two between 50 s and 400 s: at this stage, zones in the HAZ experience plastic deformation, whereas strain in Z8 (BM) remain approximately constant (in elastic region). Stage three between 400s and 520s: in this stage, the strain is localised in the softest zone (Z4 and Z5) where the fracture will occur; meanwhile the behaviours of other HAZ zones, FZ and BM remain almost the same.

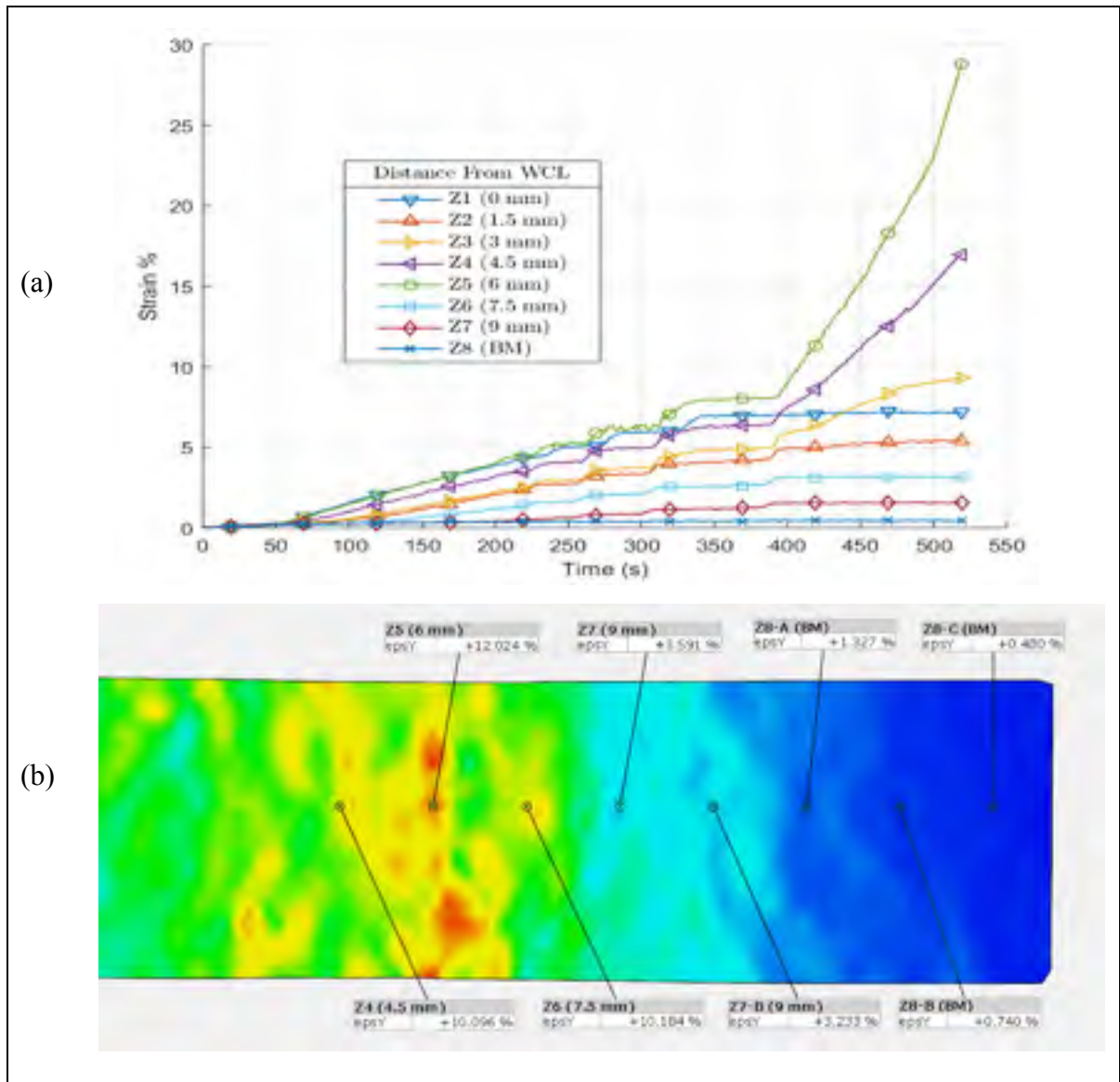


Figure 4.19 a) Local strain-time for different locations on the welded sample, b) shows the location of local strain investigated (BM & HAZ & FZ)

4.3.5 Local Stress–Strain properties obtained using DIC test in welded sample

Assuming uniform stress, every local position in the gauge length undergoes the same stress at any applied load.

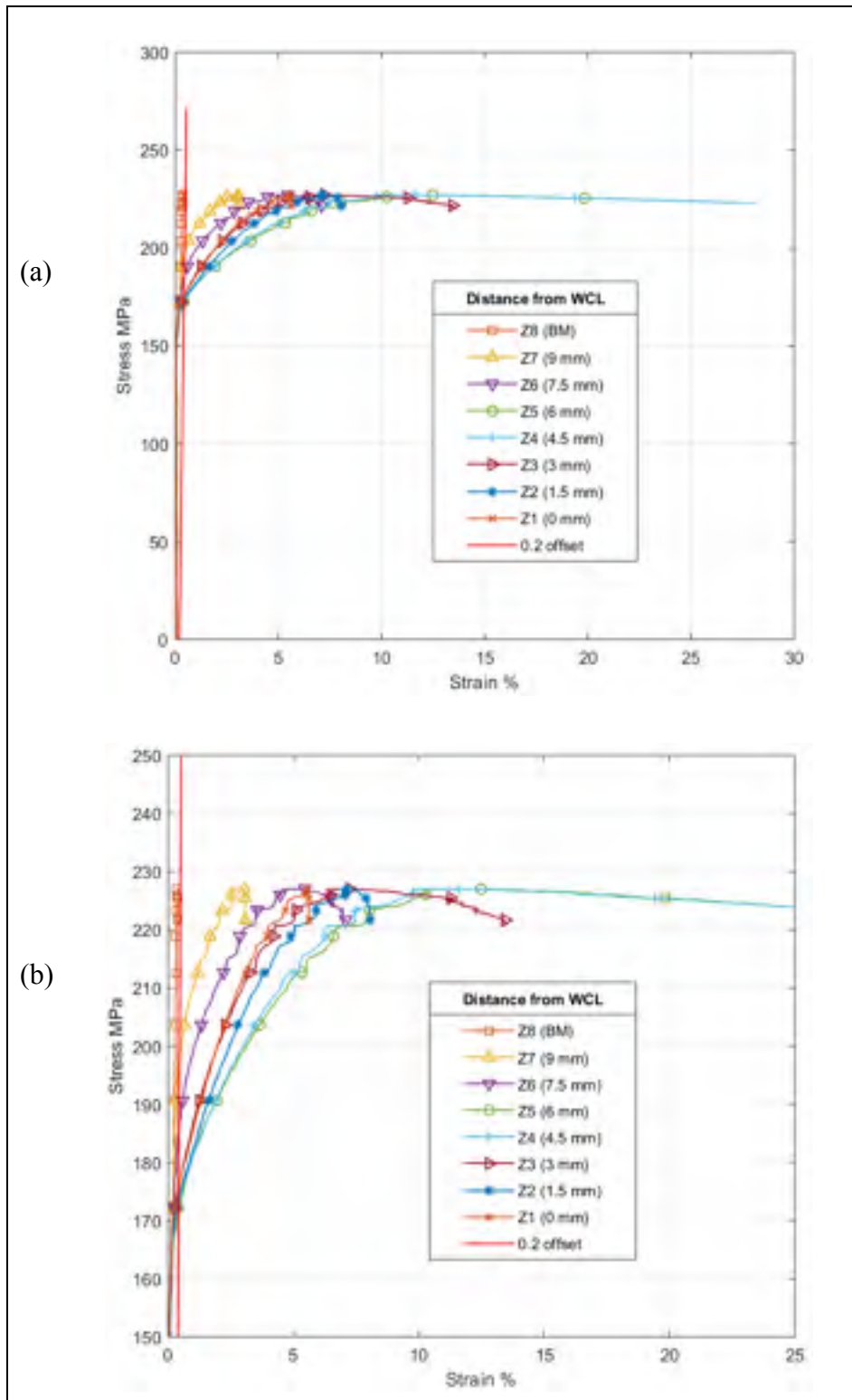


Figure 4.20 is a plot of uniform DIC stress-local strain measurements for eight zones (Z) along the gauge length as illustrated in Figure 4.20. Z4 and Z5 underwent softening behaviour and have the highest strain value and lowest yield strength. The zones Z1, Z2 and Z3 shows similar behaviour to the lower strain level compared with Z4 and Z5. Zones close to BM (Z6 and Z7) show higher yield strength and lower deformation. It is clear that Z8 (the base metal) is still in the elastic region.

The global mechanical response of over aged zones in terms of longitudinal stress-strain of the samples is plotted in Figure 4.21. The two softest planes in the HAZ (Z1 and Z2), welded and parent metal are illustrated in the same figure. The Z1 plane shows the highest localised deformation where the fracture finally occurs. Localisation of strain up to 18 % was observed in the Z2 region as shown in the figure.

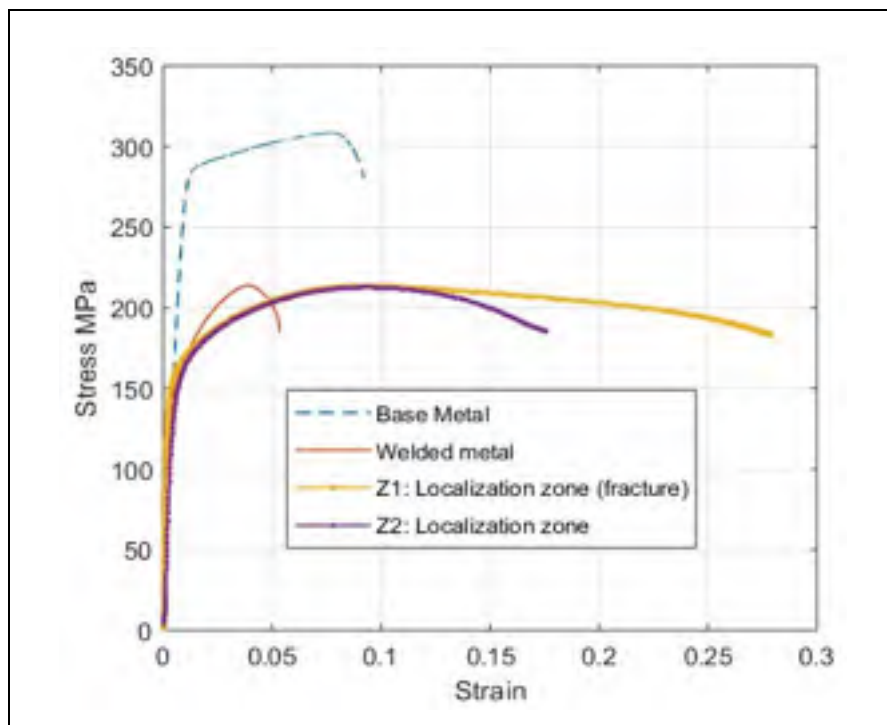


Figure 4.21 Average stress-strain behaviour (DIC measurements) for welded joint, fracture planes in HAZ (Z1 and Z2) compared with base metal thermal cycle distribution across gauge length of DIC test specimen

Figure 4.22 shows the thermal cycle distribution across the gauge length of the DIC extracted specimens. Specimens in Figure 4.22a illustrate the samples extracted from the FZ and HAZ meanwhile the sample in Figure 4.22b shows the samples extracted from the HAZ (without FZ).

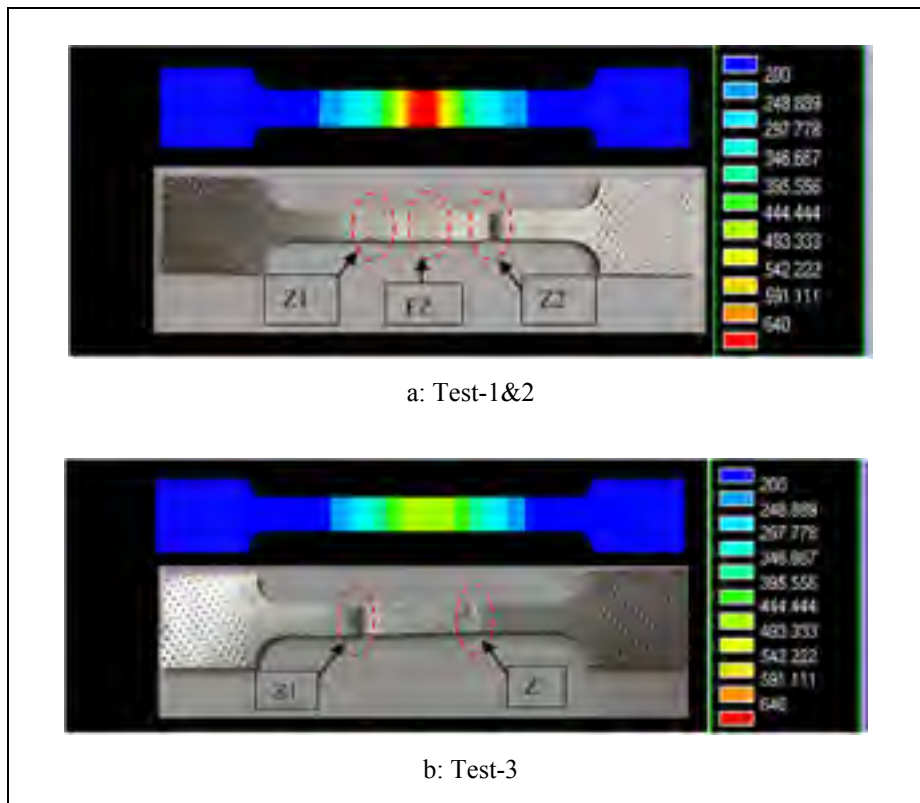


Figure 4.22 Thermal history of extracted samples for DIC test, a) fusion zone, b) HAZ

In the HAZ subzone adjacent to the FZ boundary where the peak temperature was between approximately 400°C - 640°C, the precipitate dissolved resulting in SSS, and because of the high cooling rate in this zone with an average of -26 °C/sec, the formation of re-precipitation during the cooling process was suppressed. In this zone, the increase in tensile properties could be attributed to the natural aging that occurs after cooling. The width of this subzone is about 4.1mm.

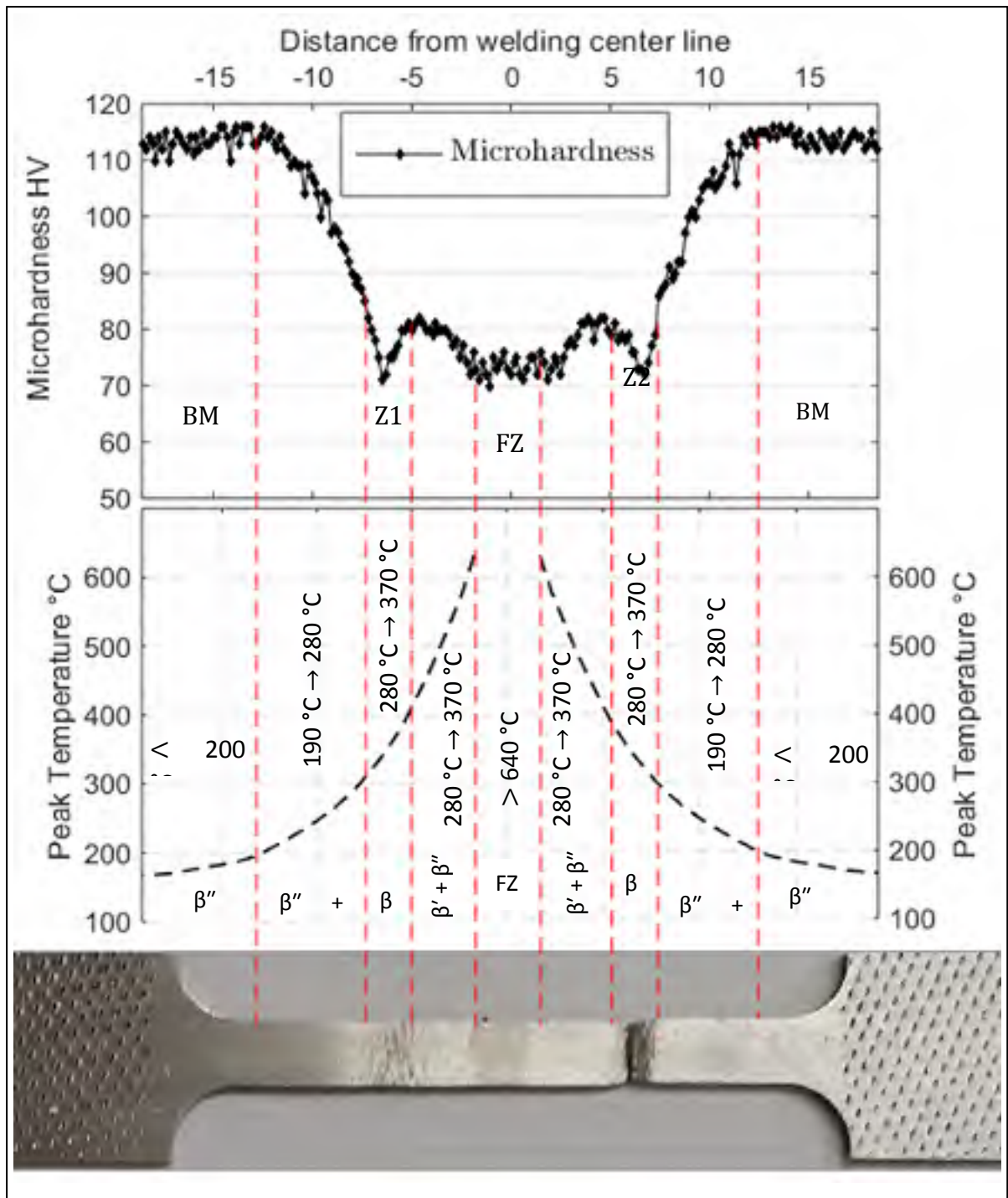


Figure 4.23 Correlations between mechanical properties and peak temperature profile along FZ and HAZ

The subzone located approximately 5.9mm from the welding center line and extended to 8.1 mm was exposed to a peak temperature between 290°C - 380°C. In this over aged zone, the temperature was not sufficient to dissolve the precipitate to SSS, but the temperature and slow cooling rate (6.4 °C/sec) was enough to transform and coarsen the needle shaped precipitate to a semi coherent rod shape β' precipitate and consequently, this zone undergoes a significant over aging effect. The precipitate growth is the main factor causing softening in this zone.

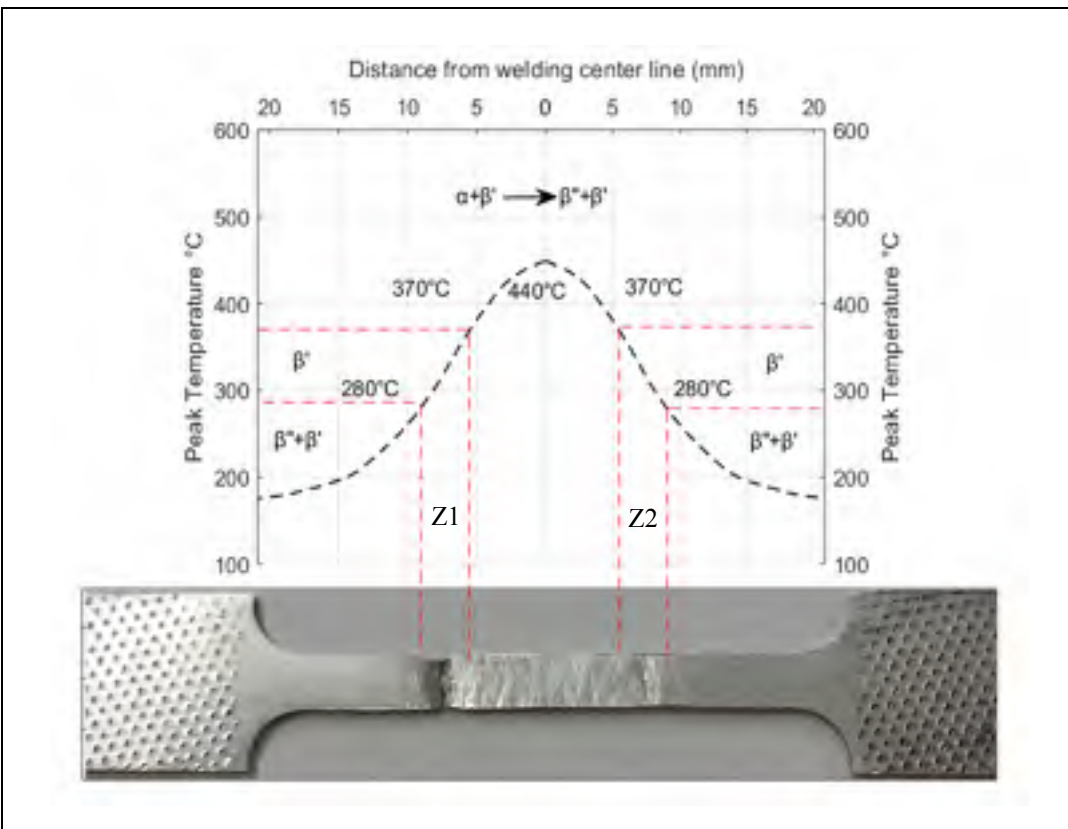


Figure 4.24 Correlations between mechanical properties and peak temperature profile along HAZ

Figure 4.24 shows the peak temperature across gauge length of the sample extracted from the HAZ as showed in Figure 4.22b. In this specimen, even though the zone subjected to a peak

temperature between 370°C - 440°C (which is close to the over aging temperature) suffers high deformation, the over aged planes Z1 and Z2 could be identified and necking and the final fracture occurs in one of these two planes.

CONCLUSION

Welding thermal profile, microstructure characterisation, microhardness, and high-resolution digital image correlation (DIC) during tensile tests were used to document the local mechanical behaviour of the HAZ in aluminum welds obtained by a robotic GMAW process. The following conclusions can be drawn:

1. The thermal analysis using FEA produced reasonably accurate results compared with the experimental thermal profile, and the most significant difference between the experimental results and the model results was an 8.3% difference in the temperature measured by the TCs nearest to the FZ.
2. Mechanical response of the welded sample was significantly influenced by the welding thermal cycle, and the variation in thermal cycle created different subzones in the HAZ. The over aged subzone that produce the lowest hardness could be described as a plane of 2.2 mm width located 5.9 mm to 8.1 mm on both sides of the welding center line. The symmetrical mechanical response on both sides of the weld was a result of the steady welding speed and heat input of robotic welding.
3. The HAZ subzones present different plastic properties from zone to zone and the local mechanical behaviour of these zones varies according to the peak temperature that they were exposed to. The mechanical response of the heterogeneous HAZ leads to the development of extreme localisation of deformed zones within which necking and fracture occurred during tensile testing. These subzones were closely correlated with peak temperature.
4. Though the microhardness technique was able to reveal the lowest hardness regions in the weldment, this technique has limitations for predicting the failure zone as it shows similar hardness values in the FZ and over aged planes.
5. In the high peak temperature zone (above 380°C), the small coherent needle-shaped β'' precipitates dissolved and the biggest one grew to form a semi coherent β' . This

zone regains some of its properties by re-precipitation of β'' during natural aging. Intermediate peak temperature (between 290 °C and 380°C) and the slow cooling rate resulted in coarsening of β'' to a rod shape β' and produced an over aged plane.

RECOMMENDATIONS

While this work focused on the characterisation of mechanical behaviour and microstructure of HAZ subzones, apply the experimental result to develop and validate a predictive approach for welded AA6061-T6.

1. The correlation between hardness and grain growth observed in this investigation by optical microscope is in good agreement with literature data; though, SEM could be used to validate this work.
2. The effect of peak temperature on Mg₂Si precipitate size (growth and coarsening) and the correlation between precipitate transformation and its influence on mechanical properties also requires TEM validation.
3. Correlated transformation of precipitate could be applied to a metallurgical model to calculate the mechanical properties and the softest zone in HAZ subzones based on peak temperature.
4. Phase fraction calculated by SYSWELD could be validated using TEM and used to predict the mechanical properties in HAZ subzones and the global response of the welded joint.

APPENDIX I

WELDED SAMPLES EXPERIMENTAL THERMAL PROFILE CAPTURE WITH THERMOCOUPLES



Figure-A I-1 a) Horizontally welded plate, b) Vertically welded plate.

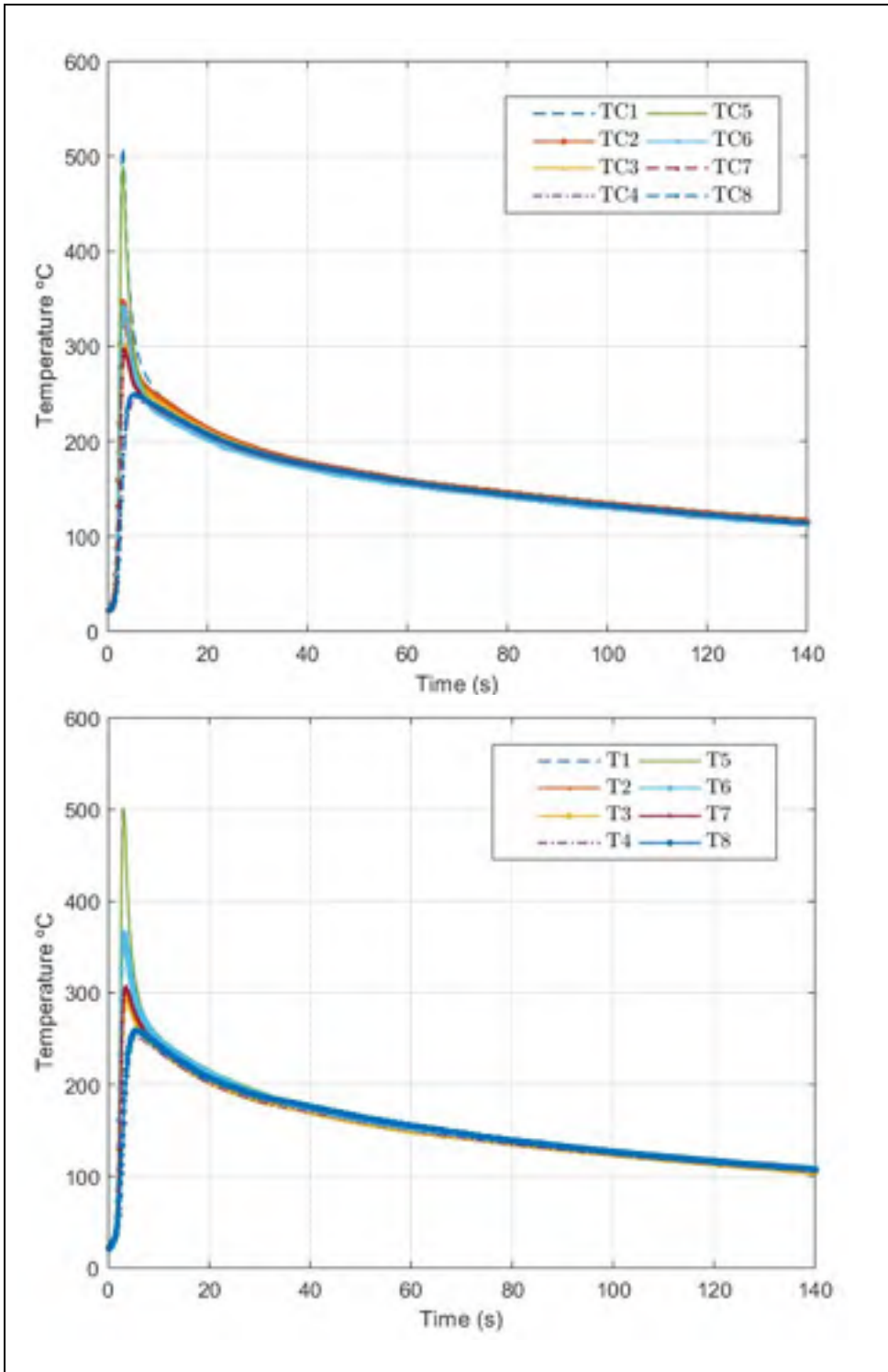


Figure-A I-2 Experimental thermal profile recorded by four TCs in each side of welding line in horizontal plate in Test-2 and Test-3

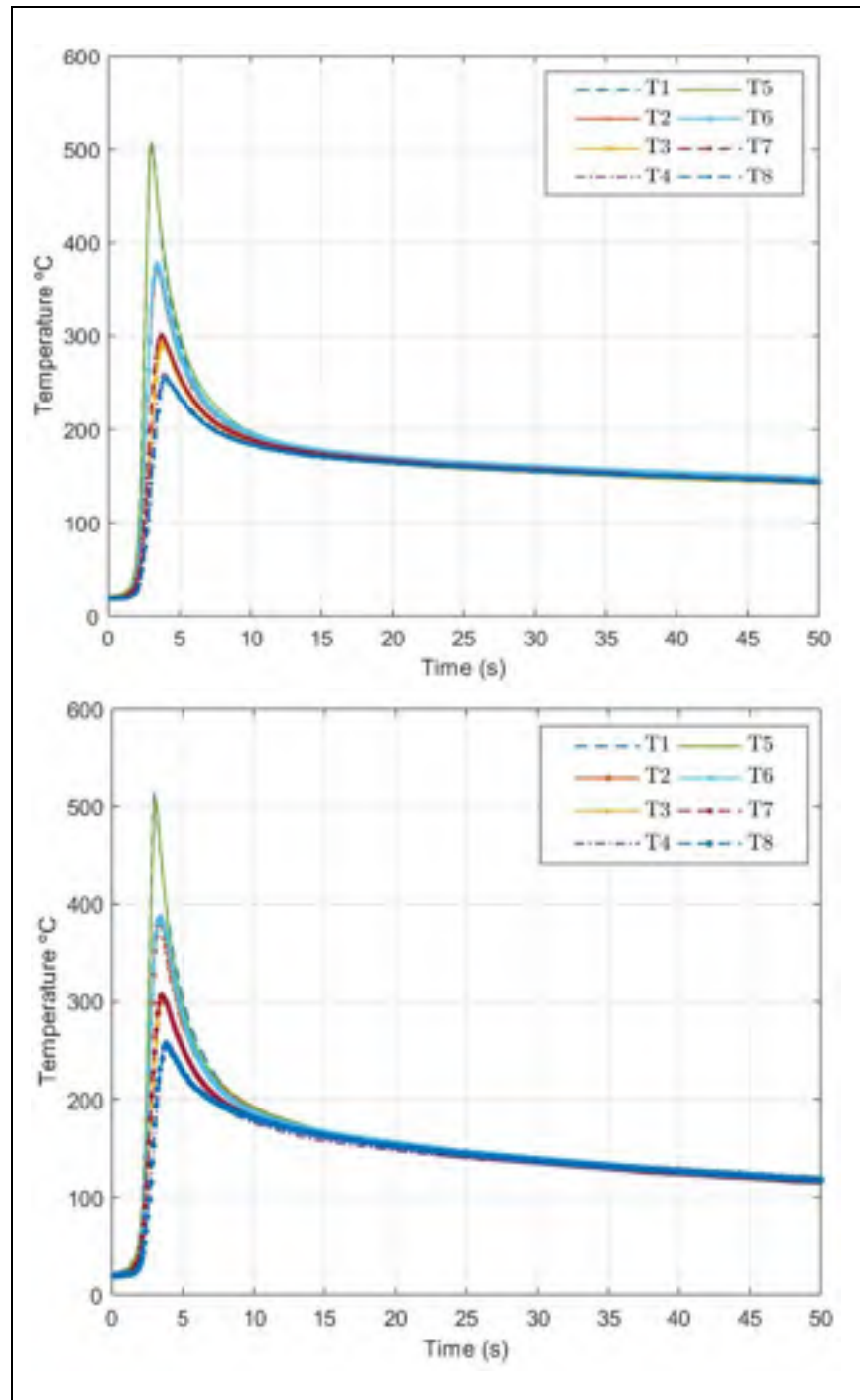


Figure-A I-3 Experimental thermal profile recorded by four TCs in each side of welding line in vertical plate in Test-2 and Test-3

APPENDIX II

THERMAL DISTRIBUTION CALCULATED BY SYSWELD

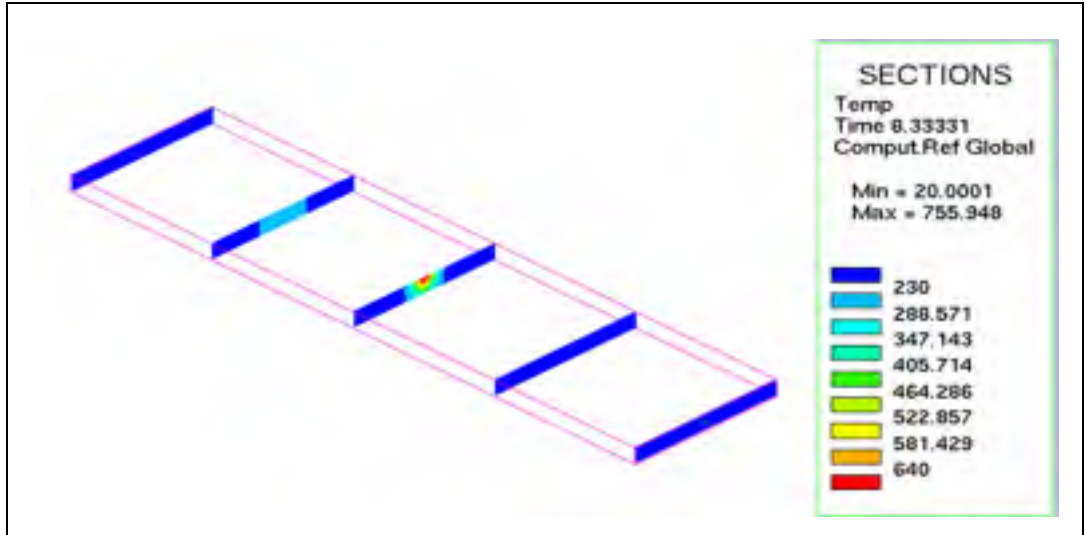


Figure-A II-1 SYSWELD thermal profile at (8.3s)

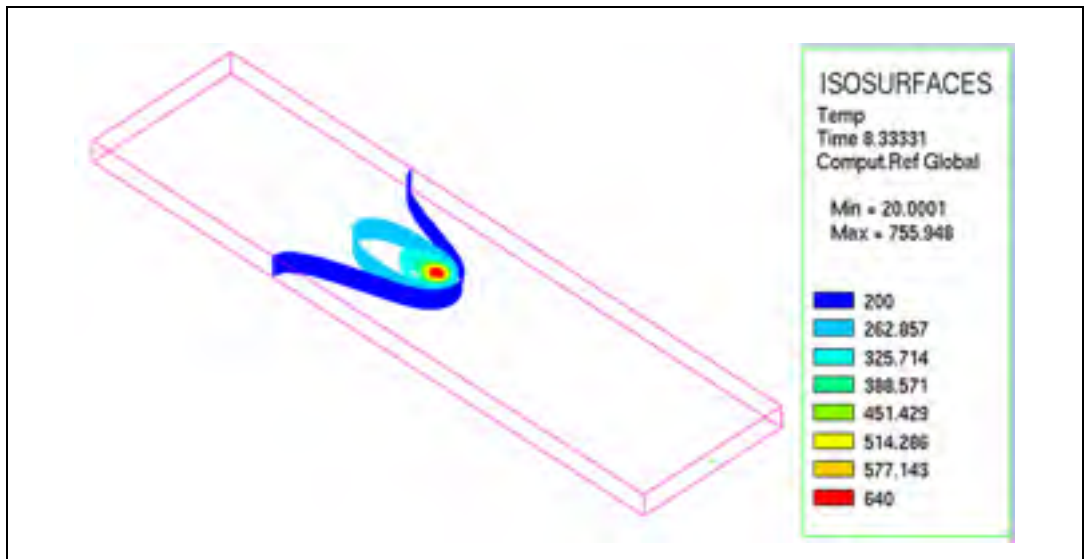


Figure-A II-2 Sysweld thermal profile

APPENDIX III

MICROHARDNESS PROFILE IN TWO CONFIGURATIONS

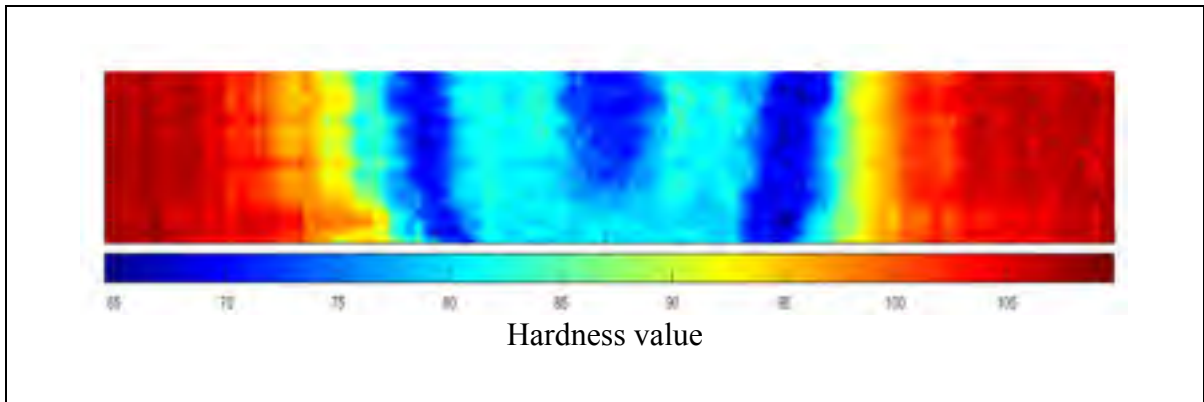


Figure-A III-1 2D Hardness map of cross section of horizontally welded specimen

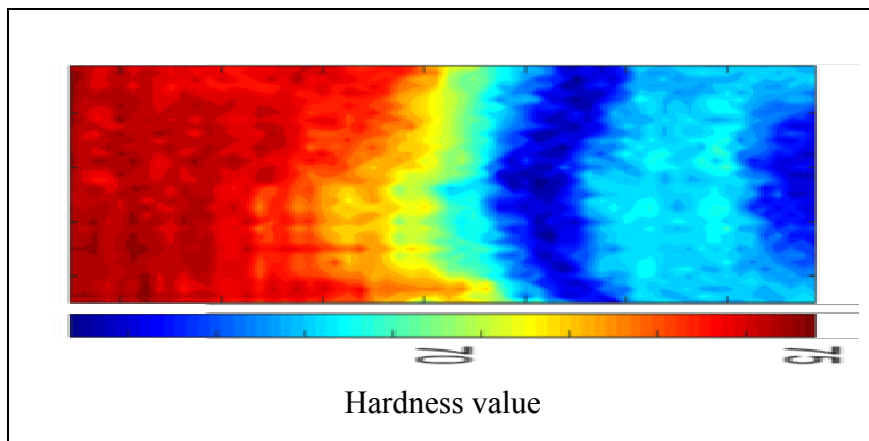


Figure-A III-2 2D Hardness map of cross section of vertically welded specimen

183	184	185	186	187	188	189	190	191	192	193	194	195	196	197	198	199	200	201	202	203	204	205	206	207	208	209	210	211	212	213	214	215	216	217	218	219	220	221	222	223	224	225	226	227	228	229	230	231	232	233	234	235	236	237	238	239	240	241	242	243	244	245	246	247	248	249	250	251	252	253	254	255	256	257	258	259	260	261	262	263	264	265	266	267	268	269	270	271	272	273	274	275	276	277	278	279	280	281	282	283	284	285	286	287	288	289	290	291	292	293	294	295	296	297	298	299	300	301	302	303	304	305	306	307	308	309	310	311	312	313	314	315	316	317	318	319	320	321	322	323	324	325	326	327	328	329	330	331	332	333	334	335	336	337	338	339	340	341	342	343	344	345	346	347	348	349	350	351	352	353	354	355	356	357	358	359	360	361	362	363	364	365	366	367	368	369	370	371	372	373	374	375	376	377	378	379	380	381	382	383	384	385	386	387	388	389	390	391	392	393	394	395	396	397	398	399	400	401	402	403	404	405	406	407	408	409	410	411	412	413	414	415	416	417	418	419	420	421	422	423	424	425	426	427	428	429	430	431	432	433	434	435	436	437	438	439	440	441	442	443	444	445	446	447	448	449	450	451	452	453	454	455	456	457	458	459	460	461	462	463	464	465	466	467	468	469	470	471	472	473	474	475	476	477	478	479	480	481	482	483	484	485	486	487	488	489	490	491	492	493	494	495	496	497	498	499	500	501	502	503	504	505	506	507	508	509	510	511	512	513	514	515	516	517	518	519	520	521	522	523	524	525	526	527	528	529	530	531	532	533	534	535	536	537	538	539	540	541	542	543	544	545	546	547	548	549	550	551	552	553	554	555	556	557	558	559	560	561	562	563	564	565	566	567	568	569	570	571	572	573	574	575	576	577	578	579	580	581	582	583	584	585	586	587	588	589	590	591	592	593	594	595	596	597	598	599	600	601	602	603	604	605	606	607	608	609	610	611	612	613	614	615	616	617	618	619	620	621	622	623	624	625	626	627	628	629	630	631	632	633	634	635	636	637	638	639	640	641	642	643	644	645	646	647	648	649	650	651	652	653	654	655	656	657	658	659	660	661	662	663	664	665	666	667	668	669	670	671	672	673	674	675	676	677	678	679	680	681	682	683	684	685	686	687	688	689	690	691	692	693	694	695	696	697	698	699	700	701	702	703	704	705	706	707	708	709	710	711	712	713	714	715	716	717	718	719	720	721	722	723	724	725	726	727	728	729	730	731	732	733	734	735	736	737	738	739	740	741	742	743	744	745	746	747	748	749	750	751	752	753	754	755	756	757	758	759	760	761	762	763	764	765	766	767	768	769	770	771	772	773	774	775	776	777	778	779	780	781	782	783	784	785	786	787	788	789	790	791	792	793	794	795	796	797	798	799	800	801	802	803	804	805	806	807	808	809	810	811	812	813	814	815	816	817	818	819	820	821	822	823	824	825	826	827	828	829	830	831	832	833	834	835	836	837	838	839	840	841	842	843	844	845	846	847	848	849	850	851	852	853	854	855	856	857	858	859	860	861	862	863	864	865	866	867	868	869	870	871	872	873	874	875	876	877	878	879	880	881	882	883	884	885	886	887	888	889	890	891	892	893	894	895	896	897	898	899	900	901	902	903	904	905	906	907	908	909	910	911	912	913	914	915	916	917	918	919	920	921	922	923	924	925	926	927	928	929	930	931	932	933	934	935	936	937	938	939	940	941	942	943	944	945	946	947	948	949	950	951	952	953	954	955	956	957	958	959	960	961	962	963	964	965	966	967	968	969	970	971	972	973	974	975	976	977	978	979	980	981	982	983	984	985	986	987	988	989	990	991	992	993	994	995	996	997	998	999	1000
-----	-----	-----	-----	-----	-----	-----	-----	-----	-----	-----	-----	-----	-----	-----	-----	-----	-----	-----	-----	-----	-----	-----	-----	-----	-----	-----	-----	-----	-----	-----	-----	-----	-----	-----	-----	-----	-----	-----	-----	-----	-----	-----	-----	-----	-----	-----	-----	-----	-----	-----	-----	-----	-----	-----	-----	-----	-----	-----	-----	-----	-----	-----	-----	-----	-----	-----	-----	-----	-----	-----	-----	-----	-----	-----	-----	-----	-----	-----	-----	-----	-----	-----	-----	-----	-----	-----	-----	-----	-----	-----	-----	-----	-----	-----	-----	-----	-----	-----	-----	-----	-----	-----	-----	-----	-----	-----	-----	-----	-----	-----	-----	-----	-----	-----	-----	-----	-----	-----	-----	-----	-----	-----	-----	-----	-----	-----	-----	-----	-----	-----	-----	-----	-----	-----	-----	-----	-----	-----	-----	-----	-----	-----	-----	-----	-----	-----	-----	-----	-----	-----	-----	-----	-----	-----	-----	-----	-----	-----	-----	-----	-----	-----	-----	-----	-----	-----	-----	-----	-----	-----	-----	-----	-----	-----	-----	-----	-----	-----	-----	-----	-----	-----	-----	-----	-----	-----	-----	-----	-----	-----	-----	-----	-----	-----	-----	-----	-----	-----	-----	-----	-----	-----	-----	-----	-----	-----	-----	-----	-----	-----	-----	-----	-----	-----	-----	-----	-----	-----	-----	-----	-----	-----	-----	-----	-----	-----	-----	-----	-----	-----	-----	-----	-----	-----	-----	-----	-----	-----	-----	-----	-----	-----	-----	-----	-----	-----	-----	-----	-----	-----	-----	-----	-----	-----	-----	-----	-----	-----	-----	-----	-----	-----	-----	-----	-----	-----	-----	-----	-----	-----	-----	-----	-----	-----	-----	-----	-----	-----	-----	-----	-----	-----	-----	-----	-----	-----	-----	-----	-----	-----	-----	-----	-----	-----	-----	-----	-----	-----	-----	-----	-----	-----	-----	-----	-----	-----	-----	-----	-----	-----	-----	-----	-----	-----	-----	-----	-----	-----	-----	-----	-----	-----	-----	-----	-----	-----	-----	-----	-----	-----	-----	-----	-----	-----	-----	-----	-----	-----	-----	-----	-----	-----	-----	-----	-----	-----	-----	-----	-----	-----	-----	-----	-----	-----	-----	-----	-----	-----	-----	-----	-----	-----	-----	-----	-----	-----	-----	-----	-----	-----	-----	-----	-----	-----	-----	-----	-----	-----	-----	-----	-----	-----	-----	-----	-----	-----	-----	-----	-----	-----	-----	-----	-----	-----	-----	-----	-----	-----	-----	-----	-----	-----	-----	-----	-----	-----	-----	-----	-----	-----	-----	-----	-----	-----	-----	-----	-----	-----	-----	-----	-----	-----	-----	-----	-----	-----	-----	-----	-----	-----	-----	-----	-----	-----	-----	-----	-----	-----	-----	-----	-----	-----	-----	-----	-----	-----	-----	-----	-----	-----	-----	-----	-----	-----	-----	-----	-----	-----	-----	-----	-----	-----	-----	-----	-----	-----	-----	-----	-----	-----	-----	-----	-----	-----	-----	-----	-----	-----	-----	-----	-----	-----	-----	-----	-----	-----	-----	-----	-----	-----	-----	-----	-----	-----	-----	-----	-----	-----	-----	-----	-----	-----	-----	-----	-----	-----	-----	-----	-----	-----	-----	-----	-----	-----	-----	-----	-----	-----	-----	-----	-----	-----	-----	-----	-----	-----	-----	-----	-----	-----	-----	-----	-----	-----	-----	-----	-----	-----	-----	-----	-----	-----	-----	-----	-----	-----	-----	-----	-----	-----	-----	-----	-----	-----	-----	-----	-----	-----	-----	-----	-----	-----	-----	-----	-----	-----	-----	-----	-----	-----	-----	-----	-----	-----	-----	-----	-----	-----	-----	-----	-----	-----	-----	-----	-----	-----	-----	-----	-----	-----	-----	-----	-----	-----	-----	-----	-----	-----	-----	-----	-----	-----	-----	-----	-----	-----	-----	-----	-----	-----	-----	-----	-----	-----	-----	-----	-----	-----	-----	-----	-----	-----	-----	-----	-----	-----	-----	-----	-----	-----	-----	-----	-----	-----	-----	-----	-----	-----	-----	-----	-----	-----	-----	-----	-----	-----	-----	-----	-----	-----	-----	-----	-----	-----	-----	-----	-----	-----	-----	-----	-----	-----	-----	-----	-----	-----	-----	-----	-----	-----	-----	-----	-----	-----	-----	-----	-----	-----	-----	-----	-----	-----	-----	-----	-----	-----	-----	-----	-----	-----	-----	-----	-----	-----	-----	-----	-----	-----	-----	-----	-----	-----	-----	-----	-----	-----	-----	-----	-----	-----	-----	-----	-----	-----	-----	-----	-----	-----	-----	-----	-----	-----	-----	-----	-----	-----	-----	-----	-----	-----	-----	-----	-----	-----	-----	-----	-----	-----	-----	-----	-----	-----	-----	-----	-----	-----	-----	-----	-----	-----	-----	-----	-----	-----	-----	-----	-----	-----	-----	-----	-----	-----	-----	-----	-----	-----	-----	-----	-----	-----	-----	-----	-----	-----	-----	-----	-----	-----	-----	-----	-----	-----	-----	-----	-----	-----	-----	-----	-----	-----	-----	-----	-----	-----	-----	-----	-----	-----	-----	-----	-----	-----	-----	-----	-----	-----	-----	-----	-----	-----	-----	-----	-----	-----	-----	-----	------

Figure-A III-3 Microhardness value in weld cross section of vertically welded plate

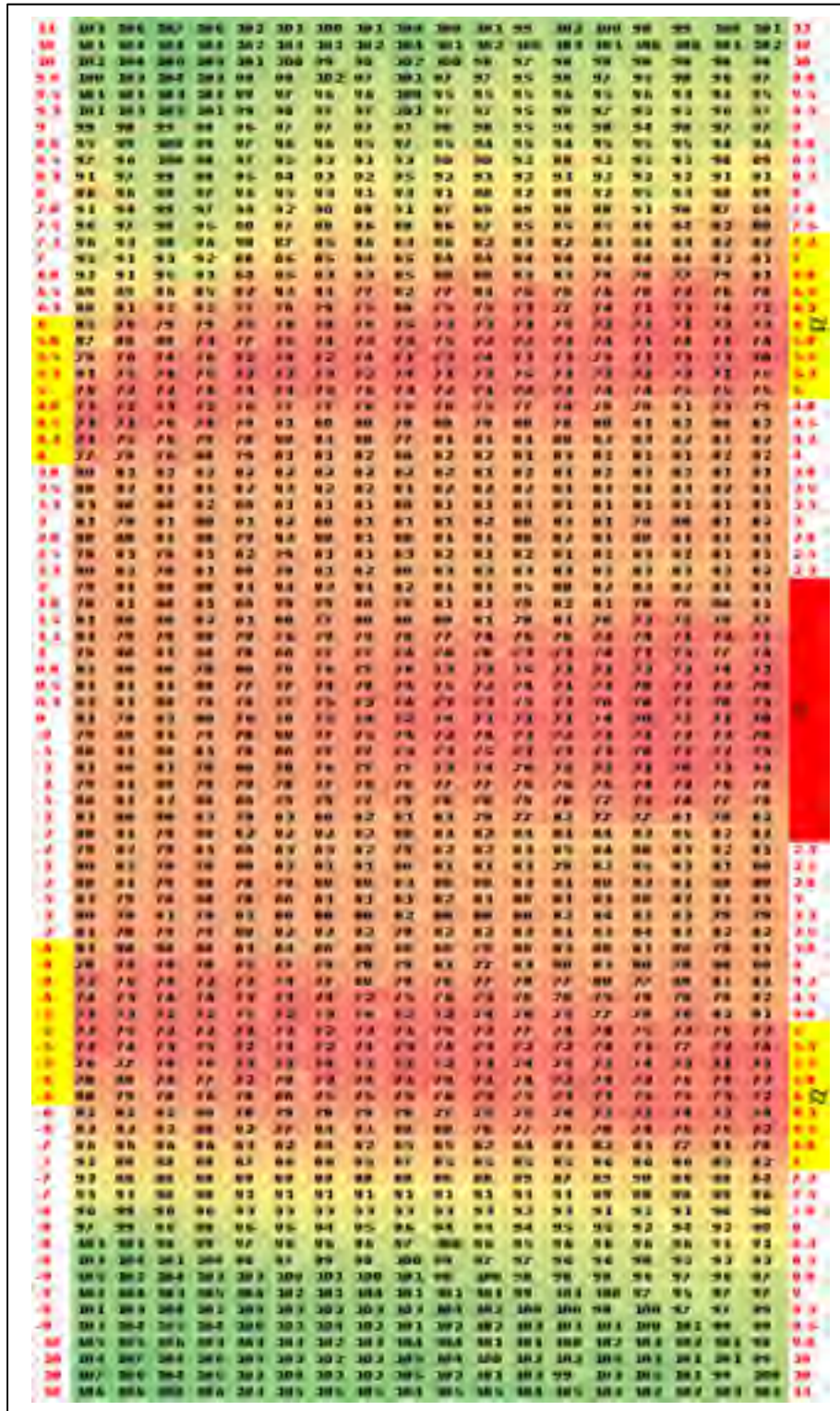


Figure-A III-4 Microhardness value in weld cross section of horizontally welded specimen

APPENDIX IV

MICROFLAT TENSILE TEST (DIC)



Figure-A IV-1 MFT specimens extracted from welded samples



Figure-A IV-2 MFT extracted specimens



Figure-A IV-3 Fracture of MFT specimens DIC test

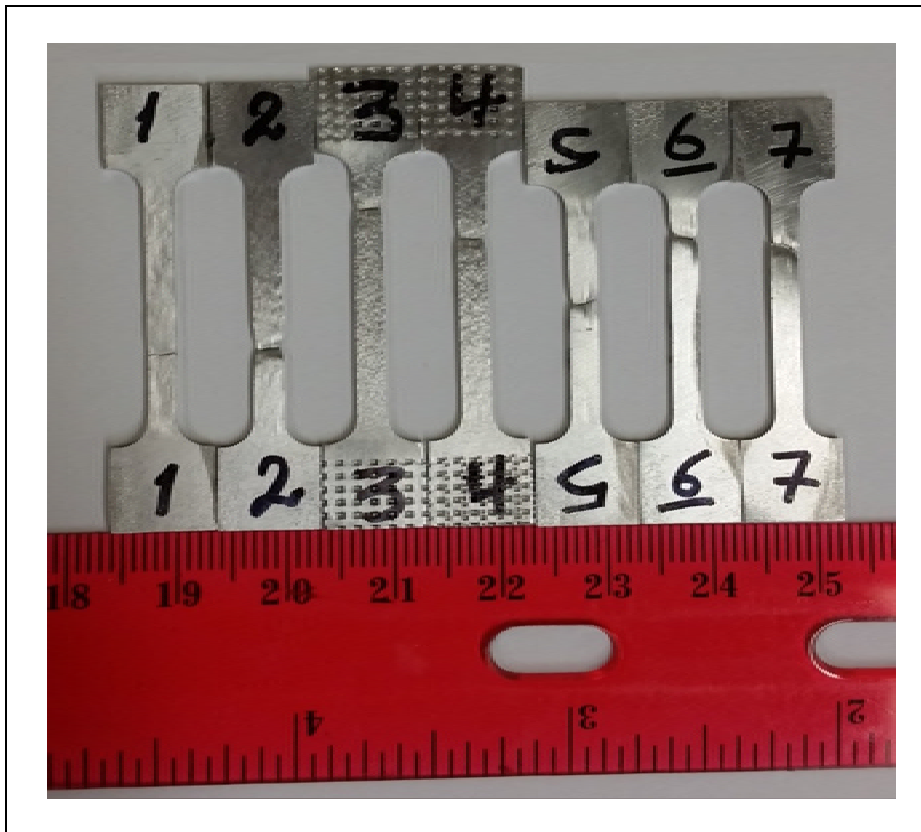


Figure-A IV-4 Fracture of MFT specimens parallel to welding line



Figure-A IV-5 Speckle pattern quality in DIC

LIST OF REFERENCES

- [1] T. Dursun and C. Soutis, "Recent developments in advanced aircraft aluminium alloys," *Materials & Design (1980-2015)*, vol. 56, pp. 862-871, 2014.
- [2] J. S. Pérez, R. R. Ambriz, F. F. C. López, and D. J. Viguera, "Recovery of mechanical properties of a 6061-T6 aluminum weld by heat treatment after welding," *Metallurgical and Materials Transactions A*, vol. 47, no. 7, pp. 3412-3422, 2016.
- [3] D. G. Altenpohl, *Aluminium viewed from within: an introduction into the metallurgy of aluminium fabrication*. Aluminium-Vrlg., 1982.
- [4] J. G. Kaufman and E. L. Rooy, *Aluminum alloy castings: properties, processes, and applications*. ASM International, 2004.
- [5] J. R. Kissell and R. L. Ferry, *Aluminum structures: a guide to their specifications and design*. John Wiley & Sons, 2002.
- [6] L. Zhang, X. Li, Z. Nie, H. Huang, and J. Sun, "Softening behavior of a new Al-Zn-Mg-Cu alloy due to TIG welding," *Journal of Materials Engineering and Performance*, vol. 25, no. 5, pp. 1870-1879, 2016.
- [7] D. Altenpohl and J. G. Kaufman, *Aluminum--technology, Applications, and Environment: A Profile of a Modern Metal: Aluminum from Within--the Sixth Edition*. Aluminium Association, 1998.
- [8] J. R. Davis, *Corrosion of aluminum and aluminum alloys*. ASM International, 1999.
- [9] L. Troeger and E. Starke, "Microstructural and mechanical characterization of a superplastic 6xxx aluminum alloy," *Materials Science and Engineering: A*, vol. 277, no. 1, pp. 102-113, 2000.
- [10] A. Handbook, "Heat treating, vol. 4," *ASM International, Materials Park, OH*, vol. 860, 1991.
- [11] K. Buchanan, K. Colas, J. Ribis, A. Lopez, and J. Garnier, "Analysis of the metastable precipitates in peak-hardness aged Al-Mg-Si (-Cu) alloys with differing Si contents," *Acta Materialia*, vol. 132, pp. 209-221, 2017.
- [12] W. Miao and D. Laughlin, "Effects of Cu content and preaging on precipitation characteristics in aluminum alloy 6022," *Metallurgical and Materials Transactions A*, vol. 31, no. 2, pp. 361-371, 2000.

- [13] D. Pashley, M. Jacobs, and J. Vietz, "The basic processes affecting two-step ageing in an Al-Mg-Si alloy," *Philosophical magazine*, vol. 16, no. 139, pp. 51-76, 1967.
- [14] R. Qiang Gao, K. Stiller, V. Hansen, A. Oskarsson, and F. Danoix, "Influence of aging conditions on the microstructure and tensile strength of aluminium alloy 6063," in *Materials Science Forum*, 2002, vol. 396: Trans Tech Publ, pp. 1211-1216.
- [15] C. F. Tan and S. M. Radzai, "Effect of hardness test on precipitation hardening aluminium alloy 6061-T6," *Chiang Mai Journal of Science*, vol. 36, no. 3, pp. 276-286, 2009.
- [16] C. Gómora, R. Ambriz, F. Curiel, and D. Jaramillo, "Heat distribution in welds of a 6061-T6 aluminum alloy obtained by modified indirect electric arc," *Journal of Materials Processing Technology*, vol. 243, pp. 433-441, 2017.
- [17] O. Myhr, Ø. Grong, H. Fjær, and C. Marioara, "Modelling of the microstructure and strength evolution in Al-Mg-Si alloys during multistage thermal processing," *Acta Materialia*, vol. 52, no. 17, pp. 4997-5008, 2004.
- [18] J. D. Verhoeven, *Fundamentals of physical metallurgy*. John Wiley & Sons Inc, 1975.
- [19] R. W. Hertzberg, *Deformation and fracture mechanics of engineering materials*. Wiley, 1996.
- [20] W. D. Callister and D. G. Rethwisch, *Materials science and engineering*. John Wiley & Sons NY, 2011.
- [21] G. Mathers, *The welding of aluminium and its alloys*. Woodhead publishing, 2002.
- [22] K. Easterling, *Introduction to the physical metallurgy of welding*. Elsevier, 2013.
- [23] S. Kou, *Welding metallurgy*. John Wiley & Sons, 2003.
- [24] N. Nazemi, "Identification of the mechanical properties in the heat-affected zone of aluminum welded structures," 2015.
- [25] G. Liang and S. Yuan, "Study on the temperature measurement of AZ31B magnesium alloy in gas tungsten arc welding," *Materials Letters*, vol. 62, no. 15, pp. 2282-2284, 2008.
- [26] R. R. Ambriz, G. Barrera, R. García, and V. H. López, "Effect of the weld thermal cycles of the modified indirect electric arc on the mechanical properties of the AA6061-T6 alloy," *Welding International*, vol. 24, no. 4, pp. 321-328, 2010.

- [27] V. Malin, "Study of metallurgical phenomena in the HAZ of 6061-T6 aluminum welded joints," *Welding Journal-Including Welding Research Supplement*, vol. 74, no. 9, p. 305s, 1995.
- [28] Y. Liang, J. Shen, S. Hu, H. Wang, and J. Pang, "Effect of TIG current on microstructural and mechanical properties of 6061-T6 aluminium alloy joints by TIG–CMT hybrid welding," *Journal of Materials Processing Technology*, vol. 255, pp. 161-174, 2018.
- [29] K. Zhang, J. Chen, P. Ma, and X. Zhang, "Effect of welding thermal cycle on microstructural evolution of Al–Zn–Mg–Cu alloy," *Materials Science and Engineering: A*, vol. 717, pp. 85-94, 2018.
- [30] D. Narsimhachary, R. N. Bathe, G. Padmanabham, and A. Basu, "Influence of temperature profile during laser welding of aluminum alloy 6061 T6 on microstructure and mechanical properties," *Materials and Manufacturing Processes*, vol. 29, no. 8, pp. 948-953, 2014.
- [31] R. Ambriz, G. Barrera, R. García, and V. López, "A comparative study of the mechanical properties of 6061-T6 GMA welds obtained by the indirect electric arc (IEA) and the modified indirect electric arc (MIEA)," *Materials & Design*, vol. 30, no. 7, pp. 2446-2453, 2009.
- [32] A. Hirose, N. Kurosawa, K. F. Kobayashi, H. Todaka, and H. Yamaoka, "Quantitative evaluation of softened regions in weld heat-affected zones of 6061-T6 aluminum alloy—characterizing of the laser beam welding process," *Metallurgical and Materials Transactions A*, vol. 30, no. 8, pp. 2115-2120, 1999.
- [33] A. M. Handbook, "Properties and Selection: Nonferrous Alloys and Special-purpose Materials, vol. 2, ASM International, Materials Park, OH, 1990," *Google Scholar*.
- [34] O. R. Myhr, Ø. Grong, and K. O. Pedersen, "A combined precipitation, yield strength, and work hardening model for Al-Mg-Si alloys," *Metallurgical and Materials Transactions A*, vol. 41, no. 9, pp. 2276-2289, 2010.
- [35] G. Edwards, K. Stiller, G. Dunlop, and M. Couper, "The precipitation sequence in Al–Mg–Si alloys," *Acta materialia*, vol. 46, no. 11, pp. 3893-3904, 1998.
- [36] J. A. Vargas, J. E. Torres, J. A. Pacheco, and R. J. Hernandez, "Analysis of heat input effect on the mechanical properties of Al-6061-T6 alloy weld joints," *Materials & Design (1980-2015)*, vol. 52, pp. 556-564, 2013.
- [37] O. Myhr and Ø. Grong, "Process modelling applied to 6082-T6 aluminium weldments—I. Reaction kinetics," *Acta Metallurgica et Materialia*, vol. 39, no. 11, pp. 2693-2702, 1991.

- [38] H. Lemmen, R. Alderliesten, R. Benedictus, J. Hofstede, and R. Rodi, "The power of Digital Image Correlation for detailed elastic-plastic strain measurements," *Delft University of Technology*, 2008.
- [39] I. Scheider, W. Brocks, and A. Cornec, "Procedure for the determination of true stress-strain curves from tensile tests with rectangular cross-section specimens," *Journal of engineering materials and technology*, vol. 126, no. 1, pp. 70-76, 2004.
- [40] M. Sutton and P. L. Reu, *International Digital Imaging Correlation Society*. Springer, 2017.
- [41] Z. Liang, B. Yin, J. Mo, and S. Wang, "A new method to deal with the effect of subset size for digital image correlation," *Optik-International Journal for Light and Electron Optics*, vol. 126, no. 24, pp. 4940-4945, 2015.
- [42] L. Scintilla, L. Tricarico, M. Brandizzi, and A. Satriano, "Nd: YAG laser weldability and mechanical properties of AZ31 magnesium alloy butt joints," *Journal of Materials Processing Technology*, vol. 210, no. 15, pp. 2206-2214, 2010.
- [43] C. Leitão, I. Galvão, R. Leal, and D. Rodrigues, "Determination of local constitutive properties of aluminium friction stir welds using digital image correlation," *Materials & Design*, vol. 33, pp. 69-74, 2012.
- [44] W. D. Lockwood, B. Tomaz, and A. P. Reynolds, "Mechanical response of friction stir welded AA2024: experiment and modeling," *Materials Science and Engineering: A*, vol. 323, no. 1, pp. 348-353, 2002.
- [45] A. Reynolds and F. Duvall, "Digital image correlation for determination of weld and base metal constitutive behavior," *Welding Journal*, *New York-*, vol. 78, pp. 355-s, 1999.
- [46] A. Lakshminarayanan, V. Balasubramanian, and K. Elangovan, "Effect of welding processes on tensile properties of AA6061 aluminium alloy joints," *The International Journal of Advanced Manufacturing Technology*, vol. 40, no. 3, pp. 286-296, 2009.
- [47] B. Pan, K. Qian, H. Xie, and A. Asundi, "Two-dimensional digital image correlation for in-plane displacement and strain measurement: a review," *Measurement science and technology*, vol. 20, no. 6, p. 062001, 2009.
- [48] GOM, "ARAMIS user manual–Software," ed: GOM mbH Braunschweig, Germany, 2016.
- [49] ESI Group, "SYSWELD," *Theory Manuals*, *ESI France*, 2012.

- [50] A. Association, *Aluminum: properties and physical metallurgy*. ASM International, 1984.
- [51] A. Handbook, "Volume 15 Casting," *Materials Park: ASM International*, pp. 416-522, 2008.
- [52] L.-Q. Niu, X.-Y. Li, L. Zhang, X.-B. Liang, and M. Li, "Correlation Between Microstructure and Mechanical Properties of 2219-T8 Aluminum Alloy Joints by VPTIG Welding," *Acta Metallurgica Sinica (English Letters)*, vol. 30, no. 5, pp. 438-446, 2017.
- [53] D. Maisonnette, M. Suery, D. Nelias, P. Chaudet, and T. Epicier, "Effects of heat treatments on the microstructure and mechanical properties of a 6061 aluminium alloy," *Materials Science and Engineering: A*, vol. 528, no. 6, pp. 2718-2724, 2011.